

IMPROVING THE ACCURACY AND PRECISION OF  
LASER ABLATION INDUCTIVELY COUPLED PLASMA MASS SPECTROMETRY  
ANALYSIS OF HETEROGENEOUS MATERIALS

By

JANINA R. GUTIERREZ

A DISSERTATION PRESENTED TO THE GRADUATE SCHOOL  
OF THE UNIVERSITY OF FLORIDA IN PARTIAL FULFILLMENT  
OF THE REQUIREMENTS FOR THE DEGREE OF  
DOCTOR OF PHILOSOPHY

UNIVERSITY OF FLORIDA

2003

This document is dedicated to my parents, Girme and Carmencita; and to Rod.

## ACKNOWLEDGMENTS

It has certainly been a privilege to work under the guidance of Dr. James D. Winefordner. I thank him not only for sharing his wisdom and knowledge in science with me, and more for being a kind and understanding adviser. I especially thank Dr. Benjamin Smith for giving me guidance and direction in my research and more for always being ready to listen. I thank Dr. Nicolo Omenetto for his encouragement and support in all my scientific endeavors but more for his contagious positive outlook in life. He never failed to let me see the positive side in everything.

I thank Dr. William W. Harrison for the encouragement and many helpful discussions in group meetings. I also thank Dr. Igor Gorunshkin for the many helpful discussions on research and life. I thank Dr. Paul Mueller for the many in-depth discussions about the field of Laser Ablation ICPMS. I thank my committee members, Dr. Dave Powell and Dr. John Eyler for their support. I also thank Dr. David Hahn for the countless helpful discussions on light scattering, and for the use of the particle measuring systems. I thank the ERC, especially Dr. Kevin Powers and Gil Brubaker, for generously letting me use the Aerosizer. I thank the Pacific Northwest National Laboratory, particularly Dr. Michael Alexander, for funding the research and for loaning me the Argon-ion laser and the waste simulant samples.

I thank the entire Winefordner group for their support. I thank especially Xihong Wu for taking the time to help me with other people's samples so that I could concentrate on my work.

I especially thank Jamshid Temirov for always being ready to help with anything in the laboratory; with lasers, plumbing, lifting, and even with coffee. He, along with Firuza and Diyora, has been, more than anything, my family in Gainesville; and no words can fully express my love and gratitude for them. I deeply express my gratitude to my friends, Isa Benitez, Ivana Boridarivic, and Tamara Blagojevic, who have stood with me from the first day of graduate school to the last. I would not have survived life in graduate school without them. I would also like to thank Rovelyn Tapeç, Celeste Regino, Camilla Yandoc and Gino Ables for welcoming me into Gainesville. They helped make Gainesville a second home for me.

I thank my family for their support and encouragement; especially my parents Girmé and Carmencita. I feel truly blessed to be loved by so many people. Lastly, I would like to thank my fiancé, Rod, who has always stood by me no matter what. I thank him for his love, support, and especially his patience. He has given me something to look forward to everyday.

I consider myself a very blessed person.



## TABLE OF CONTENTS

|   | <u>Page</u> |
|---|-------------|
| ACKNOWLEDGMENTS .....   | iii         |
| ABSTRACT .....  | viii        |
| CHAPTER   |             |
| 1 INTRODUCTION .....  | 1           |
| 2 BACKGROUND .....  | 5           |
| Fundamentals of Lasers .....                                      | 5           |
| Properties of Laser Radiation .....                               | 5           |
| Principles of Laser .....   | 6           |
| Temporal Modes .....  | 9           |
| Nd:YAG Lasers .....   | 10          |
| Principles of Laser Ablation .....                                | 10          |
| Laser Ablation Process .....                                      | 10          |
| Laser-solid Interaction .....                                     | 12          |
| Inductively Coupled Plasma Mass Spectrometry .....                | 13          |
| Inductively Coupled Plasmas .....                                 | 14          |
| The Ionization Process .....                                      | 18          |
| Interfacing ICP and Mass Spectrometer .....                       | 20          |
| Quadrupole Mass Spectrometer .....                                | 25          |
| Mass Detectors .....  | 27          |
| Sample Introduction .....   | 30          |
| Laser Ablation Inductively Coupled Plasma Mass Spectrometry ..... | 30          |
| Analytical Efficiency .....                                       | 34          |
| Ablation Efficiency .....   | 34          |
| Transport Efficiency .....  | 34          |
| Ionization Efficiency .....                                       | 35          |
| Quantitation Strategies .....                                     | 35          |
| Nuclear Waste Samples .....                                       | 36          |
| 3 SOURCES OF NOISE IN THE LA-ICPMS .....                          | 41          |
| Background .....  | 41          |
| Experimental Methods .....  | 42          |
| Results .....   | 44          |
| Conclusion .....  | 50          |

|   |  |     |
|---|--|-----|
| 4 | PARTICLE SIZE DISTRIBUTION STUDIES OF LASER ABLATED MATERIAL                               | 51  |
|   | Background   | 51  |
|   | Experimental Methods   | 53  |
|   | Results  | 55  |
|   | Effect of Laser Wavelength   | 55  |
|   | Effect of Laser Irradiance   | 62  |
|   | Effect of Sample Matrix Properties   | 65  |
|   | Conclusion   | 70  |
| 5 | USING AN INERTIAL IMPACTOR TO IMPROVE PARTICLE SIZE DISTRIBUTION OF LASER-ABLATED MATERIAL | 71  |
|   | Background   | 71  |
|   | Experimental Methods   | 77  |
|   | Results  | 79  |
|   | Effectiveness of the Inertial Impactor as a Particle Filter                                | 79  |
|   | Effect on Signal Intensity and Precision   | 83  |
|   | Effect on Fractionation  | 88  |
|   | Conclusion   | 88  |
| 6 | NORMALIZATION OF LA-ICPMS SIGNAL TO LIGHT SCATTERED BY LASER-ABLATED MATERIAL              | 91  |
|   | Background   | 91  |
|   | Principles of Particle Scatter   | 92  |
|   | Theoretical Considerations to Normalization of ICPMS Signal with Light Scatter             | 94  |
|   | Experimental Methods   | 104 |
|   | Results  | 111 |
|   | Fundamental Studies  | 111 |
|   | Light scatter as a function of particle diameter   | 111 |
|   | Light scatter as a function of particle number density                                     | 118 |
|   | Scatter of Ablated Material  | 121 |
|   | Normalization  | 124 |
|   | Conclusion   | 132 |
| 7 | NORMALIZATION WITH SPECTRAL EMISSION INTENSITY FROM THE LASER INDUCED PLASMA               | 134 |
|   | Background   | 134 |
|   | Experimental Methods   | 135 |
|   | Results  | 136 |
|   | Conclusion   | 147 |
| 8 | LA-ICPMS ANALYSIS OF WASTE SIMULANTS   | 148 |
|   | Experimental Methods   | 148 |
|   | Results  | 149 |
|   | Dry vs. Wet Ablation   | 149 |

|  |     |
|--|-----|
| LA-ICPMS Analysis of Waste Simulant.....     | 153 |
| Studies Performed with the PNNL System ..... | 164 |
| Effect of varying laser irradiance .....     | 164 |
| Raster vs. no raster .....                   | 171 |
| Impactor studies .....                       | 171 |
| Scanning electron images.....                | 175 |
| Conclusion .....                             | 181 |
| 9 CONCLUSION AND FUTURE WORK .....           | 182 |
| Conclusion .....                             | 182 |
| Future Work.....                             | 184 |
| LIST OF REFERENCES .....                     | 186 |
| BIOGRAPHICAL SKETCH .....                    | 189 |

Abstract of Dissertation Presented to the Graduate School of the University of Florida in  
Partial Fulfillment of the Requirements for the Degree of  
Doctor of Philosophy

IMPROVING THE ACCURACY AND PRECISION OF LASER ABLATION  
INDUCTIVELY COUPLED PLASMA MASS SPECTROMETRY ANALYSIS OF  
HETEROGENEOUS SAMPLES

By

Janina R. Gutierrez

August 2003

Chair: James D. Winefordner  
Major Department: Chemistry

Laser ablation inductively coupled plasma mass spectrometry (LA-ICPMS) has developed into an important and indispensable tool for solid sampling analysis. The use of LA-ICPMS allows rapid *in situ* analysis requiring minimal sample preparation while using a minimal amount (micrograms) of sample. Low detection limits of parts per billion are also easily achieved for most elements using the LA-ICPMS. However, the use of LA-ICPMS has yet to be fully developed as a rapid and routine method of analysis for heterogeneous materials. Matrix-matched standards are required for quantitative analyses. Variations in the laser ablation process, and elemental and isotopic fractionations may occur during analysis affecting both precision and accuracy.

The goal of this research is to improve the precision and accuracy of LA-ICPMS analysis of heterogeneous materials.

Initial stages of the study involved fundamental studies to determine the causes of poor precision and accuracy in LA-ICPMS. Results showed that the limiting source of noise in LA-ICPMS is flicker or excess low frequency noise originating from variations in the sample aerosol as they are created, transported and introduced into the ICP. Particle size distribution studies of laser-ablated material were then performed to determine the ablation parameters that produced sample aerosol with the optimum particle size distribution yielding the best ICP signal in terms of signal intensity and stability.

An inertial impactor was used to improve the particle size distribution of the ablated material prior to its introduction into the ICPMS. Results showed that removing the larger particles from ablated material improved ICPMS signal precision. ICP-induced elemental and isotopic fractionation effects were also reduced by removing larger particles from the ablated material. Light scattered by ablated material was also collected and used for normalization of the ICPMS signal. Results show that normalization to light scattered by the ablated material compensated for variations in the mass ablated, or the number of particles ablated during an analysis. The use of the spectral emission intensity of an analyte collected from the laser-induced plasma to normalize its corresponding LA-ICPMS signal was also investigated.

Finally, the proposed approaches to improving the precision and accuracy of LA-ICPMS were applied to heterogeneous nuclear waste simulants.

## CHAPTER 1 INTRODUCTION

Laser Ablation Inductively Coupled Plasma Mass Spectrometry (LA-ICPMS) has developed into an important analytical tool in a variety of applications involving a wide range of solid materials such as glasses, ceramics, soils, and plastics<sup>1</sup>. The use of LA-ICPMS allows solid sampling of diverse materials ranging from conducting to non-conducting, and from organic to inorganic materials. Solids in the form of sheets, powders, pastes and even sludges can easily be sampled. The use of LA-ICPMS allows rapid *in situ* analysis requiring minimal sample preparation while using a minimal amount (micrograms) of sample. Low detection limits of parts per billion are also easily achieved for most elements using the LA-ICPMS. However, the use of LA-ICPMS has yet to be fully developed as a rapid and routine method of analysis. Matrix-matched standards are required for quantitative analyses. Variations in the laser ablation process and elemental and isotopic fractionations may occur during analysis affecting both precision and accuracy. The use of LA-ICPMS lacks both precision and accuracy. Current %RSDs range from 5 to 20% depending on the sample being analyzed.<sup>1-3</sup>

These problems are escalated in the analysis of heterogeneous samples. Heterogeneity is defined in this research as the existence of non-uniformity of a physical or chemical property in the sample. The heterogeneous samples we refer to possess non-uniformity in sample surface morphology and consistency; and non-uniformity in sample composition, specifically nuclear wastes. Nuclear wastes considered in this study are in the form of sludge, and paste, seemingly highly viscous liquids with solid granules

embedded in the sample. When prepared for ablation, the sample surface is highly non-uniform with tiny grains randomly embedded around the surface of the sample. The possibility of heterogeneity in elemental composition between a granule and the paste also exists.

Several challenges exist in the analysis of heterogeneous materials by LA-ICPMS. These challenges, while relying on laser-solid interaction, can be either independent of or inherent to the use of LA-ICPMS as the method of analysis. There are two main causes of poor precision and accuracy in LA-ICPMS: variation in mass ablated; and the existence of a particle size distribution in the sample introduced to the plasma.

The variation in the mass ablated during analysis is a combined effect of two factors: laser pulse to pulse fluctuation and heterogeneity in sample morphology. Pulse to pulse laser energy fluctuation results in non-linear variations in sample mass removal; and ultimately in the ICPMS signal. Variation in mass removal is magnified when ablating heterogeneous materials, particularly materials with a non-uniform surface and with a heterogeneous surface. For example, ablation of a small granule that is part of the paste-like nuclear waste will yield a different mass upon ablation compared to the rest of the sample. Furthermore, there is also a possibility that the granule will have a different elemental composition than the rest of the sample. This will be the case even if the laser pulse-to-pulse variation were solved.

The particle size distribution of the sample introduced into the plasma affects both precision and accuracy. The particle size distribution of the ablated material affects the transport and ionization efficiency. Large particles ( $>3\text{ }\mu\text{m}$  in diameter) arrive randomly at the ICP, resulting in signal fluctuations<sup>4</sup>. Furthermore, large particles also may not be

vaporized and ionized efficiently in the plasma resulting in elemental fractionation. Particles ionized inefficiently in the ICP have also been shown to act as a heat sink and cause temperature differences in the plasma<sup>4</sup>. The variation in particle size distribution of laser-ablated material is affected by laser ablation parameters (such as laser fluence, wavelength, repetition rate, beam diameter, focus, pulse length, and sample matrix properties). Variations in the distribution are also heightened by samples with heterogeneous morphology. The laser-solid interaction varies with the properties of the area irradiated with the laser, resulting in variations in sample aerosol size distributions.

The goal of this study was to improve the accuracy and precision of LA-ICPMS in the analysis of heterogeneous materials. This research was divided into five major parts. A thorough investigation of the causes of poor precision and accuracy in LA-ICPMS was performed. The sources of noise in LA-ICPMS were identified and discussed. An investigation of the factors affecting particle size distribution and their optimization were also performed. This was done to find the ablation parameters that resulted in the optimum laser-ablated material for best ICP analytical results. A methodology to modify the size distribution of the laser-ablated material was developed. This required the use of an inertial impactor to physically filter out larger particles in the sample aerosol. Normalization techniques to account for variations the size distributions and the mass of the laser-ablated material were also developed. The first normalization technique involved collecting the light scattered by ablated material; and using this signal to normalize the ICP mass spectrometer signal. The second normalization technique involved collecting and monitoring the analyte emission intensity from the laser-induced plasma. Finally, information learned from the investigation, and the techniques of



modifying the particle size distribution and normalization were applied to the analysis of nuclear waste simulants.

## CHAPTER 2 BACKGROUND

### **Fundamentals of Lasers**

Since the advent of lasers in the 1960's, and the first report of the ruby laser by T.H. Maiman,<sup>5-6</sup> lasers have been widely used in a number of analytical applications in atomic spectroscopy.<sup>7</sup> Lasers have been used in methods involving absorption, emission, fluorescence, ionization and photothermal processes. Since 1962, the plasma produced by the high fluence of a focused beam has been used to help determine the concentrations of chemical elements in selected micrometer diameter regions of many samples.<sup>8-9</sup> In this section however, the focus will be on the use of a laser as a microprobe. The properties and characteristics of a laser as a source of radiation make it ideal method as a direct ablation source for analysis of solids.

### **Properties of Laser Radiation**

A laser beam is of directionality, high radiance, monochromaticity, and coherence. Laser radiation is nearly monochromatic. Light emitted by a laser has a very small range of wavelength so that all photons have almost the same energy. This property makes it possible to use a laser with very high selectivity, exciting only atomic or molecular species of interest.

Laser radiation is of high irradiance. Irradiance can be defined in this case as the radiant power (W) per unit surface area ( $\text{cm}^2$ ) that is emitted from an infinitesimal area of a surface.<sup>9</sup>

Laser radiation is highly directional. A laser beam can be confined to a narrow cone of angles. This property makes it possible to transport the laser beam to a region of interest with insignificant loss of intensity.

Laser radiation is spatially and temporally coherent. Spatial coherence means that there is a constant time-independent phase difference for the amplitude at two different points of the wave. Temporal coherence means that for a given point in space, there is always a constant phase difference between the amplitude of the wave at two successive instances in time.

As a result of laser radiation possessing these characteristics, radiation emitted by a laser can be easily focused into a small area resulting into an extremely high irradiance of electromagnetic energy (up to  $10^{12}$  W/cm<sup>2</sup>). Such high irradiance results in intense heating of the irradiated matter so that the laser interaction produces a change of state from solid to plasma within a very short time. Consequentially, particles such as excitons, photons, phonons, excited molecules, neutral and excited atoms, and ions are produced.

### **Principles of Laser**

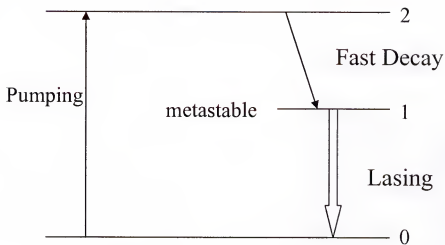
The term “laser” is an acronym for “light amplification by stimulated emission of radiation”. The principle behind lasers is stimulated emission of radiation achievable by population inversion. An excited atom is struck by a photon of exactly the same energy as the one that would be emitted. The excited atom is stimulated to emit a photon, so that two photons of the same wavelength result.

A laser consists of three main components, an active or lasing medium, an energy pump or source and an optical resonator. The active medium amplifies an incident electromagnetic wave. The energy pump selectively brings energy into the active medium

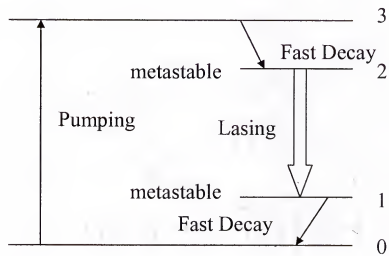
to populate selected levels and to achieve population inversion. The optical resonator, composed of a highly reflecting and a partially reflecting mirror placed opposite each other, partially stores the induced emission; and causes selective feedback of the radiation emitted from the excited species in the active medium.

A primary requirement of light amplification or stimulated emission is an inversion of the population densities of the energy levels. Atoms must be raised from the ground state into a higher energy state by some means. During the excitation, the number of the atoms in the ground state will eventually decrease; and correspondingly, the number of atoms in the excited state will increase. Population inversion will occur only if one or more intermediate or metastable levels between the ground and excited state. Figure 2-1 illustrates the lasing scheme for three- and four-level systems. In this case, the excited atoms decay to the metastable level, and then decay further to the ground level. In a three-level scheme for example, population inversion can occur if the intermediate level (labeled level 2 in Figure 2-1A) is long-lived compared to the upper level (level 3) so that the population in the intermediate level can grow relative to the ground state until the inversion is achieved. In the four-level lasing scheme, the atoms are excited to level 3. Excited atoms decay rapidly to level 2. Because level 2 is long-lived compared to level 3, a population inversion occurs between level 2 and the ground state. Thus, lasing occurs from level 2 to level 1.

Once population inversion is achieved, oscillation can be achieved by the process of spontaneous emission. If the net gain of laser amplification between the mirrors exceeds losses by reflection, the generated laser beam exits through the partially reflecting mirror. When coherent oscillation occurs, the output laser beam is highly



A



B

Figure 2-1. Lasing schemes: A) Three-level scheme. B) Four-level scheme.

directional and monochromatic.

### **Temporal Modes**

Lasers can be operated in four major temporal modes. These are continuous-wave, pulsed (or normal),  $Q$ -switched, and mode-locked.<sup>10</sup> In a continuous-wave laser, the output beam is continuous with time. Correspondingly, the upper level of the lasing transition must have a longer lifetime than the lower level. In pulsed lasers, the output radiation is a train of repetitive pulses. The radiant power output can be very high (reaching up to MW) during the pulse even if the average power is low. In this case, the upper level has a shorter lifetime than the lower level. In a mode-locked laser, the pulses are ultra-short, lasting for picoseconds. The pulses have a high peak power. This is accomplished by forcing the phases of the oscillating modes to be correlated or locked to each other.

Lasers used for ablation are usually run in the  $Q$ -switched mode to obtain powerful giant pulses. In a laser run at normal mode, the  $Q$ -factor, defined as the ratio of the energy stored to the energy loss, is kept constant. In the  $Q$ -switched mode, the quality factor  $Q$  of the cavity is lowered and the oscillation is prevented until population inversion is well beyond the threshold value. By using an optical element in the laser cavity, oscillation is prevented, and energy will accumulate gradually in the laser medium. If the  $Q$ -factor is suddenly increased by removing the element, a large population inversion occurs in the cavity; and a high-powered pulse is produced (lasting for a few nanoseconds). Since a significant amount of energy is released in a relatively short time, the peak power of a  $Q$ -switched laser is very high.

### **Nd:YAG Lasers**

A laser commonly used for ablation is the Nd:YAG ( $\text{Nd}^{3+}:\text{Y}_3\text{Al}_5\text{O}_{12}$ ) or Neodymium Yttrium-Aluminum Garnet. The lasing medium is a neodymium crystal coated with yttrium-aluminum garnet. A Xe-arc flashlamp is normally used to pump the Nd:YAG laser. The generated frequency from this laser is 1064 nm, but frequency doubling mechanisms can be used to convert the radiation to 532 nm. Radiation at 355 nm can also be generated by frequency mixing 1064 nm and 532 nm. In addition, 266 nm can be generated by frequency doubling the 532 nm light.

### **Principles of Laser Ablation**

The primary goal of laser ablation for ICPMS analysis is to transform an amount of sample into the vapor phase with stoichiometric composition representative of the sample. Understanding the fundamentals of the ablation process and laser-solid interaction is important in successfully producing stoichiometric sample aerosols for precise and accurate ICPMS analysis.

### **Laser Ablation Process**

Laser ablation is governed by a variety of distinct non-linear mechanisms. These mechanisms can be summarized as three fundamental processes occurring over several orders in time.<sup>1</sup> These mechanisms are laser-solid interactions at the target, plasma initiation off the target, and laser interactions with the expanding plasma. As a high-power laser pulse is focused on a sample, the irradiance on the ablated area leads to rapid local heating, intense vaporization, and degradation of the material. The ablated material compresses the surrounding gas and leads to the formation of a shockwave. The beam also interacts with the partially ionized vaporized material and affects the quality of ablation.

A better understanding of the ablation process can be attained by looking at the ablation using different laser irradiances. R.E. Russo<sup>11,12</sup> described in detail the physics of laser ablation in microchemical analysis using five different laser irradiances with four transition points or thresholds. The transitions characterize changes in the dominant ablation mechanism for different ranges of laser intensities.

At laser intensities below the ablation threshold, with irradiance less than  $10^7$  W/cm<sup>2</sup>, atoms or ions may be released or desorbed from the surface, but there is no bulk mass removal suitable for microchemical analysis. Increasing the laser irradiance removes a significant fraction of the laser-irradiated region. The ablation is governed by laser-induced melting and vaporization, along with energy dissipation into the bulk of the sample through heat conduction. For laser wavelengths in the UV to near-IR range, the ablation process starts with the absorption of photon energy by free electrons in the sample. The excited electrons then collide with lattice phonons and transfer energy to the lattice through delocalized relaxation mechanisms. Irreversible surface damage will occur at the laser-irradiated spot if the temperature of the lattice exceeds the melting point of the sample. If additional laser irradiance is incident on the sample, it will result in vaporization. A plume of vapor will form and expand away from the sample surface as a result of the pressure difference between the rapidly vaporized sample material and the atmosphere.

With laser irradiances greater than  $10^7$  W/cm<sup>2</sup> but less than  $10^8$  W/cm<sup>2</sup>, the plume of ablated material released can be partially ionized. At these irradiances, the ionized mass plume can shield the sample from the trailing part of the laser beam pulse. The electrons emitted at the early stage of ablation can gain energy from the trailing part of



the laser pulse through collisions with the ionized mass vapor. When the kinetic energy of the electrons is higher than the ionization potential of the evaporated atoms from the sample, the atomic vapor is ionized. When ionized, the vapor absorbs the laser energy and shields the sample surface from further exposure to the laser beam, which reduces the efficiency of sample removal.

Ablation with irradiances of about  $10^9 \text{ W/cm}^2$  is characterized by an explosive ablation. At such high irradiances, the irradiated sample is heated above its normal boiling point. The sample then becomes metastable. As the sample approaches its thermodynamic critical state, density fluctuations may create vapor bubbles inside the superheated liquid sample volume. The rate of homogenous nucleation then rises near the critical temperature. Bubbles will grow if their radii are greater than critical values. The sample will then undergo a rapid transition into a mixture of vapor and liquid droplets. Molten droplets will then be ejected from the sample surface as a result of the rapid expansion of the high pressure bubbles.

For irradiances greater than  $10^9 \text{ W/cm}^2$ , the ablation is explosive and the efficiency of sample removal is reduced. At the early stage of laser irradiation, the emitted electrons from the sample surface collide with air molecules and absorb laser energy by inverse Bremsstrahlung processes. These electrons then ionize the air which expands rapidly during the laser pulse forming a plasma. At these high irradiances, the ablation efficiency will be reduced by plasma absorption, in particular for picosecond and short nanosecond laser ablation.

### **Laser-solid Interaction**

As the laser beam strikes the sample, photons are absorbed by the sample producing photoelectrons and ions. Heat is conducted through the sample resulting in

rapid melting and boiling over the area ablated. Vaporization and ejection of molten sample follows. The time required for the sample to increase its vaporization temperature ( $t_v$ ) is defined by Equation 21.

$$t_v = \frac{\pi k \rho c (T_v - T_o)^2}{4 P^2} \quad (2-1)$$

where  $k$  is the thermal conductivity (W/cmK),  $\rho$  is the sample mass density (g/cm<sup>3</sup>),  $P$  is the laser power density absorbed by the sample (W/cm<sup>2</sup>),  $c$  is the heat capacity (J/gK),  $T_o$  is the initial temperature (K), and  $T_v$  is the vaporization temperature (K). The factors  $k$ ,  $c$  and  $T_v$  depend on the composition of the sample. Therefore the time required for the sample to be raised to its vaporization temperature is dependent on sample composition.

The interaction between the laser beam and a solid depends on laser parameters, such as pulse width, spatial, temporal, and power fluctuation of pulse, and on the mechanical, physical and chemical properties of the sample.

### **Inductively Coupled Plasma Mass Spectrometry**

First introduced in 1961, the inductively coupled plasma (ICP) has developed into one of the most widely used and significant tool in analytical atomic spectroscopy. The ICP was initially studied as an analytical emission source in the early 1960s by Fassel and coworkers (Iowa State University)<sup>13</sup> and by Greenfield and coworkers in England (Albright and Wilson Ltd.)<sup>14</sup>. It was not until 1980 that S. Houk and coworkers<sup>15</sup> first introduced coupling the ICP with a quadrupole mass spectrometer for the analysis of aqueous solutions. Since then, ICP-MS has developed rapidly as a routine means for elemental analysis of a wide range of samples. As an analytical technique, ICP-MS possesses three unique capabilities for elemental analysis. First, ICPMS offers very low detection limits. Current detection limits for the direct analysis of solution samples are in

the range of low pg/mL for most elements<sup>2</sup>. Table 2-1 summarizes current detection limits attained by ICPMS. Second, the mass spectra of elements are relatively simple. Because the natural isotope abundance spectral pattern provides quick and essentially formidable evidence for the qualitative identification of an element, ICPMS can be applied to automated qualitative and semi-quantitative elemental analysis. Third, ICPMS allows measurement of elemental and isotopic ratios. ICPMS can be readily used for routine isotopic ratio data and isotope dilution. Complications of the ICPMS as a technique include spectra interferences arising mainly from molecular species and from matrix effects.

### **Inductively Coupled Plasmas**

The inductively coupled plasma is defined as an electrodeless discharge in a gas (commonly argon) at atmospheric pressure, maintained by energy coupled to it from a radio frequency generator. The three components used to generate the ICP are the plasma torch, the radio frequency (RF) coil, and the RF power supply.

Figure 2-2 illustrates the schematic of a typical ICP torch used for ICPMS. The ICP is created in a stream of argon gas flowing through an assembly of three concentric quartz tubes known as the plasma torch. The torch commonly used is based on the design of Scott and Fassel (1974)<sup>16</sup>. The torch has an outer tube with an inner diameter of 18 mm and is about 100 mm long. Inside the outer tube are two concentric tubes of 13 and 1.5 mm inner diameter ending short of the torch mouth. Each annular region formed by the tubes is supplied with gas by a tangential side tube resulting in a vorticular

Table 2-1. Detection limits of Perkin Elmer Sciex ICPMS system.

| 0.0001--0.001 ppb |    | 0.001-0.1 ppb |    | 0.01-0.1 ppb | 0.1-1 ppb | 1-10 ppb | >10 ppb |
|-------------------|----|---------------|----|--------------|-----------|----------|---------|
| Bi                | Sr | Ag            | Nd | B            | Br        | Ca       | C       |
| Ce                | Ta | Al            | Ni | Be           | Fe        | Cl       | S       |
| Co                | Tb | As            | Pb | Cr           | K         |          |         |
| Cs                | Th | Au            | Pd | Li           | P         |          |         |
| Er                | Tl | Ba            | Pt | Na           | Si        |          |         |
| Eu                | Tm | Cd            | Rb | Se           |           |          |         |
| Hf                | U  | Cu            | Ru | Se           |           |          |         |
| Ho                | Y  | Dy            | Sb | Te           |           |          |         |
| In                | Ir | Ga            | Sm |              |           |          |         |
| La                | Lu | Gd            | Sn |              |           |          |         |
| Nb                | Pr | Ge            | Ti |              |           |          |         |
| Re                | Rh | Hg            | V  |              |           |          |         |
|                   |    | I             | W  |              |           |          |         |
|                   |    | Mg            | Yb |              |           |          |         |
|                   |    | Mn            | Zn |              |           |          |         |
|                   |    | Mo            | Zr |              |           |          |         |

Source: Perkin Elmer Sciex brochure, Montaser and Golightly 1992

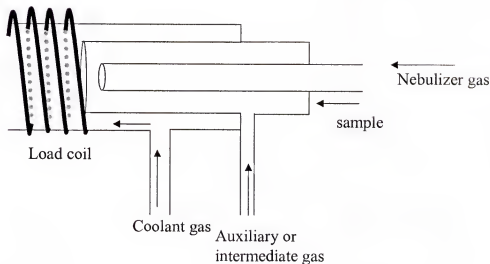


Figure 2-2. A schematic diagram of an ICP torch (Fassel type).

flow. The sample is brought into the plasma from the nebulizer through the center tube with gas flowing at typical values of 1 l/min. The nebulizer gas flow physically punches a channel through the center of the plasma. The outer gas flow (10 to 15 l/min) is called the coolant gas flow which protects the walls of the torch and supports the plasma. The gas flow introduced to the inner annular space is called the auxiliary gas flow with typical flow rates of 0.1-1.5 l/min. The auxiliary gas flow pushes the plasma away from the central tube to prevent melting.

The RF coil is made of 2 to 4 turns of copper tubing cooled by a water or gas flow. The torch is mounted horizontally and positioned centrally in the RF coil. The RF coil is a few mm away from the mouth of the torch.

The RF power supply, with frequency of 27 or 40 MHz, generates a magnetic field, so that the field lies along the axis of the torch.

Figure 2-3 illustrates the formation of the ICP. The plasma discharge forms when RF power is applied to the RF coil and a high voltage spark is introduced into the flowing gas. An alternating current oscillates within the coil at a rate corresponding to the frequency of the generator (27 or 40 MHz). The RF oscillation of the current in the coil causes an intense electromagnetic field lying along the axis of the torch. A Tesla coil is used to introduce free electrons to the gas, which results in some electrons being stripped from argon atoms. These released electrons are then caught up and accelerated in the magnetic field, colliding with other argon atoms, releasing more electrons. The collision-induced ionization of the argon continues in a chain reaction, breaking down the gas into argon atoms, argon ions, and electrons, forming the inductively coupled plasma.

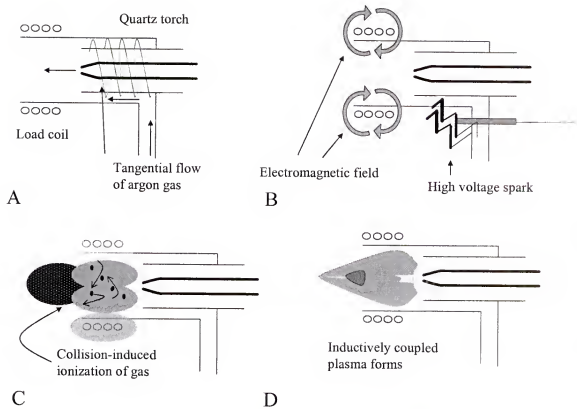


Figure 2-3. Formation of inductively coupled plasmas. A) Tangential flow of argon gas. B) Magnetic field is created and electrons are introduced. C) Free electrons cause collision-induced ionization of gas. D) Inductively coupled plasma forms.

The plasma is sustained within the torch and the load coil as long as RF energy is continually transferred into it.

The three most fundamental properties of the ICP are its gas temperature, reaching around 8000 K, its electron temperature reaching around 10,000 K, and its electron number density reaching around  $1-3 \times 10^{15}$  per  $\text{cm}^3$ . Figure 2-4 illustrates the temperature of the different regions or zones in the plasma. The high temperature coupled with the relatively long plasma-sample interaction times (2-3 ms) leads to nearly complete vaporization and atomization of the sample aerosol, which reduces the chemical and physical interferences in the plasma. The high electron number density reduces the ionization-type interferences commonly found in flame spectrometry. Furthermore, since the ICP is a robust electrical flame, its fundamental properties and analytical characteristics are not altered when the sample composition is altered.

### **The Ionization Process**

As the sample aerosol is introduced into the center of the plasma, it moves at a velocity that physically punches a channel through the center of the plasma discharge. The sample introduced then goes through a number of physical changes starting at the preheating zone and continuing through the radiation zone and into the analytical zone. The process of ionization involves desolvation of a liquid droplet, vaporization of the remaining solid particle, atomization of the vapor, and lastly ionization of the atoms. Figure 2-5 summarizes the conversion of a droplet to an ion in the ICP.

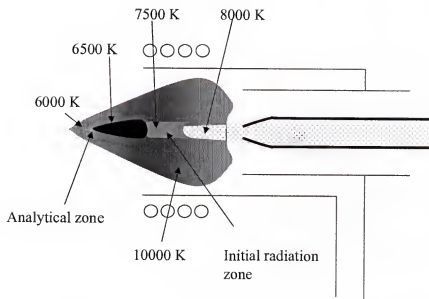


Figure 2-4. Temperature in the different zones in the inductively coupled plasma.  
Source: Montaser and Golightly (1992)

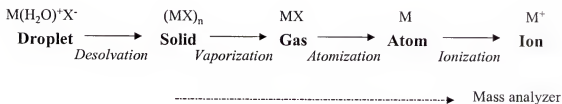


Figure 2-5. Ionization process in the ICP



The degree of ionization of the atom population in the plasma depends on the ionization temperature of the plasma, the electron number density of the plasma, the ionization energy of the analyte, and the partition functions for the atom and ion energy states.<sup>17</sup> The degree of ionization  $\alpha$  of an element is as follows<sup>17</sup>:

$$\alpha = \frac{n_i}{n_a + n_i} = \frac{\frac{(n_i n_e)}{n_a}}{n_e + \frac{(n_i n_e)}{n_a}} = \frac{K_M}{n_e + K_M} \quad (2-2)$$

where  $n_a$  is the number density of atoms ( $\text{cm}^{-3}$ ),  $n_i$  is the number density of ions ( $\text{cm}^{-3}$ ),  $n_e$  is the electron number density ( $\text{cm}^{-3}$ ), and  $K_M$  is the Saha equilibrium constant. The Saha equilibrium constant is dependent on the ionization temperature  $T_{ion}$ , and is expressed as follows<sup>17</sup>:

$$K_M = \frac{n_i n_e}{n_a} = 4.83 \times 10^{15} T_{ion}^{3/2} \frac{Z_i}{Z_a} \exp\left(-\frac{V_i}{kT_{ion}}\right) \quad (2-3)$$

where  $Z_a$  is the partition function of the atom (dimensionless),  $Z_i$  is the partition function of the ion,  $V_i$  is the ionization potential,  $k$  is the Boltzmann constant. Table 2-2 lists the degree of ionization calculated for different elements using the above equation, and values of  $n_e = 1.475 \times 10^{14} \text{ cm}^{-3}$  and  $T_{ion} \text{ (Ar)}$  of 6680 K.<sup>16-19</sup> The values at the table confirm that ICP is a good ionization source for most elements.

### Interfacing ICP and Mass Spectrometer

The interface between the ICP and the mass spectrometer is probably the most critical area in ICPMS system. The role of the interface is to transport the ions efficiently and consistently from the plasma, which is at atmospheric pressure, to the mass spectrometer analyzer, which is at approximately  $10^{-6}$  Torr. Figure 2-6 shows the typical interface schematics for coupling ICP to MS. The interface usually consists of two

Table 2-2. Ionization potential and degree of ionization of elements. (Montaser and Golightly, 1992)

| Element | Degree of Ionization* | Element | Degree of Ionization* |
|---------|-----------------------|---------|-----------------------|
| Cs      | 99.98                 | Co      | 94.83                 |
| Rb      | 99.98                 | Fe      | 96.77                 |
| K       | 99.97                 | Re      | 94.54                 |
| Na      | 99.91                 | Ta      | 96.04                 |
| Ba      | 99.96                 | Ge      | 91.64                 |
| Ra      | 99.95                 | W       | 94.86                 |
| Li      | 99.85                 | Si      | 87.9                  |
| La      | 99.91                 | B       | 62.03                 |
| Sr      | 99.92                 | Pd      | 94.21                 |
| In      | 99.42                 | Sb      | 81.07                 |
| Al      | 98.92                 | Os      | 79.96                 |
| Ga      | 99                    | Cd      | 85.43                 |
| Tl      | 99.38                 | Pt      | 61.83                 |
| Ca      | 99.86                 | Te      | 66.74                 |
| Y       | 98.99                 | Au      | 48.87                 |
| Sc      | 99.71                 | Be      | 75.36                 |
| V       | 99.23                 | Zn      | 74.5                  |
| Cr      | 98.89                 | Se      | 30.53                 |
| Ti      | 99.49                 | As      | 48.87                 |
| Zr      | 99.31                 | S       | 11.47                 |
| Nb      | 98.94                 | Hg      | 32.31                 |
| Hf      | 98.54                 | I       | 24.65                 |
| Mo      | 97.5                  | P       | 28.79                 |
| Tc      | 94.14                 | Rn      | 35.74                 |
| Bi      | 96.72                 | Br      | 3.183                 |
| Sn      | 96.99                 | C       | 3.451                 |
| Ru      | 97.93                 | Xe      | 5.039                 |
| Pb      | 97.1                  | Cl      | 0.4558                |
| Mn      | 95.87                 | Os      | 0.04245               |
| Rh      | 94.45                 | Kr      | 0.2263                |
| Ag      | 94.45                 | Ni      | 0.04186               |
| Ni      | 92.55                 | Ar      | 0.01341               |
| Mg      | 98.25                 | Fe      | 0.0001919             |
| Cu      | 91.59                 | Ne      | 0.000005468           |
|         |                       | He      | 1.007E-09             |

\*assuming local thermodynamic equilibrium  $T_{ion}(Ar)=6680K$ and  $n_e=1.47 \times 10^{14}/cm^3$

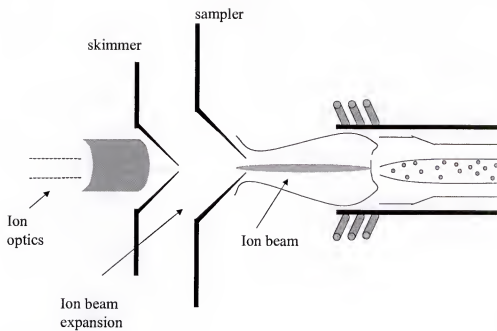


Figure 2-6. Typical ICP-MS interface.

metallic cones, each with very small apertures. The plasma flame usually flares out around the sides of the first cone. Much of the gas flow from the central channel of the torch containing the ionized sample aerosol is extracted by the aperture. The aperture diameter of the first cone ranges from 0.8-1.2 mm. The region behind the sampling cone is maintained at approximately 2 Torr. Gas expanding into this lower pressure reaches a velocity exceeding the local speed of sound in a distance of less than one aperture diameter. The temperature drops rapidly, and no reactions are possible to alter the composition of the sample. As the gas pressure and temperature rapidly decrease, the kinetic energy of the gas is converted into directed flow along the axis and a free jet is formed, bound by a shock wave known as the barrel shock. Another shock wave, the Mach disc is formed across the axis at a distance determined by the pressure ratio of the expansion and aperture diameter. The ions then pass through the second cone, called the skimmer cone, which is more sharply angled than the sample cone to minimize formation of a further shock wave at its edge. The temperature drops to around 200 K. Beyond the skimmer cone, the extracted ions enter a region where the pressure is low enough to ensure that the mean free path is longer than the system dimensions and the flow becomes random. To direct as many of the ions as possible, the skimmer is followed by electrostatic lens system. The ion lens usually includes a photon stop on the axis to prevent direct photons from the plasma reaching the ion detector and contributing to the background.

Figure 2-7 shows the interface for the Finnigan Mat Sola (the ICPMS used in this research). The interface is composed of a series of three cones through which the pressure drops from atmospheric pressure to approximately  $10^{-5}$  torr. The first cone is the

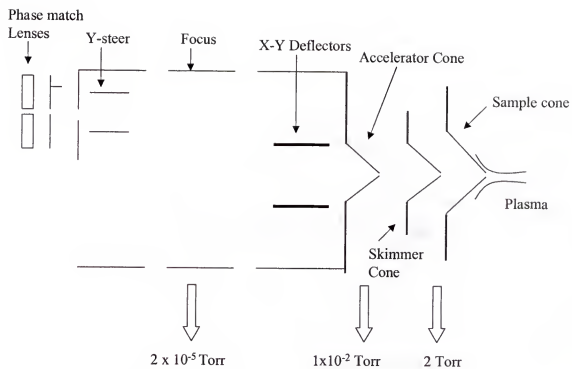


Figure 2-7. Schematic diagram of Finnigan Mat Sola ICP-MS interface.

sampling cone located approximately 14 mm from the end of the RF coil; the aperture has a diameter of 1.1 mm. The interspace behind the sample cone is kept at a pressure of 2-3 Torr by a single stage rotary pump. A skimmer cone located approximately 8 mm behind the sampling cone is used to select the center portion of the jet of plasma passing through the first aperture. The aperture at the end of this cone is 0.8 mm which is sufficient to allow most of the ions sampled from the plasma to pass through to the next stage of the vacuum system. At the same time, the cooler gases at the edge of the jet are also removed by the expansion chamber rotary pump. In the Finnigan Mat Sola ICPMS system, the skimmer cone is followed by an accelerator cone. The interspace between the skimmer and accelerator cones is pumped by a turbo pump at 330 l/s maintaining the pressure at  $10^{-3}$  torr. The accelerator cone acts as an electrode on which a voltage of -2 kV is applied. Ions passing from the skimmer cone are focused into the accelerator cone. A series of ion lenses then transfer the ion beam to the entrance aperture of a quadrupole mass spectrometer. These lenses are comprised of x-deflector plates, y-deflector plates, focus lenses, steering plates, and phase matching plates. These lenses are adjusted manually to maximize the ions arriving at the quadrupole.

### **Quadrupole mass spectrometer**

A quadrupole mass analyzer operates as a mass filter. The mass analyzer could be configured so that a stable path exists for ions of the desired mass. Other ions are deflected away from the axis and do not reach the detector. Figure 2-8 illustrates the schematic diagram of a quadrupole mass analyzer. The quadrupole is composed of four straight metal rods suspended parallel to and equidistant from the axis. These rods approximate a hyperbolic shape. Opposite pairs of the rods are connected together and

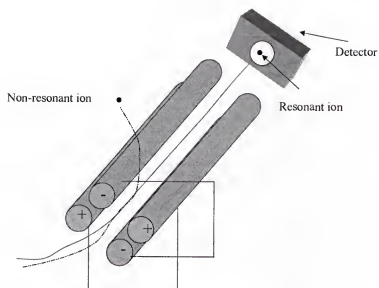


Figure 2-8. Schematic diagram of a quadrupole analyzer.

RF and DC voltages are applied to each pair. The mass transmitted by the quadrupole is determined by the amplitude of the RF and DC potentials fed to each pair of opposite rods. Both RF and DC potentials easily controlled electrically. Within limits of the time constants of the RF drive circuits, the selected mass may be scanned rapidly with rates up to 3000 mass units per second. Compared to other mass analyzers such as magnetic sectors analyzers, quadrupoles are more tolerant of higher operating pressures. Since the ICP operates at atmospheric pressure, using the quadrupole as a mass analyzer simplifies the vacuum requirements of an ICPMS. However, they also provide a limited mass resolution, one atomic mass unit. This resolution is sufficient to separate adjacent elemental and isotopic peaks but not enough to separate isobaric interferences.

### **Mass Detectors**

The detector converts the number of ions emerging from the mass analyzer into electrical pulses, which are then counted by its integrated measurement circuitry. The magnitude of the electrical pulses corresponds to the number of analyte ions in the sample aerosol. The two most commonly used detectors in ICPMS systems are the pulse counting Channeltron electron multipliers, used for low ion count rates, and the Faraday collector, used for high-count rates.

The Channeltron electron multiplier consists of an open glass tube with a cone at one end. The interior of the tube and cone are coated with a lead oxide semi-conducting material capable of generating electrons from ions impinging on its surface. The cone end of the tube is biased at a high negative potential while the opposite end of the tube is held at ground. The resistance of the interior coating varies continuously with position relative to each end. When a voltage is applied across the tube, a continuous gradient of potential exists inside the tube. When an ion hits the surface of the cone, one or more



secondary electrons are ejected. Due to the potential gradient, the secondary electrons move further into the tube towards the region closer to ground. As the secondary electrons hit other sections of the tube surface, more secondary electrons are emitted. The process is repeated many times, resulting in a discrete pulse containing as many as  $10^8$  electrons at the collector per ion striking the detector. Figure 2-9 summarizes the process of ion detection of the multiplier.

For analyses involving bulk concentrations of the analyte, Faraday cups are often used. Figure 2-10 shows a schematic diagram of the Faraday Cup Detector. The Faraday cup can be considered to be a conventional electrical detector. Its main component is a collector electrode enclosed in a cage called the Faraday cage. Ions impinging on the collector are neutralized by electrons drawn from ground after passage through a high-ohmic resistor. The voltage drop occurring across the standard resistor is a measure of the ion current. The voltage signal from the resistor is then amplified by a DC amplifier or a vibrating-reed electrometer. The collector is kept inclined with respect to the ion trajectory so that reflected ions or ejected secondary electrons do not escape the Faraday cage. The amplified ion current is a measure of the number of ions and the number of charges per ion. The Faraday cup detector is simple, inexpensive, rugged and reliable. They have high accuracy, constant sensitivity and very low electrical noise. However, the Faraday cup has a relatively long delay inherent in its amplification system. The Faraday therefore should be reserved for accurate measurement of slowly changing ion currents.

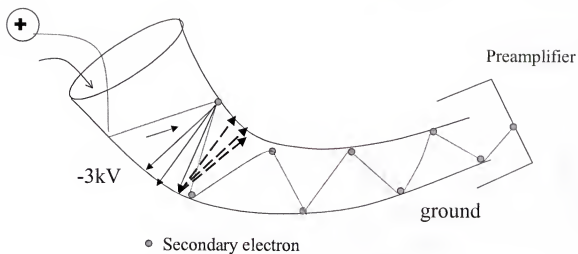


Figure 2-9. Schematic diagram of a Channeltron electron multiplier.

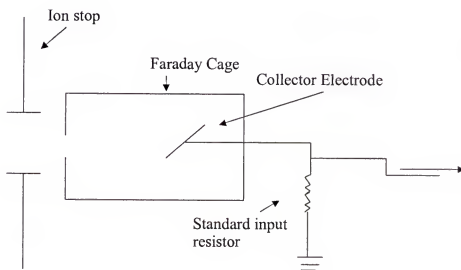


Figure 2-10. Schematic diagram of Faraday cup

## **Sample Introduction**

Sample introduction in ICPMS systems involves the conversion of liquid or solid samples into a fine-droplet aerosol suitable for complete ionization in the plasma. The sample introduction area of ICPMS has been called its weakness since only about 1-2% of the sample finds its way into the plasma<sup>20-21</sup>.

Although, there are many different means of introducing samples into the ICPMS, a common way of generating aerosols from liquids and dissolved solid samples is through a nebulizer and a spray chamber. The sample is pumped at an average of 1 ml/min via a peristaltic pump into a nebulizer. The peristaltic pump, a small pump with mini-rollers rotating at the same speed, feeds the sample into the nebulizer by applying constant motion and pressure to the sample in the tubing ensuring a constant flow of liquid. As the sample enters the nebulizer, it is broken up into a fine aerosol by the pneumatic action of the gas flow breaking the liquid into tiny droplets. The droplets are then fed into a cooled spray chamber. Larger droplets, greater than approximately 10  $\mu\text{m}$ , are impacted on the walls of the spray chamber or fall out due to gravity so that only small droplets make it to the plasma. Figure 2-11 shows a simplified representation of the separation of large and fine droplets in the Scott type-spray chamber.

### **Laser Ablation Inductively Coupled Plasma Mass Spectrometry**

Laser ablation was first used as a sample introduction for ICPAES in 1981 by M. Thompson and coworkers<sup>22</sup> and for ICPMS in 1985 by A.L. Gray<sup>23</sup>. Since then, LA-ICPMS has been used in a variety of applications involving materials such as glass, ceramics, metals, plastics, soils, and minerals<sup>1</sup>. Figure 2-12 illustrates the schematic diagram for LA-ICPMS systems. In LA-ICPMS, the laser beam is directed and focused

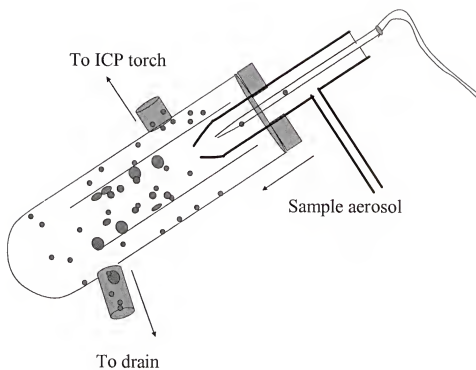


Figure 2-11. Schematic diagram of a Scott-type spray chamber.

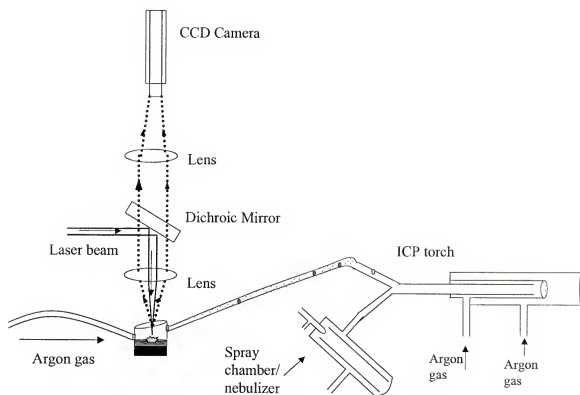


Figure 2-12. Schematic diagram of Laser ablation-ICPMS interface.

onto the sample. At irradiances of  $10^9$  W/cm<sup>2</sup> or greater, the laser-material interaction results in ejection of molecules, atoms and ions. The carrier gas, usually argon or helium, is used to transport the ablated material into the inductively coupled plasma, for atomization and ionization, and into the mass spectrometer for detection. LA-ICPMS has become a popular and indispensable analytical technique over the years. Advantages of the using the LA-ICPMS are as follows:

- Sample introduction via Laser Ablation gives LA-ICPMS the ability to sample diverse materials ranging from conducting and non-conducting inorganic and organic compounds in the form of solids or powders
- The focusing characteristics of lasers permit sampling of small selected areas, enabling localized microanalysis and spatially resolved studies
- There are no vacuum requirements in the ablation chamber
- Minimal sample preparation is required
- Rapid sample exchange and throughput is possible for routine analyses
- A minimal amount of sample (micrograms) is required for an analysis by LA-ICPMS
- Low detection limits (low parts per billion) and high sensitivity is achieved, providing that the ablated material is transported to the plasma with efficiency
- Compared to solution ICPMS, spectral interferences are reduced due to the reduction of H<sub>2</sub>O in the sample

Limitations of LA-ICPMS as a solid-sampling technique are as follows:

- LA-ICPMS lacks precision compared to other techniques for solid sampling such as SIMS and the Electron Microprobe<sup>24-25</sup>
- Elemental and isotopic fractionation may occur in the process of ablation, sample transport or ionization leading to inaccuracies in analysis
- Quantitative analysis using LA-ICPMS requires the use of matrix-matched standards
- Analysis of heterogeneous samples, usually overcome by sample dissolution in solution-ICPMS, may pose challenges for accurate analysis

### **Analytical Efficiency**

Another advantage of LA-ICPMS is that the sample introduction can be separated from the sample ionization. This allows optimization of both processes but also introduces three complex sets of parameters that can introduce noise and affect the overall precision and accuracy of the technique. These parameters affect sample ablation, sample transport and sample ionization. The overall efficiency of LA-ICPMS may be defined as the ratio of the number of analyte ions detected to the number of analyte atoms ablated, and is affected by sample ablation, sample transport and sample ionization.

### **Ablation Efficiency**

The ablation efficiency may be defined as the ratio of the mass of the material actually removed from the sample to the total mass of material irradiated with the laser. Sample ablation is affected by the laser operating parameters, wavelength, irradiance, beam diameter, pulse length, repetition rate, and ablation conditions such as ablation cell shape and volume, the nature of the scavenger gas used and the physical and chemical properties of the sample being ablated.

### **Transport Efficiency**

The transport efficiency may be defined as the ratio of the amount of ablated material that reaches the ICP to the amount of material actually ablated off of a sample. The transport efficiency is affected by the length of transport path, the transport gas nature and flow rate, and the size of the particles being transported. It has been reported that as sample particles are transported into the ICP by the carrier gas, particles with diameters greater than about 5  $\mu\text{m}$  may settle out due to gravity<sup>26</sup>. Smaller (ultra fine) particles (<5 nm) have been reported to be lost due to diffusion<sup>1</sup>. This particle size variation, which translates into a random arrival of particles in the ICP, is responsible for

the observed signal fluctuations since different particle sizes produce different ion signals.

### **Ionization Efficiency**

The ionization efficiency of the plasma may be defined as the ratio of the number of ions reaching the detector to the number of atoms introduced into the ICP. The ionization efficiency is affected by the nebulizer gas flow, the RF power, the coolant and intermediate gas flows, and the size distribution of the sample aerosol. Large particles may not be efficiently ionized in the ICP. Several studies have been reported focused on the effect of particle diameter on the plasma ionization efficiency in conventional solution nebulization ICPMS and ICPAES.<sup>27-29</sup> However, to date, there is no definitive understanding on which particle size is the maximum diameter completely vaporized and ionized in the ICP. For example, Knight reported that particles 3-7  $\mu\text{m}$  in diameter are not completely vaporized and ionized in the plasma during the analysis of silicates in ICP-AES.<sup>27</sup> On the other hand, in their systematic study on desolvated droplets in argon ICPs, Olesik and Fister reported the estimated largest size of the droplets allowing complete ionization in the plasma to be in the range of 10-20  $\mu\text{m}$ .<sup>28</sup> Furthermore, it has been reported that incompletely desolvated droplets affect plasma ionization and excitation conditions in a volume within about 1-2 mm of the droplet.<sup>29</sup> Finally, elemental fractionation in the ICP may also occur when large particles are present in the plasma and are vaporized and ionized incompletely.<sup>28,29</sup>

### **Quantitation Strategies**

Although solid reference materials such as glasses and brass made by NIST are available for calibration purposes, it is often difficult to apply them to the analysis of



other matrices. In the absence of matrix-matched standards, there are existing methods of calibration strategies used. Internal standardization is used to account for shot-to-shot variations in laser output power and aerosol transport losses in the ablation cell and transfer line. However, the use of internal standards in laser ablation is not as straightforward as in solution nebulization. The chosen internal standard has to be very similar to the analyte in physical properties so that both are affected in the same way by variations in the laser output power. The concentration of the chosen internal standard also has to be known. Another strategy that can be used is to simultaneously nebulize solution standards with the ablation of the sample to achieve matched plasma conditions.<sup>30</sup>

Methods of normalization can also be used to compensate for variations in the ablation process. The acoustic waves emitted in the ablation process may be monitored and used to account for variations in mass ablated.<sup>31</sup> This method improves the precision by a factor of 2, but does not account for aerosol transport losses from the ablation cell to the plasma, and is not commercially available. Another method of normalization is to use an aerosol mass monitor to correct for variations in the ablated material and sample transport<sup>32</sup>. The monitor consists of a piezoelectric microbalance sensor and an electrostatic precipitator that deposits aerosol particles onto the sensor. A disadvantage to this method is that the particle size, shape, velocity and composition may be altered when they are deposited in the sensor.

### **Nuclear Waste Samples**

There are currently 177 underground waste storage tanks at the Hanford site Pacific Northwest National Laboratory. These tanks contain approximately 53 million gallons of wastes collected over 50 years of plutonium production. The wastes include radioactive

isotopes, toxic chemicals, corrosive liquids, organic solvents, and other dangerous and hazardous substances.

The goal of the Department of Energy is to begin a process that will lead to the gradual closing of the waste tanks. Before the closure of the tanks, however, characterization, and treatment of the wastes are necessary.

The existing baseline method for characterization of the high level waste solids involves complete dissolution of the solids by a series of chemical treatments and then analysis with Inductively Coupled Plasma Atomic Emission Spectroscopy (ICPAES). In many instances, these baseline methods have been sufficient to meet the requirements for waste storage and safe site operation, but they will not be able to meet the more demanding requirements for rapid waste characterization and process monitoring needed for significant waste volumes. Generally, the baseline methods cannot provide rapid access to data and cannot provide high sample throughput. The baseline methods are also expensive due to the high labor intensity needed for sample preparation, handling and data analysis. The methods are not scalable to meet aggressive production and remediation requirements. Because of the high sodium nitrate and hydroxide concentrations typical in the tank waste, samples normally must be diluted several orders of magnitude to make them acceptable to the instrumentation. Thus, dilution decreases the analyte concentration below the limit of detection. Furthermore, dissolution of the wastes generates secondary wastes and expose staff to higher levels of radiation than desired.

Preliminary LA-ICPMS experience at Hanford with tank waste simulants have demonstrated that mass spectral data can be rapidly obtained without sample preparation. Data reduction was developed and proven effective for qualitative and semi-quantitative

agreement with the existing methods. A preliminary comparative analysis of time and cost factors also showed that the use of LA-ICPMS will reduce direct labor costs for analysis with about 20%-60% savings. The use of LA-ICPMS could also significantly reduce the elapsed time for analysis by an estimated 85% reduction. Furthermore, the use of LA-ICPMS will increase the process throughput under heavy laboratory demand by an estimated 16 to 160 times.

Before LA-ICPMS can be used routinely, it is important to demonstrate that its use will give limits of detection, accuracies and precisions comparable to the baseline methods. More importantly, it must be demonstrated that the method can produce analytical results from heterogeneous solids, similar to the retrieved tank waste, that are comparable to the baseline dissolution method.

There are two issues that must be addressed with regards to the properties of the nuclear waste as a sample independent of the method of analysis: sample heterogeneity and reference sample matching (matrix-matching). The existing procedure of tank wastes is to obtain a core sample from a 1-million gallon tank, equivalent to about only 0.000001 of the tank contents. When taken from an unstirred tank, there may be significant lateral variations missed by a single core. Portions of the core sample are then homogenized. A portion of about 0.5 g of the homogenized sample is then removed for dissolution, resulting in a further sample volume reduction by a factor of about 0.001. Furthermore, the waste samples are high granular and pasty in consistency with the possibility of non-stoichiometric composition of elements in the granules and paste. Another complication of working with the wastes is the variability of the samples encountered. Unlike other industrial applications where the sample composition is very reproducible, it is very

difficult to come up with standards that will match almost every kind of tank waste. To address this issue, a number of simulant materials representing key Hanford tank waste matrix categories were prepared by DOE. Simulant matrices were spiked with low-levels of a broad range of elemental constituents covering a significant portion of the mass spectral range pertinent to the waste materials. Several independent methods were evaluated to quantify differences in ablation efficiency between the unknown and the reference sample. One was to monitor the ablated particle plume using a particle size spectrometer to determine and compare the volume of the ablated material from the respective samples.<sup>3</sup> Table 2-3 shows the composition of the 4 different waste simulants used for this study.

Table 2-3. Estimated composition of the waste simulants used in these experiments.  
(source: DOE, PNNL)

| INFARM SIMULANT CONCENTRATIONS |          |          |          |
|--------------------------------|----------|----------|----------|
| INFARM<br>Element              | D<br>ppm | F<br>ppm | G<br>ppm |
| Ag                             | 6.25     | 25       | 100      |
| Al                             | 10       | 400      | 1500     |
| B                              | 0.4      | 6.25     | 25       |
| Ba                             | 400      | 1500     | 0.4      |
| Bi                             | 6.25     | 25       | 100      |
| Ca                             | 83000    | 83000    | 83025    |
| Cd                             | 25       | 100      | 400      |
| Ce                             | 1500     | 0.4      | 1.5      |
| Co                             | 1500     | 0.4      | 1.5      |
| Cr                             | 25       | 100      | 400      |
| Cs                             | 7000     | 7300     | 8400     |
| Cu                             | 25000    | 6.25     | 25       |
| Er                             | 1500     | 6250     | 25000    |
| Fe                             | 58300    | 59400    | 57900    |
| In                             | 0.4      | 1.5      | 6.25     |
| La                             | 25       | 100      | 400      |
| Li                             | 1500     | 0.4      | 1.5      |
| Lu                             | 0.1      | 250      | 100      |
| Mg                             | 6.25     | 25       | 100      |
| Mn                             | 100      | 400      | 1500     |
| Mo                             | 400      | 1500     | 0.4      |
| Na                             | 211300   | 211300   | 211300   |
| Nd                             | 400      | 1500     | 6250     |
| Ni                             | 67150    | 85900    | 60900    |
| P                              | 11900    | 10377    | 10377    |
| Pb                             | 25       | 100      | 400      |
| Pd                             | 1.5      | 6.25     | 25       |
| Pr                             | 0.4      | 1.5      | 6.25     |
| Rb                             | 100      | 25       | 6.25     |
| Rh                             | 0.4      | 1.5      | 6.25     |
| Ru                             | 1.5      | 6.25     | 25       |
| S                              | 6875     | 6875     | 6875     |
| Si                             | 400      | 1500     | 0.4      |
| Sm                             | 1.5      | 0.4      | 0.1      |
| Sr                             | 6.25     | 25       | 100      |
| Th                             | 6.25     | 15       | 0.4      |
| Ti                             | 6.25     | 25       | 100      |
| U                              | 0.4      | 1.5      | 15       |
| Y                              | 25       | 100      | 400      |
| Zr                             | 100      | 400      | 1500     |
| TOC                            | 74600    | 74600    | 74600    |
| Cl                             |          |          |          |
| NO <sub>3</sub>                | 285900   | 285900   | 285900   |
| NO <sub>2</sub>                | 70700    | 70700    | 70700    |

## CHAPTER 3

### SOURCES OF NOISE IN THE LA-ICPMS

Improving the precision of Laser Ablation Inductively Coupled Plasma Mass Spectrometry (LA-ICPMS), or any analytical technique for that matter, relies on the reduction of noise. Knowledge of the fundamental characteristics of noise and its origin in turn is essential in effective noise reduction. In this chapter, the sources of noise in ICPMS, particularly LA-ICPMS, are discussed and studied in detail.

#### Background

Noise in measured signals can be defined as unwanted fluctuations in the desired signal, which obscure its measurement. A good reference discussing the characteristics and measurements of noise is a chapter on signal and noise measurement in a book by Ingle and Crouch.<sup>8</sup>

Three sources of noise have been identified for the ICP mass spectra.<sup>20</sup> The first is white noise, which is present throughout the range of possible frequencies, forming the baseline of the noise spectrum. The second type of noise is flicker noise, also called  $1/f$  or excess low frequency noise, present predominantly at the low frequencies. The third type of noise is a group of random noise occurring as peaks at discrete frequencies in the noise power spectrum.

Both white noise and flicker noise have been associated with the nature of the sample aerosol as it is produced, transported and introduced into the plasma. These sources of noise occur from the local variations of analyte and solvent ion densities in the central channel of the ICP.<sup>21,28,32-33</sup> Noise peaks occurring at discrete frequencies

originate from sources such as the peristaltic pump pulsation, ICP power, AC power line pickups, and acoustic noise attributed to turbulence due to air entrainment at the torch mouth.

The stability of the ion source itself and the sample introduction to it have been studied by several groups, comparing both for ICPAES and ICPMS<sup>18, 30-31</sup>. However, none have thoroughly studied the noise sources in LA-ICPMS.

In this chapter, the noise spectra of LA-ICPMS using different ablation parameters were studied to determine the main sources of noise and consequently, the reason for the corresponding lack of precision, in LA-ICPMS.

### **Experimental Methods**

The laser ablation system used in this study contained a Nd:YAG laser (SL401, Spectron Laser Systems, Rugby, England) quadrupled to produce an output beam of 266 nm. The energy of the laser beam was measured by a laser energy detector (J3-02DW, Molelectron Corporation, California, USA) and kept constant at 1 mJ for all experiments producing an irradiance of  $4.4 \text{ GW cm}^{-2}$ . An x-y-z translation stage was used to move the sample at a speed of  $15 \text{ } \mu\text{m s}^{-1}$  during ablation. The laser ablation system was coupled to an ICPMS (Sola, Finnigan Mat, Hempstead, England), which was used to analyze the ablated particles. Table 3-1 summarizes the ICP and laser operating parameters used in the ICPMS analyses.

Time resolved analyses were performed by setting the mass analyzer (quadrupole) to scan the mass of interest over time. Dwell times could be varied at fixed time increments. For these experiments, dwell times used were 1 ms, 2 ms and 32 ms, resulting into scanning frequencies of up to 31.25Hz, 500 Hz and 1000 Hz respectively,

Table 3-1. Laser Ablation and ICPMS Operating Parameters

| <u>ICPMS Operating Parameters</u> |             |
|-----------------------------------|-------------|
| RF Power                          | 1100 kW     |
| Coolant gas flow                  | 15 l/min    |
| Intermediate Gas Flow             | 1.5 l/min   |
| Nebulizer Gas Flow                | 0.635 l/min |
| <u>Laser Ablation Parameters</u>  |             |
| Laser pulse energy                | 1 mJ        |
| Laser beam diameter               | 50 $\mu$ m  |
| Repetition rate                   | 5 Hz        |



with Nyquist frequencies of 16.75 Hz, 250 Hz and 500 Hz..

(Microcal Origin) was used to process the raw data in counts per second from the mass spectrometer. The dwell time could not be varied below 1 ms resulting in a maximum scanning range of 1000 Hz. This was deemed acceptable for the research since previous work on the ICPMS noise spectra rarely featured noise peaks at frequencies over 500 Hz.

The particle size distribution of the laser-ablated material produced was measured with an Aerosizer (Aerosizer LD, Amherst Process Instrument, Massachusetts, USA). The Aerosizer is capable of measuring particles in the range of 0.2-700  $\mu\text{m}$ , sampling up to 100,000 particles per second.

## Results

The aluminum signal at mass 27 was monitored over time for different samples: background or nebulized 5%  $\text{HNO}_3$ , 1 ppm aqueous solution of aluminum, laser-ablated pure aluminum metal, and laser-ablated waste simulant with a sodium nitrate matrix. The resulting mass signal was Fourier transformed to acquire the noise spectra from 0-250 Hz, scanning with a dwell time of 2 ms.

Figure 3-1A demonstrates that the excess low frequency noise is minimal when scanning for aluminum in nitric acid (or in other words a blank). Discrete noises were present at 60 Hz and its harmonics at 30 Hz, 120 Hz, 180 Hz, and 240 Hz due to pickups from the AC power line. White noise was present throughout the scanning frequencies.

Figure 3-1B shows that excess low frequency noise is present for aluminum for a solution of 1ppm aluminum. The solution was introduced by a Meinhardt nebulizer and the resulting aerosol passed through a cooled Scott-type spray chamber. The excess low

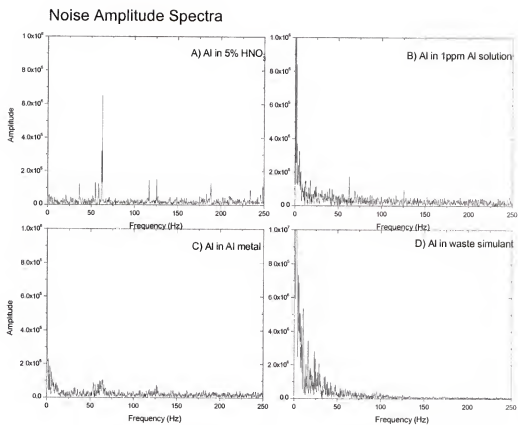


Figure 3-1. Noise amplitude spectra of aluminum in A) background, 5%  $\text{HNO}_3$ , B) 1 ppm Al solution, C) pure Al metal, and D) waste simulant.

frequency noise was present through to about 60 Hz. The magnitude of white noise is slightly increased and discrete noise peaks were present due to the AC power line pick-ups.

Figure 3-1C shows that excess low frequency noise is also present for aluminum particles introduced into the ICP via laser ablation of solid aluminum metal. The excess low frequency noise was present to about 20 Hz. Peaks at 60 and 120 Hz were also present due to AC line power pick ups.

Finally, Figure 3-1D demonstrates a significant increase in excess low frequency noise for aluminum in laser-ablated waste simulant. The excess low frequency noise continued through to about 120 Hz.

These results suggest that sample introduction was a major source of low frequency noise. Furthermore, sample introduction via laser ablation resulted in a significantly greater excess low frequency noise especially when the laser-ablated material being analyzed had a wide size distribution. Figure 3-2 shows the particle size distribution of the aerosol resulting from the ablation of aluminum metal and waste simulant. Ablation of aluminum metal resulted in particles with a mean particle diameter of 0.4  $\mu\text{m}$  and the largest particle present had diameters of about 1  $\mu\text{m}$ . On the other hand, ablation of the waste simulant yielded particles with a mean diameter of 1  $\mu\text{m}$ , with the largest particles having a diameter of about 4.5  $\mu\text{m}$ . It is important to note that ablation of pure metals into the ICPMS yielded less excess low frequency noise than the nebulization of 1 ppm solution into the ICP. A possible explanation for this is that the ablation of pure aluminum metal yielded particles with smaller or more uniform size distribution.

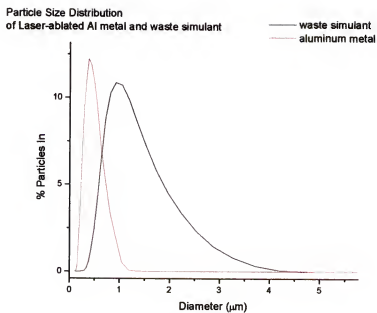


Figure 3-2. Particle size distribution of laser-ablated pure aluminum metal and waste simulant obtained using the API Aerosizer.

To verify that the excess low frequency noise was caused by variation in particle size distribution and random fluctuations caused by large particles, an inertial impactor was used to cut off larger particles from the ablated material being introduced into the ICPMS. (the details of this experiment are further discussed in Chapter 5). Figure 3-3 shows the noise spectra for aluminum in the waste simulant introduced via laser ablation with and without filtering out the larger particles. For this particular experiment, the scanning frequency was kept at 31.25 Hz yielding a Nyquist frequency of 15.75 Hz. Since the emphasis of the study was low frequency noise, this frequency range was used. The results show that the excess low frequency noise was reduced when larger particles were filtered out from the laser-ablated material. These results further confirmed the idea that the presence of larger particles and the existence of a wide size distribution was the cause of additional flicker or excess low frequency noise.

The noise amplitude spectra of the ICPMS signal resulting from the ablation of waste simulant was taken with and without the simultaneous nebulization of nitric acid, which required the use of a peristaltic pump. This experiment was performed to determine if the use of the pump produced any source of noise and if the simultaneous introduction of a solution into the plasma during laser ablation could reduce the low frequency noise. Figure 3-4 shows the results for this experiment performed for 2.5 Hz and 5 Hz to determine if the repetition rate of the laser affected the noise spectra. The results showed that the peristaltic pump did not introduce any specific noise peaks to the ICP mass signal. Furthermore, the simultaneous nebulization of the nitric acid actually reduced the low frequency noise. The repetition rate of the ablation laser did not affect the noise significantly.

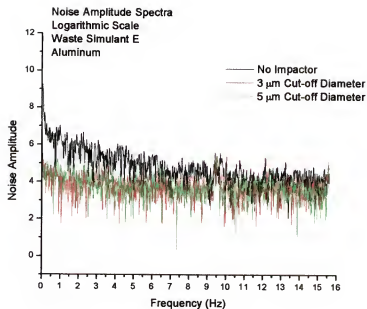


Figure 3-3. Noise amplitude Spectra of LA-ICPMS signal for Al in waste simulant with the use of a cut-off filter and without.

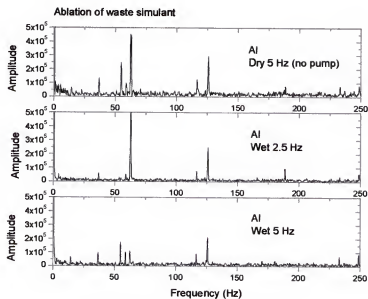


Figure 3-4. Noise amplitude spectra of LA-ICPMS signal of waste simulants using dry plasma and wet plasma.

### **Conclusion**

The results of these experiments showed that the dominant source of noise in LA-ICPMS was flicker or excess low frequency noise. Fluctuations in signal were introduced primarily by the presence of large particles in the laser-ablated material, and by a wide particle size distribution in the sample aerosol reaching the ICP. Excess low frequency noise in the LA-ICPMS analysis could be reduced by creating a sample aerosol with the narrowest size distribution possible and with the smallest mean diameter possible.

## CHAPTER 4

### PARTICLE SIZE DISTRIBUTION STUDIES OF LASER ABLATED MATERIAL

The previous chapter demonstrated that the limiting source of noise in LA-ICPMS is flicker or excess low frequency noise attributed to variations in the nature of the sample as it is created, transported and introduced into the plasma. The ideal sample aerosol for ICPMS can be described as consisting of fine mono-disperse particles traveling at a uniform velocity. Due to the complex nature of laser-solid interaction, the sample aerosol formed in laser ablation is far from ideal. The goal of this chapter was to find the optimum laser wavelength, energy and irradiance which would create the optimum size distribution of ablated particles for sample introduction into ICPMS, with minimum transport losses and best ionization efficiencies in the plasma, which in turn would result in the best precision and accuracy in ICPMS analysis of different materials.

#### **Background**

The size of particles ablated from a sample is dependent primarily on laser-solid interaction. Laser-solid interaction is in turn affected by several factors: laser wavelength, irradiance, spatial and temporal profile of the laser beam, sample characteristics such as heat capacity, thermal conductivity, heat of vaporization and melting and boiling points, and ablation conditions such as the size and shape of the ablation cell and the nature and flow rate of the transport and scavenger gas.

Several studies have been made on the effect of these laser parameters on the particle size distribution of the laser-ablated material and its corresponding effect on the ICPMS signal.



Geertsen and coworkers made a comparison between infrared and ultraviolet laser ablation, and the corresponding implication for solid sampling ICPMS.<sup>34</sup> The 355 nm, 532 nm and 1064 nm wavelengths of the Nd:YAG were used along with a 193 mm ArF and 308 XeCl to ablate a variety of materials including copper. Results showed that the mass ablated by a UV laser was considerably larger than for an IR laser. Selective vaporization was also less likely for UV laser sampling and the authors concluded that UV laser sampling was superior to IR laser sampling in terms of reproducibility, matrix effects, spatial resolution, quantitation, and sensitivity.

Montelica-Heino and co-workers investigated the fundamental processes taking place in UV and IR ablation of glassy materials.<sup>35</sup> Two separate Nd:YAG lasers were used for the study, the first operated at 266 nm with an energy of 4 mJ, and the second operated at 1064 nm with an energy of 250 mJ. Glassy materials with different compositions of silicon, calcium and aluminum were ablated. The ablation products were collected on ultra pure microfiber filters and characterized by SEM. Results revealed that the material created by ablation with the IR laser included beads and fragments from 2-20  $\mu\text{m}$ , and that the particles created by UV ablation were much smaller in diameter.

Alexander and coworkers investigated the relationship between laser parameters, particle size distributions and analytical results as determined by precision and accuracy.<sup>3</sup> The laser parameters that produced the best analytical results corresponded to the generation of smaller particle distributions.

Figg and coworkers used a 532 nm Nd:YAG to ablate glass samples and revealed that the particle size distribution shifted to larger sized particles when the laser pulse energy and irradiance increased.<sup>36</sup>

Jeong used an optical particle counter to measure the particle size distribution of glass samples for different laser ablation conditions with a 266 nm laser.<sup>37</sup> Results showed that although particle size distribution changed with power density, the laser beam diameter was a more influential parameter in terms of efficient particle generation.

Although several studies have been made on the particle size distribution of laser-ablated material, comparisons have been made using entirely different ablation parameters, such as irradiance or laser beam diameter. In this chapter, studies were performed on laser-ablated material made under similar conditions. Three wavelengths of a single Nd:YAG laser were used to ablate different materials of different matrices. The optics used to focus the laser, the ablation chamber, and the rastering speed were kept constant throughout the experiments.

### **Experimental Methods**

Dichroic mirrors and optical filters were used to isolate each wavelength, 1064 nm, 532 nm, and 266 nm, at a time from the Spectron SL 401 Nd:YAG laser. The resulting beam used for a particular ablation was focused through a set of lens on the ablation chamber. The laser focusing position was varied for each wavelength to obtain the smallest possible beam spot on the sample, approximately 40 x 60  $\mu\text{m}$  for UV and IR beams. The energy of the laser beam was measured by a power meter (Molelectron) and kept constant at 1 mJ unless stated otherwise. The laser was fired at a repetition rate of 5 Hz. An x-y-z translation stage was used to move the sample during ablation, with a rastering speed of 15  $\mu\text{m/s}$ . The ablated particles were transported by argon gas flowing through the ablation chamber and into the particle sizer through a plastic tube 1.5 m long and 0.48 cm inner diameter. This tubing is exactly the same tubing the ablated particles

pass through in an ICP analysis. The argon gas flow was kept at 0.365 l/min, which was determined to be the optimum flow rate for LA-ICPMS analysis of different materials. A XeCl laser at 308 nm was also used to ablate the materials using the same ablation conditions that were used for the Nd:YAG.

An Amherst Process Instrument Aerosizer LD (Hadley, MA) was used to size the particles produced during laser ablation. The principle behind the operation was the aerodynamic time of flight. The Aerosizer was capable of measuring particles in the range of 0.2-700  $\mu\text{m}$ , with sampling rates up to 100,000 particles per second. The Aerosizer software had the capability of presenting the particle size distribution with respect to the percentage of particles in each size range, or with respect to the number of particles in each size range. The latter information, along with the sample density, assuming the particles are spherical, was used to calculate the approximate mass of the ablated material.

Two other optical particle-counting systems were used on some experiments, the Lasair 1001, and Lasair II-310A (Particle Measurement Systems, Colorado, USA). Both operated based on particle scattering. Lasair 1001 was capable of measuring particles from 0.2-2.0  $\mu\text{m}$ , while Lasair II-310A was capable of measuring particles from 0.3-25  $\mu\text{m}$ . Each instrument had seven size channels.

The metal foils used were 99.8% metal and were 0.05 mm thick (Alfa Aesar, Massachusetts USA). The metal powders (Alfa Aesar, MA USA) were spread evenly on double sided tape (3M, Minnesota USA) on a glass slide. The glass standards used were NIST standard reference materials 610, 611, and 614. The waste simulants were provided by the Pacific Northwest National Laboratory.

## Results

### Effect Laser Wavelength

The effect of varying the laser wavelength on the size distribution of laser-ablated material was investigated. The irradiances used for the ablation were  $4 \text{ GW/cm}^2$  for 1064 nm, 308 nm, and  $2 \text{ GW/cm}^2$  for 532 nm. Different laser wavelengths were used to ablate different matrices. The corresponding effect on the particle size distribution was observed.

The experiments performed revealed that ablation with 1064 nm laser generally produced particles with larger mean diameters than ablation with 532 nm and 266 nm. However, this was not the case for all matrices. Figure 4-1A shows the mean particle size diameters resulting from ablation of different metal sheets with the four laser wavelengths. For all metals, ablation with 1064 nm resulted in much larger particle diameters. Figure 4-2A shows the mean particle diameters for laser-ablated metal powders. Ablation with 1064 nm generally produced larger particles. Ablation with 532 was inefficient especially for the titanium metal and silicon wafer, where the particles created from the ablation were below the detection limit of the Aerosizer. The corresponding mass ablated for ablation of both metals and powders is also presented in Figures 4-1B and 4-2B.

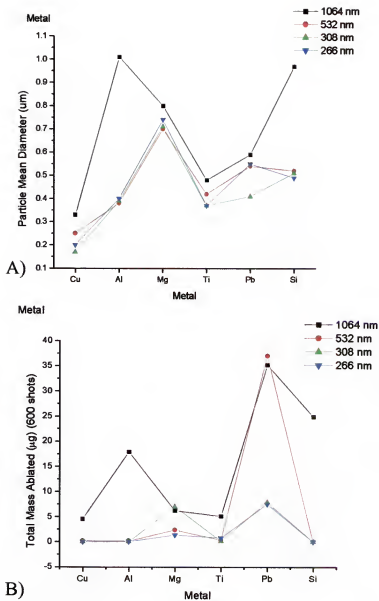


Figure 4-1. Ablation of different metals with 1064 nm, 532 nm, 308 nm and 266 nm.  
 A) Particle size distribution. B) Total mass ablated for 600 shots.

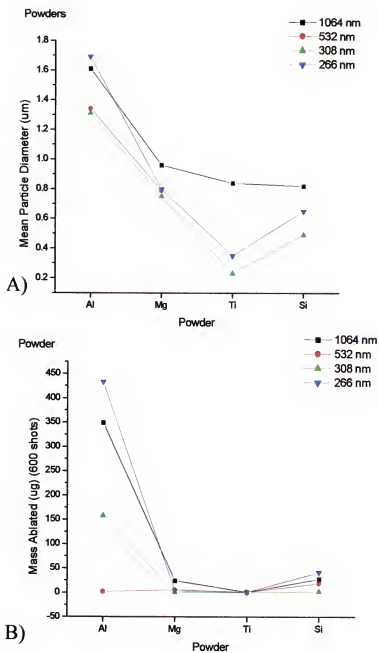
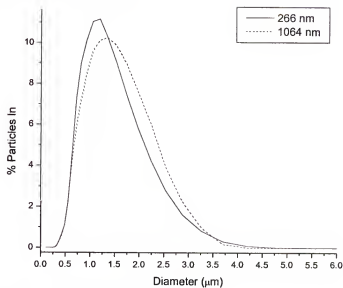


Figure 4-2. Ablation of different powders with 1064 nm, 532 nm, 308 nm, and 266 nm.  
A) Particle size distribution. C) Total mass ablated for 600 shots.

A waste simulant (Formula G) was also ablated with 1064 nm and 266 nm at  $4 \text{ GW/cm}^2$ ; 532 nm was not used since ablation with it produced particles below the detection limit of the Aerosizer. The resulting particle size distributions for ablation of the waste simulant with 1064 and 266 nm are shown in Figure 4-3A. The particles created from the 1064 nm beam had a mean diameter of  $1.6 \text{ }\mu\text{m}$  with particles up to about  $6.3 \text{ }\mu\text{m}$  in diameter, while the material created by the 266 nm laser had a mean diameter of  $1.4 \text{ }\mu\text{m}$  with particles up to  $5.2 \text{ }\mu\text{m}$  in diameter. The average mass ablated from the waste simulant by a single shot of laser at an irradiance of  $4 \text{ GW/cm}^2$  was calculated to be 64 ng and 30 ng for 266 nm and 1064 nm respectively. Figure 4-3B shows the total mass of ablated material accumulated for ablation with both wavelengths for 100,000 laser shots. Unlike the metals and the powders, ablation of the waste simulant with 1064 nm did not yield a greater mass ablated than with 266 nm. Moreover, the transport efficiencies of the particles created by ablation with 266 nm and 1064 nm were calculated by measuring the difference between the number and mass of ablated particles reaching the Aerosizer and the mass ablated from the sample. 20% and 23% of the mass ablated from the sample actually reached the Aerosizer for 266 nm and 1064 nm respectively. Figures 4-4 and 4-5 show scanning electron microscope (SEM) images of the laser-ablated waste simulant using 266 nm and 1064 nm respectively using irradiances of  $4.4 \text{ GW/cm}^2$  for both. The images revealed that the particles were not spherical, with UV created particles having smaller cross sections and more clusters of smaller particles. On the other hand, the IR created particles were generally bigger and massive.

Laser-ablated waste simulant



Laser-ablated waste simulant

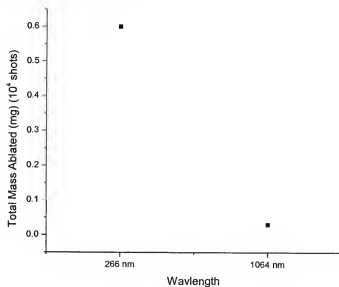


Figure 4-3. Waste simulant ablated with 1064 nm and 266 nm.

A) Particle size distribution. B) Total mass ablated for  $10^4$  shots.



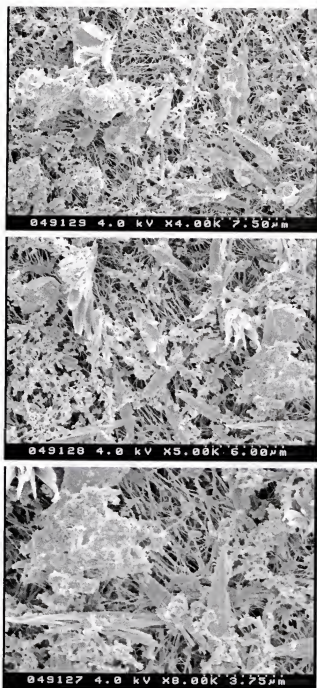


Figure 4-4. SEM images of 266 nm laser-ablated waste simulant.

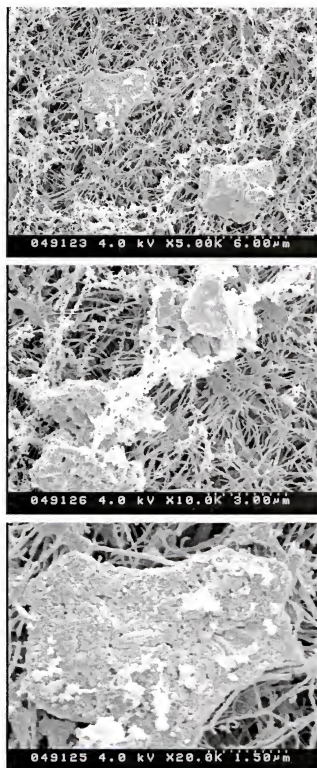


Figure 4-5. SEM images of 1064 nm laser-ablated waste stimulant.

ICPMS analysis of the laser-ablated waste simulants were performed. The tube connecting the ablation cell to the Aerosizer was simply connected to the ICP torch. The signal for aluminum and neodymium were monitored with respect to time for both wavelengths. Figure 4-6 shows the time resolved signal for Al and Nd using 266 nm and 1064 nm for ablation. The signal intensity of neodymium from the ablation with 266 nm was roughly three times greater than with 1064. The signal intensity of aluminum from the ablation with 266 nm was also significantly bigger than ablation with 1064 nm. The % RSD however was larger for 266 nm, 15% and 20% for Al and Nd, than that for 1064 nm, 7% and 10% for Al and Nd. A possible explanation for the higher fluctuations of material ablated with the use of 266 nm beam was that the 266 nm wavelength was prone to more shot-to-shot fluctuation. Furthermore, the sample being ablated, waste simulant, was highly heterogeneous and there may have been differences in the mass ablated per shot.

### **Effect of Laser Irradiance**

The effect of varying the laser irradiance on the particle size distribution of the laser-ablated material was investigated. A piece of copper metal was ablated with 1064 nm and 266 nm while varying the irradiance by keeping the beam diameter constant but varying the laser pulse energy. For ablation with both 1064 and 266 nm, the mean particle diameter increased with increasing irradiance (see Figure 4-7) for laser ablation of copper. ICPMS measurements of the laser-ablated copper was also performed while varying the laser irradiance. Figure 4-8 shows the ICPMS signal intensity as a function of laser irradiance. For a specific laser wavelength, the ICPMS signal decreased as the laser

irradiance was increased, and as the mean particle diameter of the ablated material increased. The % RSD achieved for all

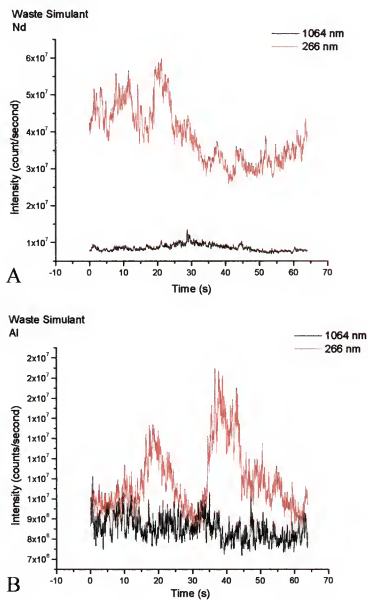


Figure 4-6. Time-resolved ICPMS signal for ablation of waste simulant using 266 nm and 1064 nm lasers. A) Nd B) Al.

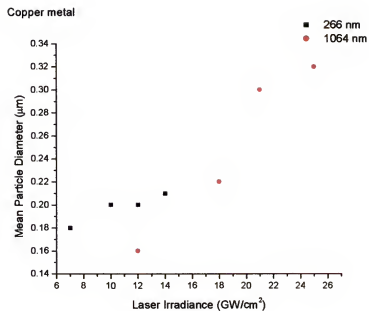


Figure 4-7. Effect of laser irradiance on mean particle diameter.

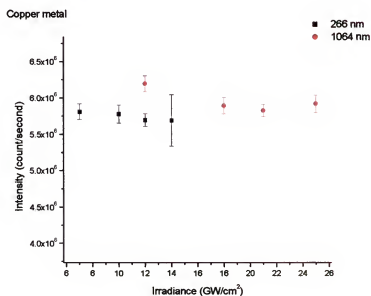


Figure 4-8. Effect of increasing laser irradiance on ICPMS signal intensity and stability.

the irradiances for both wavelengths were within the range of 1.5-2% with the exception of 266 nm at 14 GW/cm<sup>2</sup> where the % RSD obtained was 6%. A possible explanation for this is that as the laser irradiance increased, the plasma formed on the surface of the sample thickened optically, absorbing a bigger fraction of the laser beam, and thereby resulting in less efficient ablation.

### **Effect of Sample Matrix Properties**

Ablation of different metal foils with different thermal properties revealed that the mean particle diameter increased with increasing sample thermal conductivity and decreasing melting and boiling points. This was true for ablation using both 1064 nm and 266 nm. The same experiments were also performed for powders with different thermal properties. The results also revealed that the mean particle diameter increased with increasing sample thermal conductivity and decreasing melting and boiling points. Figure 4-9 shows the mean particle diameters for the different metals and powders using both 1064 nm and 266 nm.

The particle size distribution of the laser-ablated material did not only vary with the chemical composition of the matrix but also with the physical and optical properties of the sample. For instance, ablation of aluminum powder resulted in particles with a size distribution significantly different than the ablation of aluminum metal. Figure 4-10 shows the particle size distribution of laser-ablated aluminum in the form of metal sheet and powder. Ablation of the aluminum powder yielded larger particles and wider distributions than ablation of the metals. This was true for all the laser wavelengths.

Considering the same matrix, the color of the sample also affected the particle size distribution of the laser-ablated material. Three similar reference glass standards from NIST were ablated at 4.4 GW/cm<sup>2</sup>, NIST 611 (dark blue in color, with trace metals

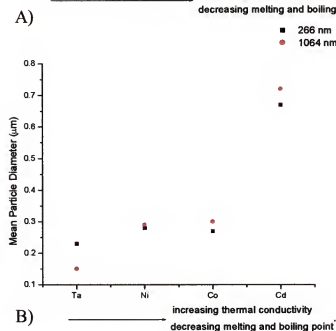
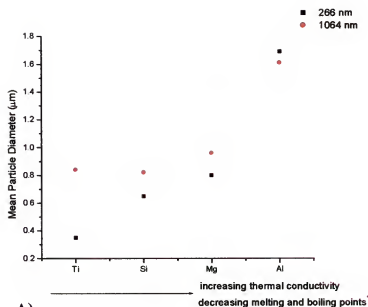


Figure 4-9. Particle size distribution of laser-ablated material as a function of sample thermal conductivity and melting and boiling points.  
A) Metals sheets. B) Metal powders.

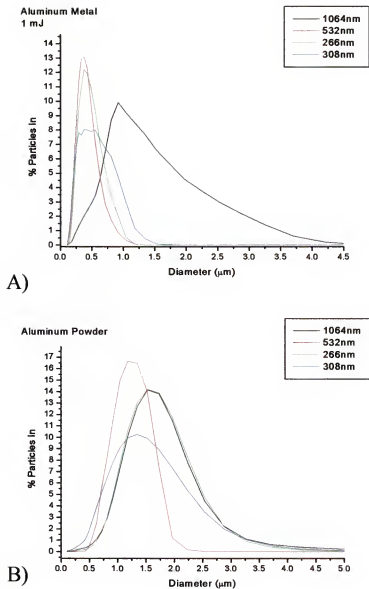


Figure 4-10. Particle size distribution of laser-ablated aluminum. A) Aluminum metal; B) Aluminum powder.



>200mg/kg), NIST 612 (light blue in color, with trace metals 30-65 mg/kg), and NIST 614 (translucent white in color, with trace metals less than 1 mg/kg). Figure 4-11 illustrates the particle size distribution of the ablated material for these three glasses. These results show that ablation of NIST 614, the lightest in color and possessing the lowest concentrations of trace metals present, had the smallest mean particle diameter. Accordingly, the ablation of NIST 611, the darkest in color, possessing the largest concentrations of trace metals yielded the widest distribution with the largest mean particle diameter. A possible explanation is that NIST 611, the darkest in color, absorbed a greater fraction of the laser beam than the other two glasses. The difference in the particle size distribution of the three glasses indicated further the need for matrix-matched standards in LA-ICPMS. Most analyses of glassy or geological materials are performed using these glass standards for the calibration curve. However, if the ablation of these glass standards yield particles of different distributions, the corresponding ICPMS signals may also vary. Thus, there is a need to correct for variations in particle size distribution between samples or standards.

Finally, the particle size distribution of the material resulting from the ablation of powders, metal sheets, and glasses were compared. Figure 4-12 shows that under similar ablation conditions, the ablation of metals yielded particles with the narrowest distributions, while glassy materials produced the widest particle size distributions.

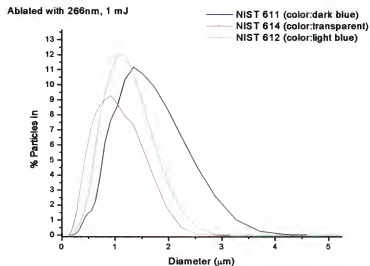


Figure 4-11. Particle size distribution of laser-ablated NIST glass standards.

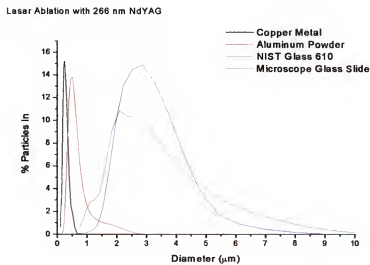


Figure 4-12. Particle size distribution of different matrices.

## Conclusion

The results from these studies confirmed that the particle size distributions of laser-ablated materials affected the intensity and stability of ICPMS signals. Particles that were larger in diameter and were of wider size distribution cause more signal fluctuations, thus decreasing precision in ICPMS. Ablation parameters can be optimized to reduce the particle size distribution of the laser-ablated material with consideration to the properties of the sample matrix. The following generalizations can be made:

- Ablation with 1064 nm generally yielded the largest mean particle diameter for different metal sheets and powders
- The mean particle diameter of the ablated-material increased with increasing laser irradiance (constant beam diameter and increasing laser energy)
- The corresponding ICPMS signal of the laser-ablated material decreased with increasing laser irradiance
- The mean particle diameter and total mass ablated for metals increased with increasing sample thermal conductivity and decreasing melting and boiling points
- Metals generally produce narrower distributions than powders and glasses
- Ablation of darker-colored glasses produced larger particles than ablation of lighter-colored glasses

Despite these generalizations, extensive optimization of ablation parameters must still be made prior to actual analysis as sample matrix properties affect the quality of the ablation material.

## CHAPTER 5

### USING AN INERTIAL IMPACTOR TO IMPROVE PARTICLE SIZE DISTRIBUTION OF LASER-ABLATED MATERIAL

The previous chapters have established that the limiting source of noise in LA-ICPMS originates from the nature of the sample aerosols as they are produced, transported and ionized. The goal of this chapter was to improve the quality of the laser-ablated material introduced into the ICPMS. An inertial impactor was used to filter out larger particles from the sample aerosol to reduce signal fluctuations in the ICPMS. As a result, the precision and accuracy of LA-ICPMS analyses were improved.

#### **Background**

The variation in the size of the laser-ablated particles affects both the efficiency of sample transport and analyte ionization. It has been reported that as sample particles are transported into the ICP by the carrier gas, particles with diameters greater than about 5  $\mu\text{m}$  may settle out due to gravity.<sup>21,23,26</sup> Smaller (ultra fine) particles (<5 nm) have been reported to be lost due to diffusion<sup>1</sup>. This particle size variation, which translates into a random arrival of particles in the ICP, is responsible for the observed signal fluctuations, since different particle sizes produce different ion signals. At the same time, larger particles may also not be efficiently ionized in the ICP. Several studies have been reported focused on the effect of particle diameter on the plasma ionization efficiency in conventional solution nebulization ICPMS and ICPAES.<sup>18, 27-29</sup> However, to date, there is no definitive understanding on which particle size is the maximum diameter completely vaporized and ionized in the ICP. For example, Knight reported that particles 3-7  $\mu\text{m}$  in

diameter are not completely vaporized and ionized in the plasma during the analysis of silicates in ICP-AES<sup>27</sup>. On the other hand, in their systematic study on desolvated droplets in argon ICPs, Olesik and Fister reported the estimated largest size of the droplets allowing complete ionization in the plasma to be in the range of 10-20  $\mu\text{m}$ .<sup>28</sup> Furthermore, it has been reported that incompletely desolvated droplets affect plasma ionization and excitation conditions in a volume within about 1-2 mm of the droplet.<sup>26</sup> Finally, elemental fractionation in the ICP may also occur when large particles are present in the plasma and are ionized incompletely.<sup>26, 34, 36, 37</sup>

With these considerations in mind, the ideal aerosol to be introduced into the plasma and undergoing complete vaporization and ionization during its residence time in the plasma should consist of small, mono-disperse particles. Due to the complex nature of the laser-solid interaction and aerosol transport, the sample aerosol formed in laser ablation ICPMS is far from ideal and the major cause of instability observed in the signal.

In solution nebulization ICPMS, it is known that flicker noise is minimized when the sample aerosol is passed through a Scott-type spray chamber.<sup>38</sup> Most nebulizers produce aerosols which are polydisperse with droplets reaching up to 100  $\mu\text{m}$ . The Scott-type spray chamber removes larger droplets by turbulent deposition on the inner walls of the chamber. This reduces random fluctuations in signal intensity. In Laser Ablation ICPMS, the ablated material does not go through the spray chamber but is directly introduced into the plasma.

Several attempts have been made to alter the particle size distribution of laser-ablated material. Ablation parameters, including laser wavelength, beam diameter and irradiance, transport gas flow rate, and ablation cell designs have been optimized to limit

particle size distributions to a small, narrow range of diameters.<sup>30, 36, 18-20</sup> In a study of elemental fractionation effects, Figg et al<sup>36</sup> used a tubing insert to remove larger-sized particles from the transport tube before the ablated material entered the plasma. Guillion and Gunther<sup>39</sup> used mineral wool to filter various fractions of the laser-induced aerosol to study the effect of particle size distribution on ICP-induced elemental fractionation in ICPMS. This approach, however, resulted in the removal of smaller particles as well as larger particles with a consequential reduction of the detected signal intensity. In a recent study, Guillion, Kuhn and Gunther<sup>40</sup> described a particle separation device based on the action of centrifugal forces in a thin coiled tube to filter out larger particles from laser ablated material, thus reducing elemental fractionation effects in the ICP. The cut-off size of the device could be adjusted from 0.3 to 1  $\mu\text{m}$  depending on the number of turns in the Tygon separation coil.

### **Operating Principle of the Inertial Impactor**

An inertial impactor was used to remove larger particles from the ablated material to serve as the counterpart of a spray chamber in LA-ICPMS. The ablated material was transported from the ablation cell through the inertial impactor and into the ICPMS. As the ablated material passed through the impactor nozzle, it was directed onto a flat plate, more commonly known as the impaction plate. The plate deflects the aerosol flow resulting in an abrupt 90° bend in the flow streamlines. Smaller particles follow the streamlines, remaining airborne, and flow out of the impactor into the ICP. Figure 5-1 illustrates the schematic diagram of the impactor nozzle. The collection efficiency of the impactor is governed by the Stokes number,  $Stk_{50}$ , or the impaction parameter, defined by the equation:

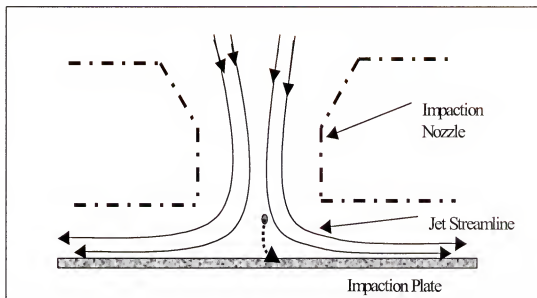


Figure 5-1. Schematic illustration of an inertial impactor nozzle.

$$Stk_{s0} = \left( \frac{\tau U}{D_j} \right) = \left( \frac{\rho_p d_{s0}^2 U C_c}{9 \eta D_j} \right) \quad (5-1)$$

where  $\tau$  is the relaxation time (s) or the time required for a particle to adjust to its velocity,  $U$  is the gas velocity (m/s),  $D_j$  is the impactor jet diameter (or nozzle diameter) (m),  $\rho_p$  is the particle density ( $\text{kg/m}^3$ ),  $d_{s0}$  is the particle diameter (m),  $C_c$  is the Cunningham correction factor (approximately 1, dimensionless) which corrects for the “slip” in the velocity of the gas at the particle surface, and  $\eta$  is the transport gas viscosity ( $\text{kg/m}\cdot\text{s}$ ). For a rectangular jet impactor, the equation can be expressed as:

$$d_{s0} \sqrt{C_c} = \left[ \frac{9 \eta W^2 L (Stk_{s0})}{\rho_p Q} \right]^{1/2} \quad (5-2)$$

where  $Q$  is the transport gas flow rate ( $\text{m}^3/\text{s}$ ),  $W$  is the nozzle slit width (m), and  $L$  is the jet length (m).

When the Stokes number is 0.59, the particle diameter satisfying equation 1 is the cut-off diameter, and the collection efficiency is 50%. As shown by figure 5-2, which illustrates the ideal and actual impactor cut-off curves, the mass of the particles larger than the cut-off size that get through equals the mass of the particles below the cut-off size that are collected. Thus, different slit widths for the impactor nozzle can be calculated based on the desired cut-off diameter, the nature of the carrier gas, the carrier gas flow rate and the density of the particles being sampled.

An advantage of using the inertial impactor to filter out larger particles is that the cut-off diameter can be easily changed with accuracy for any sample and the corresponding sampling parameters used in the analysis. An inertial impactor can be used permanently with a system for different samples since the necessary slit width for



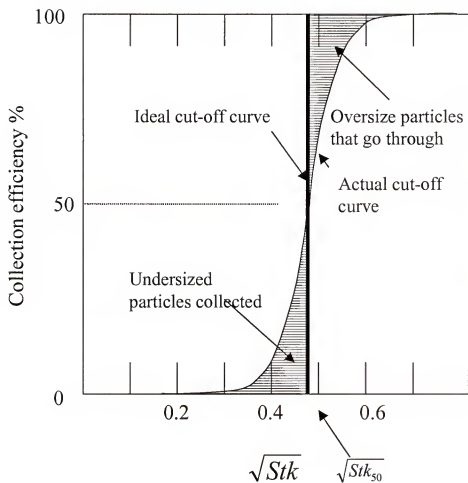


Figure 5-2. Ideal and actual cut-off curves for inertial impactors.

the impactor nozzle can be calculated based on the sample density and transport gas flow rates. Most, if not all, aerosol transport flow rates suitable to running the ICPMS can also be used with the impactor since the nozzle slit width can be changed accordingly.

### **Experimental Methods**

The inertial impactor used in this study was constructed by the University of Florida Chemistry Department Machine shop.<sup>41</sup> The entrance slit to the impactor was adjusted accordingly to satisfy the Stokes Equation and to achieve the desired cut-off diameter for a specific sample. Tygon tubing was used to connect the ablation chamber to the entrance nozzle of the impactor and to connect the exit nozzle of the impactor to the Aerosizer or to the ICPMS. Figure 5-3 shows the schematic diagram for the experimental set-up. Argon gas, at a flow rate of 0.365 l/min was used to transfer the ablated particles from the ablation chamber through the impactor and into the Aerosizer or to the ICPMS. The impactor was positioned about half way between the ablation cell and the plasma so the total distance traveled by the ablated particles was not significantly changed. Different cut-off diameters were used for each sample to select the cut-off diameter giving the best distribution without too much loss of material or without significant ICPMS signal reduction. The cut-off diameters chosen for this experiment were 5 and 3  $\mu\text{m}$ . The use of 4  $\mu\text{m}$  as the cut-off diameter was also investigated at the initial stages of the study but was abandoned since there were insignificant differences when using 3 and 5  $\mu\text{m}$ .

Table 5-1 summarizes the ICP and laser analytical operating parameters used in the ICPMS analyses.

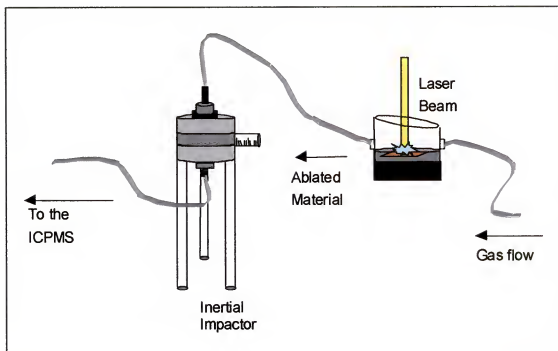


Figure 5-3. Experimental set-up for the use of an inertial impactor.

Table 5-1. Laser Ablation and ICPMS operating parameters used for experiments with inertial impactor.

**ICP Operating Parameters**

|                            |                    |
|----------------------------|--------------------|
| RF Power                   | 1200 W             |
| Coolant Gas Flow Rate      | 15 l/min           |
| Intermediate Gas Flow Rate | 1.5 l/min          |
| Nebulizer Gas Flow Rate    | 0.635 l/min        |
| Dwell Time                 | 2 ms, 32 ms, 64 ms |
| Channels per mass          | 8                  |

**Laser Ablating Parameters**

|                         |                      |
|-------------------------|----------------------|
| Transport Gas Flow Rate | 0.365 l/min          |
| Laser Irradiance        | 4 GW/cm <sup>2</sup> |
| Laser Repetition Rate   | 5 Hz                 |

The particle size distribution of the laser-ablated material was characterized with an Aerosizer (Aerosizer LD, Amherst Process Instrument, Massachusetts, USA). The Aerosizer is capable of measuring particles in the range of 0.2-700  $\mu\text{m}$ , and sampling rates up to 100,000 particles per second.

Nuclear waste simulants provided by the Pacific Northwest National Laboratory were ablated in this study. The waste simulants were in the form of sludge with  $\text{NaNO}_3$  as the matrix. For the experiments performed in this study, only waste simulant formula G was used. The simulant was spread on 5 layers of double sided-tape mounted on a glass slide, and dried in the oven for 5 hours at 110  $^{\circ}\text{C}$ . The tape used in this experiment was analyzed previously and determined to have low concentrations of Na, Al and Sb. The dried sample was directly ablated with the laser.

## **Results**

### **Effectiveness of the inertial impactor as a particle filter**

Initial stages of the investigation involved a thorough study of the effectiveness of the inertial impactor to filter out larger particles from the laser-ablated material. The impactor was used to filter out larger particles from the sample aerosol produced by ablation of the waste stimulant, aluminum and silica powder. Figures 5-4 to 5-6 show the particle size distribution (plotted as the number of particles and total mass ablated in each size range) of the laser-ablated material without the use of an inertial impactor and with the use of the inertial impactor with 3, 4 and 5  $\mu\text{m}$  as the cut-off diameter for the waste stimulant, aluminum powder and silica powder. For these experiments, an irradiance of 9  $\text{GW}/\text{cm}^2$  was used. The fraction of material, in terms of mass, passing through the impactor was measured by monitoring the total mass of the particles counted by the

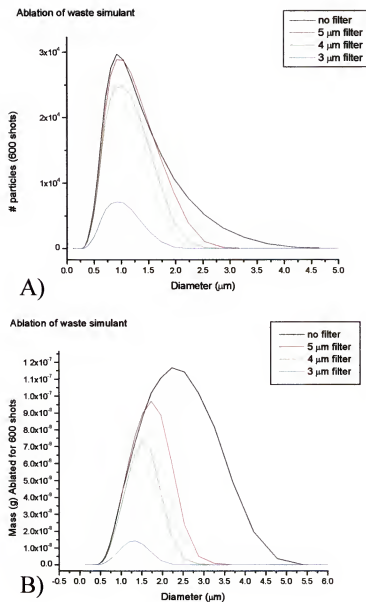


Figure 5-4. Particle size distribution of laser-ablated waste simulant with and without the use of inertial impactor. A) Number distribution B) Total mass ablated for 600 laser shots.

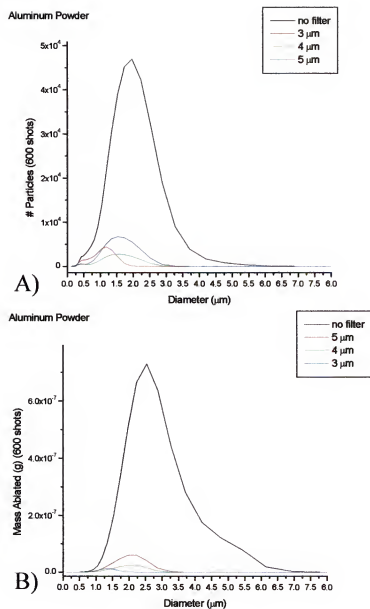


Figure 5-5. Particle size distribution of laser-ablated aluminum powder with and without the use of inertial impactor. A) Number distribution B) Total mass ablated for 600 laser shots.

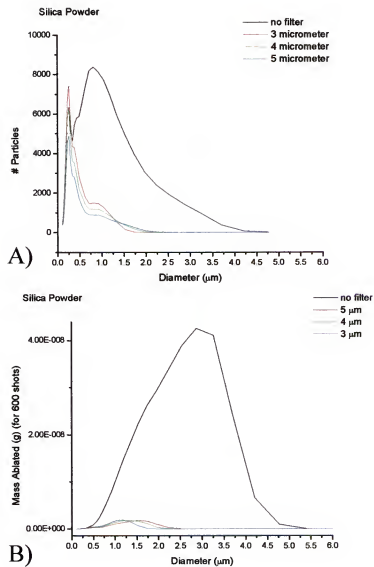


Figure 5-6. Particle size distribution of laser-ablated silica powder with and without the use of inertial impactor. A) Number distribution B) Total mass ablated for 600 laser shots.

Aerosizer and by comparing this to the mass actually ablated from the sample. For ablation of the waste stimulant, the 5, 4, and 3  $\mu\text{m}$  cut-off diameters with the inertial impactor resulted in the removal of 40%, 59% and 92%, respectively, of the total mass of the ablated material. For ablation of the aluminum powder, the 5, 4, and 3  $\mu\text{m}$  cut-off diameters resulted in the removal of 93%, 97% and 99%, respectively, of the total mass of the ablated material. For ablation of the silica powder, using the 5, 4, and 3  $\mu\text{m}$  cut-off diameters resulted in the removal of 96%, 97% and 99%, respectively, mass removal. The particle size distribution of the silica and aluminum powders tailed towards the larger diameters in the ablation conditions used in this experiment. Thus, removal of the larger particles removed most of the ablated material from the sample aerosol.

The ablated material from the waste stimulant was also collected on PTFE membrane filters (Polydisc TF, Whatman Inc., New Jersey, USA). This was done with and without the use of the inertial impactor. A field emission scanning electron microscope (S-4000, Hitachi High Technologies America, California, USA) was used to visually compare the size distribution of the material which passed through the impactor and the material which did not. Figure 5-7 shows that as expected, images of the filter paper showed a reduction in the large particles ranging from 3-5  $\mu\text{m}$  when the impactor was used.

### **Effect on Signal Intensity and Precision**

ICPMS analyses of the waste stimulant were performed with and without the use of the inertial impactor to determine its effect on ICPMS signal intensity and stability. The quadrupole was set to monitor the elements Al, Zr, Nd and Pb (chosen to represent



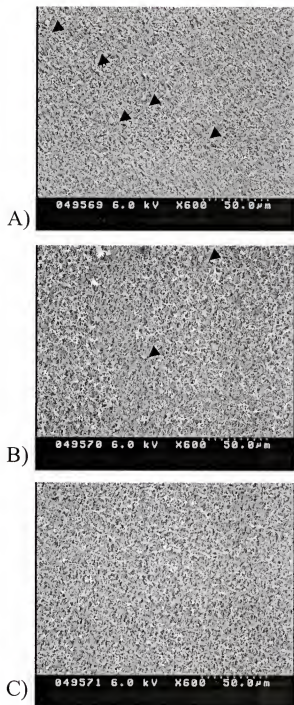


Figure 5-7. Scanning Electron microscope images of laser-ablated material. A) without going through inertial impactor. B) with the use of impactor at 5  $\mu\text{m}$  cut-off. C) with the use of impactor at 3  $\mu\text{m}$  cut-off.

different parts of the mass spectrum, and therefore different properties) one at a time. The concentrations of Al, Zr, Nd, and Pb in the waste simulant used were 1500 ppm, 1500 ppm, 6250 ppm and 400 ppm respectively. Actual analysis of the ablated material showed that using the impactor as a filter reduced the ICPMS signal intensity (in counts/s) to about 60% of the signal for unfiltered laser ablated material. The resulting signal however clearly had less variability. Figure 5-8 shows the resulting ICPMS signal stability of Al, Zr, Nd and Pb with respect to time for the ablated waste simulant without the use of an impactor, and with the use of the impactor at 5 and 3  $\mu\text{m}$  cut-off diameters. The low frequency (flicker) variation in the ICPMS signal was reduced with the use of the inertial impactor. This was further confirmed by taking the noise amplitude spectra of the signals with and without the use of an impactor, as shown in Figure 5-9. Without the use of an inertial impactor, the signal from laser ablation ICPMS measurement of the waste simulant showed excess low frequency noise. The use of the impactor both at 5 and 3  $\mu\text{m}$  cut-off diameter, significantly reduced the flicker. The signal variation of the resulting signals, reported as % relative standard deviation (%RSDs), also decreased significantly as shown in Table 5-2. The fact that the ICPMS signal intensity was reduced by 60% even when 92% of the total particles were removed confirmed that the larger particles were not ionized efficiently in the plasma and therefore did not significantly contribute to the signal. More importantly, it should be noted that such decrease in signal intensity was not detrimental to the analysis of the nuclear waste simulant. Thus, it was concluded that the consequence of significant sample aerosol mass reduction resulting from the removal of the larger particles was far outweighed by the

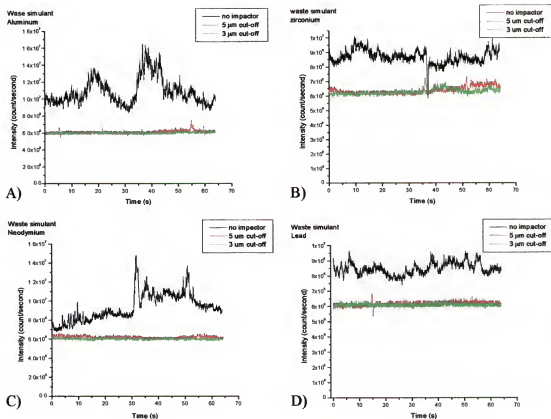


Figure 5-8. LA-ICPMS of laser-ablated waste simulant without the use of an impactor and with the use of an impactor. A) Aluminum signal. B) Zirconium signal. C) Neodymium signal. D) Lead signal.

Table 5-2. % RSD of LA-ICPMS analyses obtained with and without the use of an inertial impactor.

| % Relative Standard Deviation |             |      |      |
|-------------------------------|-------------|------|------|
|                               | No impactor | 5 μm | 3 μm |
| <sup>27</sup> Al              | 15          | 3.0  | 2.1  |
| <sup>238</sup> Pb             | 2.9         | 0.68 | 1.2  |
| <sup>146</sup> Nd             | 15          | 2.2  | 1.7  |
| <sup>90</sup> Zr              | 5.5         | 3.9  | 3.1  |

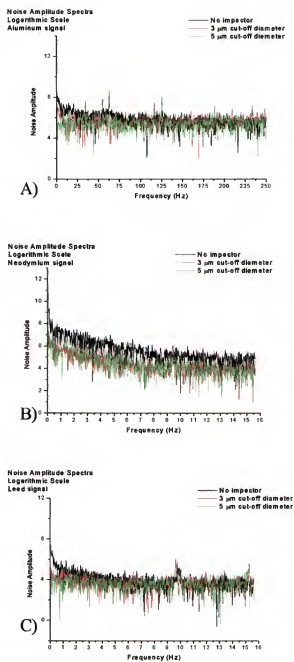


Figure 5-9. Noise Amplitude Spectra of LA-ICPMS signal for laser-ablated waste simulant without and with the use of the inertial impactor. A) Aluminum. B) Neodymium. C) Lead.

improvement of the signal stability. This was especially true for nuclear wastes where the elements of interest are present in bulk concentrations.

### **Effect on Fractionation**

To further evaluate the validity of the method, the effect of using an inertial impactor to filter out larger particles in laser-ablated material on isotopic and elemental fractionation was also investigated. Isotopic ( $^{146}/^{145}\text{Nd}$ ,  $^{146}/^{143}\text{Nd}$ ) and elemental ( $^{146}\text{Nd}/^{139}\text{La}$  and  $^{143}\text{Nd}/^{139}\text{La}$ ) ratios of Nd and La were calculated from laser ablation ICPMS analysis of the waste simulants with and without the use of the impactor. The data were acquired in the peak hopping mode at 64 ms dwell time. The acquired ratios were then compared with the expected ratios based on an independent analysis performed by the Pacific Northwest National Laboratory using ICPAES and solution ICPMS.

As shown by Figure 5-10, the isotopic and elemental ratios calculated from the analysis using the inertial impactor were always closer to the expected value. Specifically, the ratios calculated from the data obtained using the inertial impactor using 3  $\mu\text{m}$  cut-off diameter were closer to the expected value. These results confirmed the findings that smaller particles were ionized more efficiently in the plasma, resulting in fewer elemental and isotopic fractionation effects.

### **Conclusion**

It has been demonstrated that the inertial impactor could be used to filter out larger particles from laser ablated material to improve the particle size distribution for LA-ICPMS analysis. The inertial impactor was used with laser ablation of nuclear waste simulants. ICPMS signals for different elements were monitored and the resulting %RSD

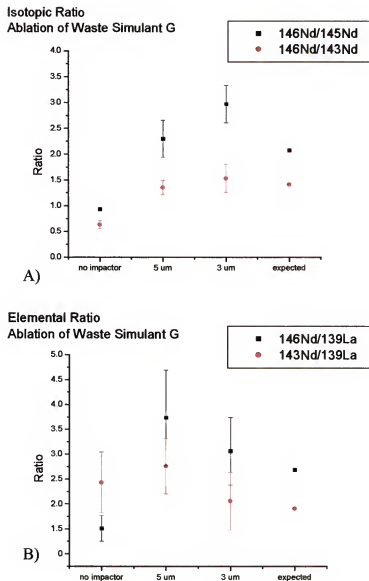


Figure 5-10. Effect of using an inertial impactor on elemental and isotopic fractionation.  
A) Elemental Ratio B) Isotopic Ratio.

simulants. ICPMS signals for different elements were monitored and the resulting %RSD was significantly improved when the inertial impactor with a 3  $\mu\text{m}$  cut-off diameter was used. Evaluation of isotopic and elemental ratios calculated from the laser ablation ICPMS analysis also showed that the use of an impactor reduced fractionation effects, both elemental and isotopic. Although removal of the larger particles resulted in a decrease in signal intensity, the increase in precision and decrease in ICP-induced fractionation outweighed this disadvantage. Another advantage of using the inertial impactor as a filter was that it was easy to implement into the LA-ICPMS system, since the slit width could simply be varied to change the cut-off diameter while maintaining the gas flow rate required to run the ICPMS.

## CHAPTER 6

### NORMALIZATION OF LA-ICPMS SIGNAL TO LIGHT SCATTERED BY LASER-ABLATED MATERIAL

The source of signal fluctuation in laser ablation can be attributed to either the existence of particle size distributions in the sample aerosol, non-linear changes in ablated mass due to shot-to-shot fluctuations of the laser energy, or both. The previous chapters have discussed improving the size distribution of laser-ablated material by either optimization of ablation parameters or by modification of the ablated material with the inertial impactor. Although these two methods have proved successful in removing unwanted fluctuations due to the quality of sample aerosol, they do not compensate for fluctuations in the mass of the ablated material introduced by shot-to-shot fluctuations of the laser pulse. In this chapter, a method of normalization is introduced to normalize the ICPMS signal to the variations in the quality as well as the quantity of the sample aerosol being introduced into the ICP. The light scattered by the sample aerosol traveling from the ablation chamber to the ICP was used for normalization.

#### **Background**

In this chapter, light scattered by the laser-ablated material was collected and used for normalization purposes to compensate for variations in the mass ablated (caused by non-linear changes in the ablation process which are in turn caused by random fluctuations in shot-to-shot pulses of the laser) and for variations in the size distribution of the laser-ablated material. A continuous wave (cw) laser beam was directed perpendicular to the flow of the sample aerosol and the light scattered by the aerosol



particles was collected. The use of light scatter as a normalization method has been explored by Nomizu and coworkers who used the collected scatter in the normalization of ICP-AES signal for the analysis of zirconium alloys<sup>43</sup>. Baker and coworkers also investigated the use of light scattering for normalization of ICPMS signal for analysis of soils<sup>44</sup>. It was reported that the precision obtained with normalization to scattered signal was not as good as that obtained with the use of an internal standard. Furthermore, there was also no investigation conducted as to how effective the method was in terms of determining differences in particle size distributions of sample aerosol and in mass ablated. No fundamental studies were performed to establish the validity and feasibility of the method. In this chapter, fundamental studies involving the effects of the particle size distribution and number density of the sample aerosol on the intensity of the light scattered were performed to evaluate the effectiveness of the method. Theoretical considerations as to how and in which cases the method can be effective were also made. Collection of light scattered by the sample aerosol was then optimized and normalization was applied to the actual analysis of nuclear waste simulants.

### **Principles of Particle Scatter**

Particles in the size range of 0.1 to 1000  $\mu\text{m}$ , are measured using the Mie theory in combination with Fraunhofer diffraction.<sup>45</sup>

As particle diameter increases from 1/10 to 10 times the wavelength of the incident light, scattering from different sides of a single particle is out of phase, causing interference and reducing intensity. Figure 6-1 shows the angular distribution of light scattered from a single particle, with the length of the arrows corresponding to the respective intensity of light in that direction. At small scattering angles, phase

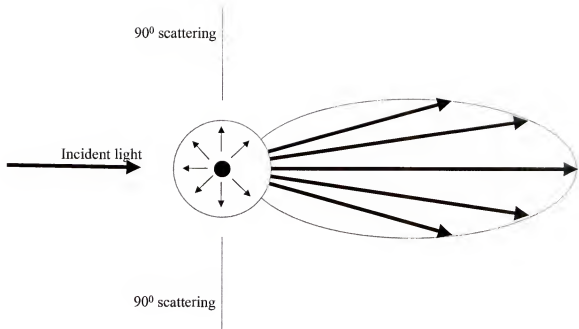


Figure 6-1. Angular distribution of light scattered by a particle (size range  $1/10$  to  $10$  times the wavelength of the incident light).

are small so that there is greater intensity of scattered light at low angles. This results into an angular distribution of scattered light (dependent on refractive index and particle size) in which most intense scatter occurs towards the forward direction. Thus, appropriate information regarding the particle size can be obtained when the light is collected in a plane intersecting the forward scattered light.

#### **Theoretical considerations to normalization of ICPMS signal with light scatter**

An idealistic approach to scattering is to consider the radiative power,  $P_{sc}$ , isotropically scattered by one single, spherical, non-absorbing particle generated from a given pure substance and illuminated by an unpolarized radiation. This is given by the simple expression below:

$$P_{sc} = P_{inc} \frac{\Omega_{sc}}{4\pi} Q_{sc} \quad (6-1)$$

$$Q_{sc} \equiv \frac{\sigma_{sc}}{A_p} = \frac{\sigma_{sc}}{\left(\frac{\pi D_p^2}{4}\right)} \quad (6-2)$$

$$P_{sc} = P_{inc} \frac{\Omega_{sc}}{4\pi} \frac{\sigma_{sc}}{A_p} \quad (6-3)$$

Here,  $P_{inc}$  is the power of the incident light (W),  $(\Omega_{sc}/4\pi)$  is the fractional solid angle of scattered light collection, and  $Q_{sc}$  is the efficiency of the scattering defined by the ratio of the scattering cross-section  $\sigma_{sc}$  (cm<sup>2</sup>) and the cross-sectional area of the particle  $A_p$  (cm<sup>2</sup>).

$N_p$  is the number of particles per unit volume uniformly distributed in the excitation volume and acting as independent scatterers, with all particles having the same diameter  $D_p$ .  $P_{sc}$  is given by:

$$P_{sc} = P_{inc} \frac{\Omega_{sc}}{4\pi} \frac{\sigma_{sc}}{A_p} N_p V_{sc} \quad (6-4)$$

where  $V_{sc}$  is the scattering volume. With the above assumption, one can see that if the incident power, the observed scattering volume, and the observation solid angle are constant, then power scattered depends linearly upon the number density of scatterers.

The measured scattered signal  $S_{sc}$  then is given by

$$S_{sc} = P_{sc} \cdot \eta_{d,sc} \quad (6-5)$$

where  $\eta_{d,sc}$  is the detection factor (e.g. counts/W).

The ICPMS signal for a given element M (here  $\chi_M=1$ , where  $\chi_M$  is the mole fraction of M in the particle) is given by

$$S_{icp} = N_{i,g} \cdot \eta_{inst} \cdot V_{i,s} \quad (6-6)$$

where  $V_{i,s}$  is the volume sampled by the instrument ( $\text{cm}^3$ ),  $N_{i,g}$  is the number of ions per  $\text{cm}^3$  of gas in the ICP, given by  $N_{i,g} = N_p \cdot \varepsilon_v \cdot \varepsilon_i$ , where  $\varepsilon_v$  and  $\varepsilon_i$  are the vaporization and ionization efficiencies respectively for a given particle diameter  $D_p$  and for every particle constituent, and  $f_e$  is the gas expansion factor in the plasma.

The signal for ICPMS can be derived by using a simplistic approach and by the following considerations:

The number of ions per  $\text{cm}^3$  of gas,  $N_{i,g}$  can be represented by

$$N_{i,g} = N_{a,g} \cdot \varepsilon_i \quad (6-7)$$

where  $N_{a,g}$  is the number of atoms per particle present in the gas phase and given by

$$N_{a,g} = \frac{m_p}{M_p} N_A \cdot \varepsilon_v \quad (6-8)$$

where  $N_A$  is Avogadro's number,  $m_p$  is the particle mass, and  $M_p$  is the atomic/molecular weight. The volume  $V_p$  and mass  $m_p$  of a particle are given by:

$$V_p = \frac{4}{3}\pi \frac{D_p^3}{8} = 0.52D_p^3 \quad (6-9)$$

$$m_p = \delta_p V_p = 0.52\delta_p D_p^3 \quad (6-10)$$

where  $\delta_p$  is the density of the particle ( $\text{g/cm}^3$ ). Note that, if  $\varepsilon_v \sim 1$ , the ICP signal increases with the third power of the particle diameter. The number of atoms or ions in one particle  $n_p$  is given by

$$n_p = \frac{\delta_p V_p N_A}{M_p} \quad (6-11)$$

Therefore,

$$n_p = \frac{m_p N_A}{M_p} = \frac{\delta_p V_p N_A}{M_p} = \frac{\delta_p 0.52 D_p^3 N_A}{M_p} \quad (6-12)$$

The number density (per  $\text{cm}^3$  of air) of atoms or ions due to all particles is then a product of  $n_p$  and  $N_p$ . The number of ions per  $\text{cm}^3$  of gas in the ICP is given by

$$N_{i,g} = N_p (\varepsilon_v \varepsilon_i f_c n_p) \quad (6-13)$$

Equation 6-13 is valid, assuming that no losses of particles occur between the scattering cell and the plasma. Strictly speaking, however, it would only be necessary that, even if losses occur, they are size-independent and that the loss factor ( $f_{\text{loss}}$ ) is the same for particles of different diameters.

The ratio of the scatter signal to the ICP signal can then be expressed as follows:

$$\frac{S_{sc}}{S_{ICP}} = \frac{\eta_{d,sc}}{\eta_{inst}} \frac{P_{inc} \frac{\Omega_{sc}}{4\pi} Q_{sc} V_{sc} N_p}{V_{i,s} N_p \varepsilon_v \varepsilon_i f_c n_p} \quad (6-14)$$

where

$$W_{sc} \equiv P_{inc} \frac{\Omega_{sc}}{4\pi} V_{sc} \quad (6-15)$$

and

$$Z_{ICP} \equiv V_{is} f_e n_p \quad (6-16)$$

Therefore,

$$\frac{S_{sc}}{S_{ICP}} = \frac{W_{sc} Q_{sc}}{Z_{ICP} \epsilon_v \epsilon_i} \quad (6-17)$$

Equation 6-17 holds for one single diameter isotropic scattering or with single event scattering. Equation 6-17 is the basis for the normalization of the ICP signal with the scattering signal. For particles of one single diameter, the ratio of the plasma signal and the scattering signal remains constant and independent of the fluctuations in the number density of the particles entering the scattering volume and the volume sampled to the plasma. Therefore, the measurement precision can be improved.

In reality, several of the assumptions made so far may not be completely valid. The following real functional dependencies of the various parameters need to be considered<sup>46,47</sup>:

$$(N_p)_{\text{plasma}} = (N_p)_{\text{ablated}} F_{\text{loss}}(D_p) \quad (6-18)$$

$$N_p = \int_0^\infty n(D_p) dD_p \quad (6-19)$$

$$Q_{sc} = f(D_p, \theta, \phi, \vec{E}_{inc}) \quad (6-20)$$

$$\epsilon_i, \epsilon_v = f(D_p, \text{chemical composition}) \quad (6-21)$$

$$K_{sc} \equiv Q_{sc} \cdot A_p \cdot N_p \quad (6-22)$$

$$K_{sc} \equiv Q_{sc} A_p N_p = \frac{\lambda_0^2}{4\pi^2} \int_0^\infty n(D_p) dD_p \int_0^{2\pi} \int_0^\pi F(\theta, \phi) \sin \theta d\theta d\phi \quad (6-23)$$

In the above equations,  $K_{sc}$  is the scattering coefficient ( $\text{cm}^{-1}$ ),  $\vec{E}_{inc}$  is the incident field ( $\text{V/cm}$ ), and  $F(\theta, \phi)$  is the dimensionless scattering function given by the absolute square of the (dimensionless) vector amplitude, which is a function of the scattering angle  $\theta$  and of the azimuthal scattering angle  $\phi$ <sup>46-48</sup>.

These relations are discussed more in detail below:

- (i) Equation 6-18 indicates that the number of particles ablated by the sampling laser (Nd:YAG) may exceed the maximum number density of particles in the scattering area and entering the plasma to ensure single scattering. More importantly, the number of particles in the scattering cell may exceed the maximum number necessary to insure single, rather than multiple scattering. A simple way to estimate this maximum number is to insure that the product of the extinction coefficient ( $\text{cm}^{-1}$ ) times the scattering length (i.e., the turbidity) must be less than unity. Considering an average scattering efficiency ( $Q_{sc}$ ) equal to 3 and an average particle diameter of  $1.5 \mu\text{m}$ , the maximum number density to insure single scattering is approximately  $10^7$  particles/ $\text{cm}^3$ .
- (ii) Equation 6-19 shows that a particle size distribution is indeed created by the ablation laser, i.e., there will be  $n(D_p)dD_p$  particles per unit volume in the size range  $D_p$  to  $D_p + dD_p$ . The ablation process will generate a unique particle size distribution function. In addition, each laser shot interacting with the sample may result in a different size distribution function.
- (iii) Equation 6-20 indicates that the scattering efficiency depends upon the diameter of the particle, the scattering angles (describing the angular dependence of the

amplitude of the scattering vector in spherical coordinates) and the polarization of the incident field.

The dependence outlined in Equation 6-20 is formulated analytically with the aid of the scattering theory for spherical particles.<sup>44-46</sup> Figure 6-1 presents some illustrative examples. An essential parameter is the so-called scattering parameter

$$x \equiv \frac{\pi D_p}{\lambda} \quad (6-24)$$

As seen in Figure 6-2, the extinction coefficients vary significantly with  $x$ . As the particle size increases, the efficiency rises very rapidly with increasing size, but then peaks at a given size and goes asymptotically to a constant value (plateau) with an oscillatory behavior. The overall behavior changes if the index of refraction of the particle changes and if the particle is also absorbing, in addition to scattering. This can be seen by the imaginary part of the index of refraction being different from zero.

If the ablation process produces particle diameters between 0 and 3  $\mu\text{m}$  (which is the case when the impactor is used), the scattering efficiency changes most significantly, since the scattering parameter,  $x$ , calculated for  $\lambda=0.514 \mu\text{m}$ , varies from 0 to 18 (see Figure 6-2).

- (iv) Equation 6-23 (reference 46) implies a size dependence of the overall efficiency of the plasma in vaporizing/exciting/ionizing particles of different diameters. As previously discussed, there is a maximum limit in the diameter of particle introduced into the plasma for complete vaporization and ionization of the particle during its residence time in the plasma. Such limit is about 3  $\mu\text{m}$ , depending upon operating conditions of the ICP.



- (v) Finally, it is important to note that the scatter signal will be influenced by the intensity distribution of the laser and the relative scattering position of the particle. A particle entering the observed scattered volume at an angle will not result in the same scatter intensity as a particle flying through the center of the laser beam.

In view of these considerations, Equation 17 has to be modified in real situations as follows:

$$\frac{S_{sc}}{S_{ICP}} = \frac{W_{sc}}{Z_{ICP}} \frac{Q_{sc}(m, x, F)}{\epsilon_{ICP}(D_p)} \quad (6-25)$$

In this case,  $Q_{sc}$  is a function of the (complex) index of refraction  $m$ , the scattering parameter  $x$ , and the scattering function  $F(\theta, \phi)$ . Moreover, the overall efficiency of the plasma in digesting the particles completely ( $\epsilon_{ICP} \equiv \epsilon_v \cdot \epsilon_i$ ) is now a function of  $D_p$ .

The criteria for which the normalization protocol based on ratioing the ICPMS signal to the scattering signal for a given number of ablation wastes can now be put on a more rigorous basis.

The size distribution per laser shot can be characterized by a mean particle diameter,  $\overline{D}_p$ , defined by the following expression<sup>47</sup>.

$$\overline{D}_p = \frac{\int_0^{\infty} D_p n(D_p) dD_p}{\int_0^{\infty} n(D_p) dD_p} \quad (6-26a)$$

or

$$\overline{D}_p = \frac{1}{N_p} \int_0^{\infty} D_p n(D_p) dD_p \quad (6-26b)$$

and by its associated variance

$$\sigma^2 = \frac{\int_0^{\infty} (D_p - \bar{D}_p)^2 n(D_p) dD_p}{\int_0^{\infty} n(D_p) dD_p} \quad (6-27)$$

or

$$\sigma^2 = \frac{1}{N_p} \int_0^{\infty} (D_p - \bar{D}_p)^2 n(D_p) dD_p \quad (6-28)$$

A value of zero for  $\sigma$  would obviously imply that every particle in the distribution has exactly the same diameter  $D_p$ . As the spread of the distribution around  $\bar{D}_p$  increases, the variance increases. Therefore, one can assume that each laser shot creates a mean particle diameter  $\bar{D}_p$  (defined by Equation. 6-26a), with a mean geometrical cross section  $((\pi \bar{D}_p^2)/4)$ , which will then scatter radiation with a mean scattering efficiency  $\bar{Q}_{sc}$ . We can now assume that the variance of the distribution, which is a characteristic parameter of each ablation event, does not vary significantly from one ablation event to another; the total mean ablated mass may vary (and will) vary, but the size distribution should remain constant. If this is the case and if the size range of the particle produced is well within the range of diameters digested by the plasma, the normalization procedure should indeed be capable of accounting for the fluctuation in the number of particles produced by the ablation process and characterized by their mean diameter  $\bar{D}_p$ . As a final experimental precaution, one should restrict the angle of observation of the scatter to a few degrees ( $\leq 10$ ) from  $\theta=0$ . For perpendicularly polarized incident light, this should minimize the differences in angular dependence of the scattering when the scattering parameter  $x$  varies from 0 to 20, which is the range of interest for the ablation

experiment. Figure 6-2 shows the dependence of the scattering parameter  $x$  on different parameters with regards to the collection of scattered light.

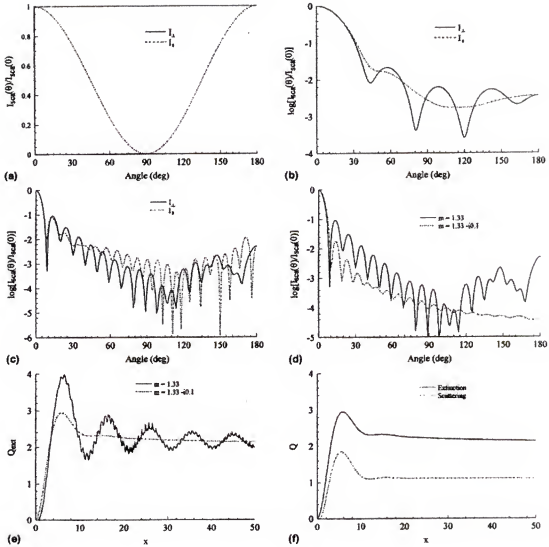


Figure 6-2. Scattering diagrams and efficiency factors: a) intensity versus angle for  $x=0.01$  and (index of refraction)  $m=1.33$ ; b) intensity versus angle for  $x=5$  and  $m=1.33$ ; c) intensity versus angle for  $x=20$  and  $m=1.33$ ; d) intensity versus angle for  $x=20$  and perpendicular polarization, showing the effect of absorption; e) extinction efficiency showing the effect of absorption; f) efficiency factors for absorbing particles.(modified figure from A.R. Jones, Progress in Energy and Combustion Science 25 (1999) 1-53).

### Experimental Methods

Figure 6-3 illustrates the schematic diagram for the experiments using the scatter cell. The scatter cell was placed halfway between the ablation chamber and the ICP torch. Ablated material was transported from the ablation cell through the scatter cell and into the ICPMS at 365 ml/min using the same tygon tubing normally used for transporting ablated material into the ICP. The argon-ion laser beam was focused into the cell by a fiber optic and lens so that it traversed the path of the aerosol flow in the scatter cell. The scattering cross-section was approximately 200  $\mu\text{m}$ . A lens and fiber optic collected the particle scatter at an angle of  $30^\circ$ , transferring it into a cooled photomultiplier tube (Hamamatsu, Photonics K.K., Japan). The signal was amplified by a low noise current amplifier (Model SR570, Stanford Research System Inc. Palo Alto, CA). The output was sent to a computer interface module (Stanford Research System Inc. Palo Alto, CA) recording the signal at a frequency equivalent to the dwell time being used to scan the quadrupole. Typical dwell times used in the experiments were 2, 32, and 64 ms so that the corresponding scatter signal was acquired at a frequency of 500, 31 and 15.6 Hz.

The scatter cell design used for this study is shown in Fig. 6-4. The cell was made of a solid aluminum block. Two holes perpendicular to each other, each with an inner diameter of 0.95 cm (the same diameter as the internal diameter of the transport tube), were drilled through each end of the block so that the two tunnels intersected at the center of the block. One hole (designated A in Fig. 6-4) served as the path of the sample aerosol flow and the other hole (designated as B in Fig. 6-4) served as the path of the laser beam. A third hole (designated as C in Fig. 6-4) was drilled at an angle of  $30^\circ$  from the path

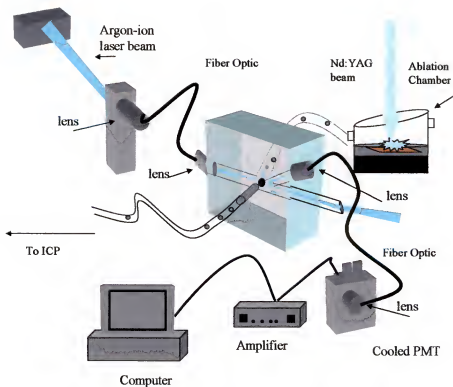


Figure 6-3. Schematic diagram of experimental set-up used for scatter normalization.

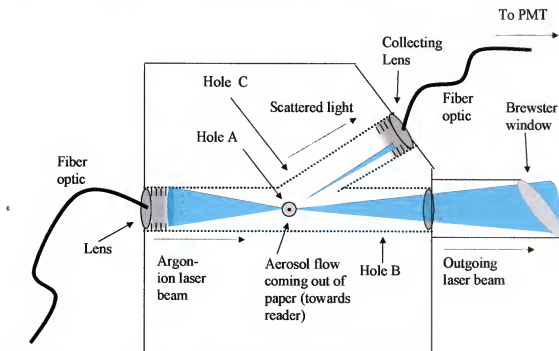


Figure 6-4. Design of the scatter cell used for scatter collection.

of the laser beam for collection of the scatter. Hole C was drilled from one side of the block and stopped at the center or middle of the scatter cell. Several other angles of scatter collection,  $90^\circ$ ,  $45^\circ$  and  $30^\circ$  from the plane of the laser beam, were investigated at the initial stages of the study. The optimum scatter signal in terms of signal-to-background and signal-to-noise ratios was achieved with the angle of collection at  $30^\circ$ . Figure 6-5 illustrates the design for the scatter cells using  $45^\circ$  and  $90^\circ$  angles. The interior of the cell was coated with an anti-reflecting black paint to prevent unnecessary laser light scattering and reflection. Aluminum tubes were press fit to the ends of the tunnels to allow connection with the ablation cell tubing and to provide an output path for the laser beam. A window placed at Brewster's angle was created on the tubing outlet of the laser beam to minimize further scattering and internal reflection. Figure 6-6 shows the scatter collected with and without the use of a Brewster's window.

A He-Ne (Aerotech, Inc., Pittsburgh, PA) laser with a 3 mW maximum power was initially used for this study. Because the intensity of the light scattered by particles is a function of the intensity of the incident beam, an argon-ion laser (Melles Griot, Carlsbad, CA) with a maximum of power of 750 mW was used for all measurements presented here. The wavelength range of the argon ion laser beam ranged from 457-514 nm. The laser beam was focused into a lens connected to a fiber optic, the other end of which was focused into the scatter cell.

An aerosol generation system designed by Hahn and coworkers<sup>49</sup> was used in this research to introduce mono-disperse particles into the scatter cell and into the ICPMS for investigation of the effect of particle size distribution and number density of a sample aerosol on the light scattered and on the corresponding ICPMS signal. The aerosol

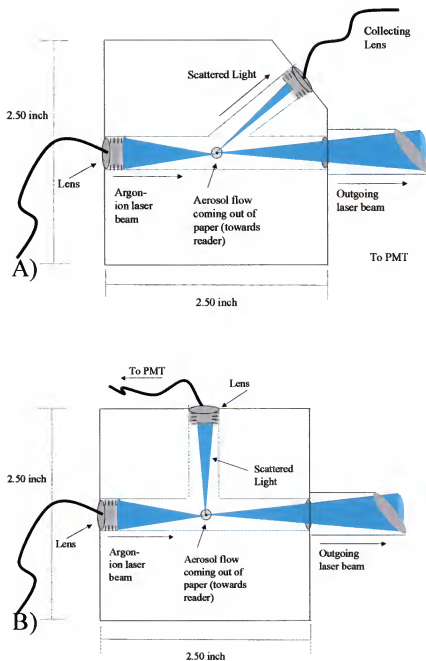


Figure 6-5. Other scatter cell designs considered for scatter collection. A) 45° angle of collection. B) 90° angle of collection.



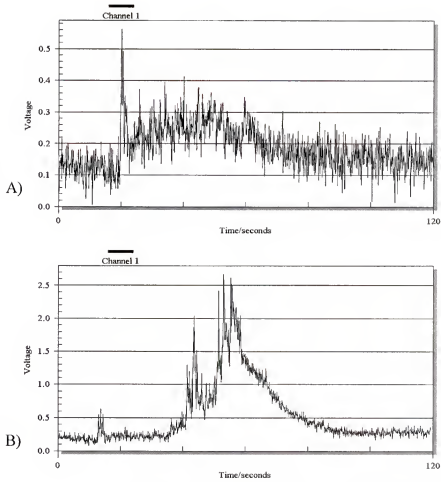


Figure 6-6. Scatter collected for laser ablation aluminum. A) without Brewster's window. B) with Brewster's window.

generation system was based on a standard pneumatic type medical nebulizer used in combination with a gaseous co-flow drying and mixing chamber. Figure 6-7 shows a schematic diagram of the nebulizer. The mixing chamber is a tube made of Plexiglas with an inner diameter of 6.3 cm and length of 43 cm. Argon gas is introduced into the nebulizer at 5 l/min and into the mixing chamber at 10 l/min. As sample droplets are nebulized and introduced into the mixing chamber, they are dried via evaporation. As the water evaporates from the nebulized droplets, particles comprised of the analyte species are formed as oxides. For this particular application, solutions of mono-disperse silica particles were introduced via the pneumatic nebulizer. The number density (# particles/ml) of the aerosol produced by the system can be calculated by multiplying the solution concentration (#particles/ml of solution) by the nebulization rate of the nebulizer (ml/min) and dividing by the total output gas flow of the generator system. For the conditions used in the experiment, the nebulization rate of the nebulizer was 0.72 ml/min, and the total gas flow was 15 l/min. For these experiments, the sample had to be introduced at a rate of 365 ml/min to simulate the ablation and transport conditions normally used in LA-ICPMS analyses so the output of the aerosol generation system was introduced into a flow meter to produce a flow of 365 ml/min. The rest of the sample aerosol was dumped.

Mono-disperse non-porous silica microspheres (Bangs Laboratories, Fishers, IN) with diameters 1.02, 1.87, 2.64 and 4.87  $\mu\text{m}$  were used for this study. The particles were suspended in water. Further dilutions with de-ionized water were conducted to obtain the desired number of particles per ml of solution.

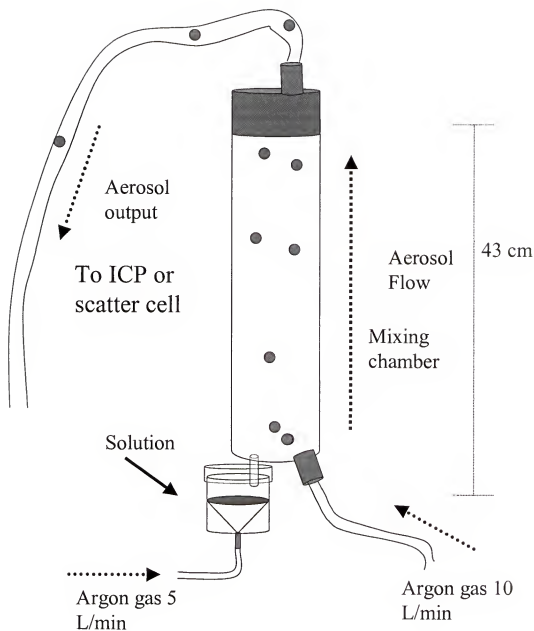


Figure 6-7. Schematic diagram of the nebulizer used to introduce mono-disperse Silica particles.

## Results

### Fundamental Studies

#### Light scatter as a function of particle diameter

Mono-disperse particles of diameters 1.02, 1.87, 2.64 and 4.87  $\mu\text{m}$  were introduced via the aerosol generation system. Solutions of the silica particles were prepared to yield 50 particles per second upon nebulization. Under the experimental conditions used, the laser beam or the scatter region was calculated to have a width of about 200  $\mu\text{m}$ , and the residence time of the particle in the scatter region was calculated approximately 600  $\mu\text{s}$ . Thus, the mean average number of particles in the scatter region was calculated to be 0.0293 particles per residence time under these experimental conditions. The Poisson distribution was used to calculate the probability of there being more than one particle in the laser region at a time. For this experiment, the solutions were made so that the probability of there being more than one particle at the scatter region was only 0.2%. Thus, scatter events recorded for these solutions were considered to be due to a single particle flowing through the scatter region. Figure 6-8 shows the scatter intensity as a function of particle diameter for single particles. The scatter intensity was taken as the average of scatter peaks for a 50 s time frame of measurements. Figure 6-9 shows the individual scatter signals recorded for single particles. It was observed that peak intensities of light scattered differed even for the same particle diameter. This can be explained by the fact that a particle flowing through the scatter region may pass through different areas of the scatter region, with different light intensities. For instance, a particle flowing through the middle of the focused beam will scatter more light than a particle flowing through the perimeter of the beam.

A similar experiment was conducted using solutions that resulted in sample aerosols with number densities of 50,000 particles per second. With these solutions, there were an average of 29 particles in the laser region at a time. Figure 6-10 shows examples of the light scatter recorded with the computer interface. Each event is considered to be caused by several particles or a group of particles passing through the laser beam. The intensity of the scatter peaks for a 10 second time frame were averaged and plotted with particle diameter. Figure 6-11 shows the scatter intensity for a concentrated sample aerosol as a function of particle diameter.

The particles generated were also introduced into the ICPMS to investigate the corresponding effect of the particle diameter on the ICPMS signal intensity and signal stability. Figure 6-12 shows the response of the ICPMS signal for the different particle diameters. The graph shows that the ICPMS signal increases with increasing diameter until  $4.87\text{ }\mu\text{m}$ , where the signal is similar to that for  $1.87\text{ }\mu\text{m}$ . The corresponding %RSD also increased drastically for particles with diameter  $4.87\text{ }\mu\text{m}$ . These results confirm that particles greater than a certain diameter are not ionized efficiently in the plasma and cause fluctuations in the ICPMS signal. The fact that the scatter signal for  $4.87\text{ }\mu\text{m}$  still increased and was higher than that for  $2.64\text{ }\mu\text{m}$  implied that the particles were being transported efficiently and the problem was primarily connected with the ionization in the plasma. This could be further confirmed if the scatter cell were placed closer to the plasma. However, with the present LA-ICPMS system, this was not feasible due to physical and mechanical constraints. A solution containing equal numbers of  $1.02$ ,  $1.87$  and  $2.64\text{ }\mu\text{m}$  particles was prepared to produce 50,000 particles per second upon nebulization. This solution was termed "mixed 3". Another solution containing equal

Scatter Intensity vs. Particle Diameter  
50 particles/second

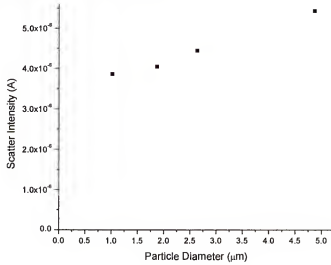


Figure 6-8. Light scatter intensity as a function of particle diameter for particles introduced at an average of 0.0293 particles per residence time in the scatter region.

Scatter Intensity for Si particles

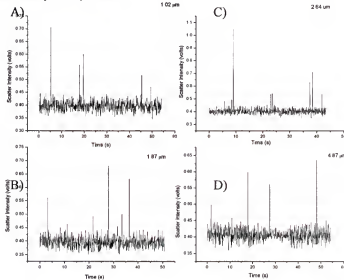


Figure 6-9. Light scattered by mono-disperse particles (average of 0.0293 particles per residence time in the scatter region). A) 1.02 μm. B) 1.87 μm. C) 2.64 μm and D) 4.87 μm.

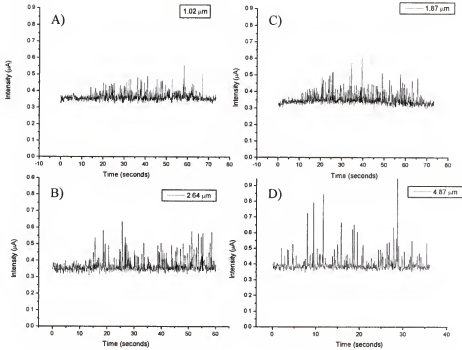


Figure 6-10. Light scattered by mono-disperse particles (average of 29.3 particles per residence time in the scatter region). A) 1.02  $\mu\text{m}$ . B) 1.87  $\mu\text{m}$ . C) 2.64  $\mu\text{m}$  and D) 4.87  $\mu\text{m}$

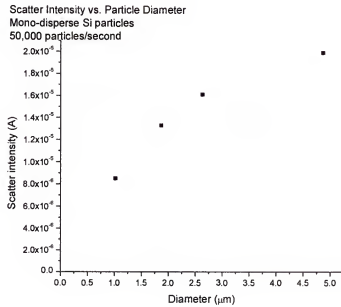


Figure 6-11. Light scatter intensity as a function of particle diameter for particles introduced at an average of 29.3 particles per residence time in the scatter region

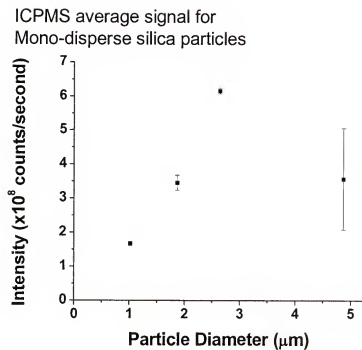


Figure 6-12. ICPMS signal intensity as a function of particle diameter for silica particles introduced at an average of 293 particles in the scatter region per residence time.



numbers of 1.02, 1.87, 2.64 and 4.87  $\mu\text{m}$  particles was prepared also to yield 50,000 particles per second upon nebulization. This solution was termed “mixed 4”. The two solutions were also nebulized via the aerosol generation system into the scatter cell and into the ICPMS. Figure 6-13a shows the ICPMS signal intensity for the two mixtures relative to the mono-disperse solutions. The ICPMS signal intensities of the two mixtures are lower than the mono-disperse solutions and have greater standard deviations. The ICPMS signal intensity of “mixed 4”, containing maximum diameter of 4.87  $\mu\text{m}$ , had a significantly lower signal than “mixed 3”, containing a maximum diameter of 2.64  $\mu\text{m}$ . Firstly, this data confirmed the fact that a wider distribution of sample aerosol reduces the ionization efficiency of the ICP. The two mixtures were prepared so that the number of particles introduced per second in the ICPMS was the same as that for the mono-disperse solutions. The equivalent mass introduced per second for the two mixtures was also similar to that introduced for the mono-disperse solution of 2.64  $\mu\text{m}$  particles. The ICPMS signal for the mixtures was significantly lower than that for 2.64  $\mu\text{m}$ . The standard deviation also increased significantly. Table 2-1 shows the average ICPMS signal for the different diameters and the mixtures. The ionization efficiency decreased as the particle size increased, and as the particle size distribution increased. Since the scatter signal recorded for the two mixtures (shown in Figure 6-13b) were significantly higher than that for the mono-disperse particles, it is implied that a wider distribution affects mainly the ionization efficiency more than the transport efficiency. Secondly, the ICPMS signal for “mixed 4” was lower than that for “mixed 3”. At the same time, the scatter recorded for the sample aerosol for “mixed 4” was considerably higher than that for “mixed 3”. Again, this reiterated that the presence of

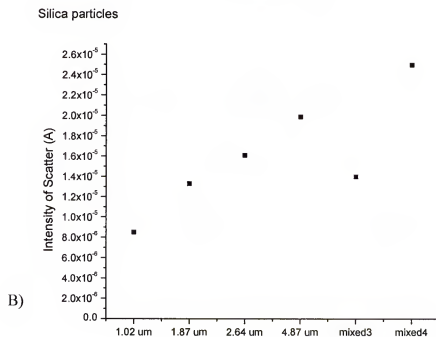
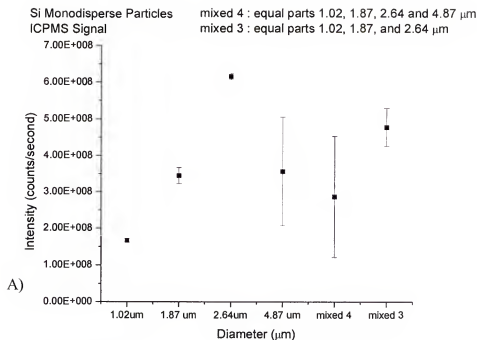


Figure 6-13. ICPMS signal and scatter intensity as a function of sample particle size distribution relative to the mono-disperse particles. A) ICPMS signal. B) Scatter signal.

large particles in a distribution affect the ICP signal stability. Table 6-1 shows the average ICPMS signal for the different diameters and the mixtures. The efficiency of ionization was calculated for each particle diameter by taking the ratio of the number of ions reaching the detector to the number of atoms being nebulized by the aerosol generator into the ICP. Figure 6-14 shows a plot of the ionization efficiency as a function of particle diameter.

### **Light scatter as a function of particle number density**

Silica particles with diameter  $1.87\ \mu\text{m}$  were nebulized at different concentrations and introduced through the scatter cell to determine the effect of number density on scatter intensity of the sample aerosol. Silica particles were introduced at 50, 500, 5,000, 50,000 and 500,000 particles/second resulting in an average of 0.0293, 0.293, 2.93, 29.3 and 293 particles at the scatter region at a time. Figure 6-15A shows the scatter intensity plotted versus the number of particles nebulized per second and Figure 6-15B shows the scatter intensity plotted versus the average number of particles in the laser region at a time for 2.93, 29.3 and 293 particles in the region. The results show that as the mean average number of particles in the region increased the scatter intensity also increased.

These fundamental studies confirmed that the scatter cell system designed was capable of measuring differences in the diameters of particles as well as differences in the number density of particles in the sample aerosol. Thus, it was capable of characterizing time-resolved differences in the quantity and the quality of the laser-ablated material.

Table 6-1. ICPMS average signal intensity and %RSD values for mono-disperse and poly-disperse silica particles.

|             | A V E (c o u n t s / s e c ) | % R S D |
|-------------|------------------------------|---------|
| 1 p p m S i | 1 . 2 E + 0 7                | 2 . 0   |
| 1 . 0 2 u m | 1 . 7 E + 0 8                | 3 . 6   |
| 1 . 8 7 u m | 3 . 5 E + 0 8                | 6 . 5   |
| 2 . 6 4 u m | 6 . 2 E + 0 8                | 1 . 4   |
| 4 . 8 7 u m | 3 . 6 E + 0 8                | 4 2     |
| m i x e d 4 | 2 . 9 E + 0 8                | 5 8     |
| m i x e d 3 | 4 . 8 E + 0 8                | 1 1     |

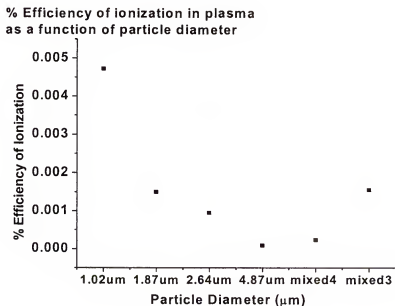


Figure 6-14. Ionization efficiency in the ICP as a function of particle diameter.

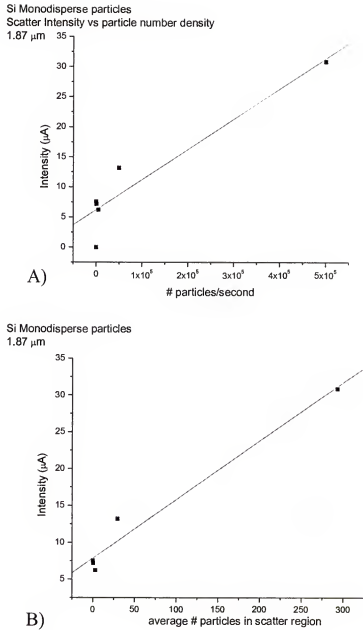


Figure 6-15. Light scattered by 1.87  $\mu\text{m}$  silica particles as a function on number density. A) Scatter intensity vs. number of particles introduced into cell/second. B) Scatter intensity vs average number o particles per residence time in the scatter region.

## Scatter of Ablated Material

The light scattered by the sample aerosol created upon ablation of different material was collected and optimized. The amplifier was set for a 6 dB lowpass filter, with a low noise gain of  $2\mu\text{A/V}$  and filter frequency of 1 MHz. At these settings, and with the use of the argon-ion laser at 700 mW, particles from a single particle could actually be observed. Figure 6-16 shows the light scattered by sample aerosol created with a single laser pulse at  $9\text{ GW/cm}^2$  on aluminum powder. The particles were released almost instantaneously and gradually disappeared over time with a few particles trailing after most of the laser ablated material had passed through the scatter region. Data on this graph was taken without cooling the PMT and a proper beam dump. Cooling the PMT helped reduce shot noise while the beam dump helped reduce unnecessary noise. Figure 6-17 shows the scatter for continuous ablation of the waste stimulant. Figure 6-18 shows the light scatter intensity for sample aerosol created with continuous ablation of aluminum powder.

The next step was to set-up the experiment so that as ablated material was being transported to the ICPMS for analysis, it passed through the scatter cell, during which time, scattered light was recorded for the time duration it took to scan the quadrupole. Since the sample aerosol passed the scatter cell before reaching the ICPMS, the two signals had to be synchronized prior to normalization. The particles scattered light approximately 5 seconds before ions reached the detector. To establish a correlation between the two signals, the quadrupole was kept scanning on one mass to monitor a particular ion signal. Figure 6-19 shows the scatter signal and the corresponding ICPMS signal for particles created by a single laser pulse on waste stimulant. The collection and

## Laser-ablated aluminum powder

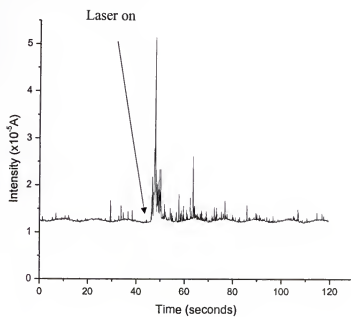


Figure 6-16. Light scattered by sample aerosol created with one laser shot on aluminum powder.

## Laser-ablated waste simulant

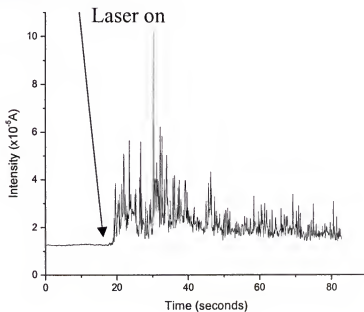


Figure 6-17. Light scattered by sample aerosol created by continuous ablation of waste simulant.

## Laser ablated aluminum powder

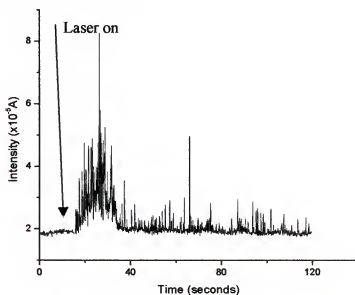


Figure 6-18. Light scattered by sample aerosol created from continuous ablation of aluminum powder.

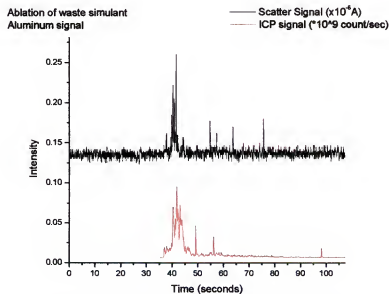


Figure 6-19. Synchronized scatter and ICPMS signal from sample aerosol created by a single laser pulse on waste simulant.



synchronization of the two signals was performed numerous times to verify that a correlation did exist between the two signals. Figure 6-20 shows other examples of ICPMS and scatter signals synchronized. Ablation of aluminum powder was also performed for simultaneous scatter and ICPMS signal collection. Figure 6-21 shows synchronized time-resolved signals for ICPMS and scatter signals for aluminum powder. A plot of ICPMS vs. scatter signal shows the evident correlation between the two signals as shown in Figure 6-22; the value for  $R^2$  was 0.7715.

### **Normalization**

To apply the actual normalization, the intensity of light scatter peaks were integrated over the time duration of the ICPMS measurements. The computer interface was triggered by an external pulse generator to 64 ms which was the dwell time used. ICPMS measurements were performed using 64 ms dwell time and based on the number of the analytes being looked at. The ICPMS signal intensity in counts per second for each run was divided by the integral of the scatter intensity ( $\mu A$ ) for the time duration of the analysis. Waste stimulant formula G was ablated and analyzed for yttrium (mass 89), zirconium (mass 90), lanthanum (mass 139) and neodymium (isotopes 143,145,146). Each run took approximately 20 seconds. Figure 6-23 shows graphs of the ICPMS signal intensities collected from the analysis of waste stimulant formula G, with and without normalization to the scatter signal. The %RSD values for the normalized and uncorrected signals are shown in Figure 6-24. The precision has been improved two fold as a result of the normalization. It is important to take note of the significant difference in behavior of the elements in the ICP. This can be attributed to mass bias in the ICPMS. It could also mean that elemental fractionation occurred either during ionization in the plasma (ICP-

induced fractionation) or that fractionation occurs upon ablation but is not corrected for by normalization. Light scattered by particles is not dependent on the elemental or isotopic composition of the particles.

The effectiveness of scatter normalization was further evaluated on the ablation of in-house standards for a calibration curve. For this experiment,  $\text{NaNO}_3$  was spiked with different concentrations of lead in the form of lead oxide. LA-ICPMS analysis was performed with and without the normalization. As shown in Figure 6-25, the uncorrected ICPMS signal did not even produce a linear calibration curve. This can be the case when the mass ablated during analysis of the three standards varied from one to the other and among runs of one standard. Normalization with the scatter signal resulted into a linear calibration curve as shown in Figure 6-25.

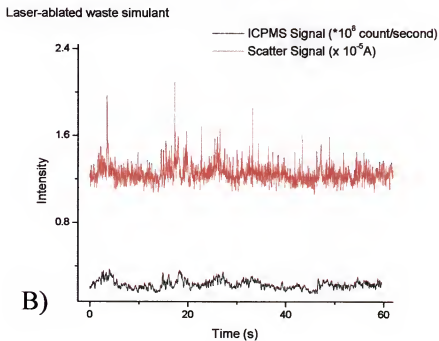
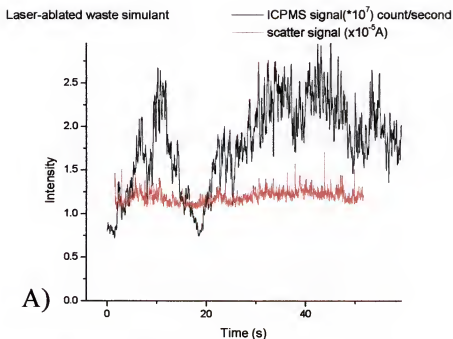


Figure 6-20. Synchronized ICPMS scatter signal for continuous ablation of waste simulant.

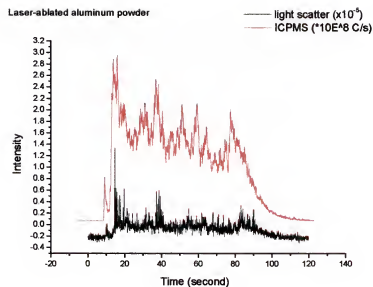


Figure 6-21. Synchronized ICPMS and scatter signals for sample aerosol created by ablation of aluminum powder.

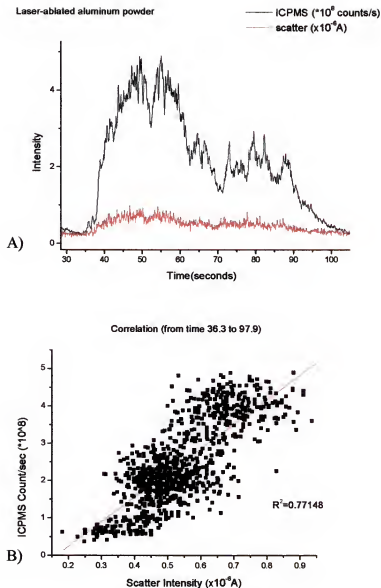
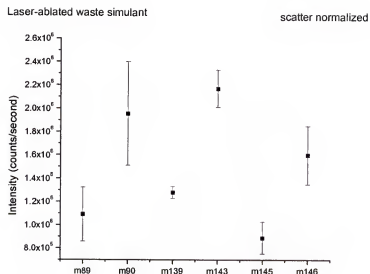
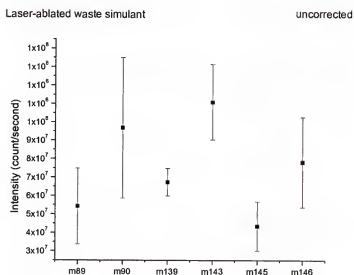


Figure 6-22. Correlation between the ICPMS and scatter signal for sample aerosol created with ablation of aluminum powder. A) Time-resolved ICPMS and scatter signal. B) ICPMS and scatter plotted against each other.



A)



B)

Figure 6-23. Normalized and uncorrected ICPMS signal intensities for ablation of waste simulants. A) Scatter-normalized ICPMS signals. B) Uncorrected ICPMS signals.

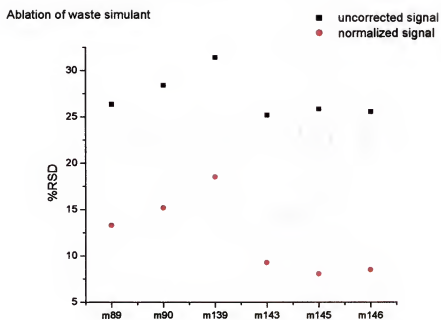


Figure 6-24. %RSD values for the normalized and uncorrected ICPMS signals resulting from LA-ICPMS analysis of waste stimulant.

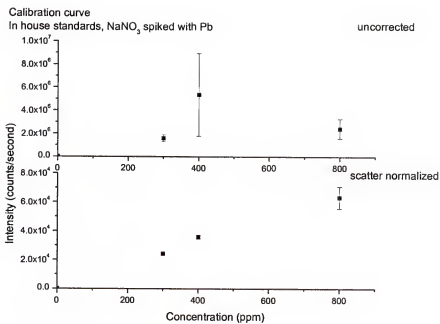


Figure 6-25. Uncorrected and scatter-normalized signal intensities for in house standards ( $\text{NaNO}_3$  spiked with Pb).



## Conclusion

The experiments discussed in this chapter revealed that the scatter cell developed is capable of measuring differences in the particle size distribution and in the number density of the aerosol. Monitoring the light scattered by the laser-ablated material as it is transported into the ICPMS for analysis yielded information about the mass and size distribution of the sample aerosol. Normalization of the ICPMS signal to the light scattered by the ablated material effectively reduced the %RSD two fold. Furthermore, normalization of the LA-ICPMS signals of standards used for calibration improved the linearity of the calibration curve. The scatter cell can also be used to study the mechanics of the laser-ablated material transport and ionization process.

The effectiveness of this method can be ascertained with some considerations derived from the theoretical approach to the normalization of the ICPMS signal with the scatter signal. First, the scattered light emitted by sample aerosols must be taken in the forward direction so that  $\theta$  is small, and with the use of a perpendicularly polarized incident light (such as the argon-ion laser used in this experiment), the differences in angular dependence of the scattering when the scattering parameter  $x$  varies from 0-20 (which is the range of interest for analysis of laser-ablated waste simulants) are minimized. Considering that realistically, a distribution in particle size exists in the ablated particles, the method will still be effective, granting that if a size distribution existed in the particle diameter, the mean particle diameter remained constant. Also granting that the ablated particle diameters produced are vaporized and ionized completely in the plasma, the normalization procedure should be valid in terms of accounting for differences in the number of particles ablated.

Advantages of using light scatter for normalization include the fact that it is based on a purely optical method so that no physical contact is made with the sample aerosol. As a result, it can be easily incorporated into laser ablation-ICPMS systems as an in-line method. Modern commercial particle size analyzers have been used for the same purpose but are not feasible for in-line particle monitoring since particles are basically destroyed after passing through commercial size analyzers<sup>3</sup>. The use of scatter cell is especially useful for the analysis of nuclear waste. Since no physical contact is necessary, exposure to radiation is avoided. Furthermore, the use of fiber optics to bring in the laser beam and to collect the scatter, gives the scatter cell flexibility in terms of mechanical and physical set-up. The use of fiber optics allows transmittal of the light source radiation or the light collection of over long distances. A disadvantage to the method, however, is that it is not capable of distinguishing differences in elemental or isotopic composition. The use of scatter for normalization effectively corrects for differences in the mass and in the particle size distribution of the laser-abated material.

## CHAPTER 7

### NORMALIZATION WITH SPECTRAL EMISSION INTENSITY FROM THE LASER INDUCED PLASMA

During laser ablation with irradiances of  $\text{GW}/\text{cm}^2$ , a plasma forms above the ablation site as a result of the explosion-like evaporation of the liquefied sample material expanding from the sample surface at a supersonic speed. The plasma, composed of electrons, ions, molecules and clusters of material, is of analytical purpose because the radiation it emits is spectrally resolved. The emitting species in the laser-induced plasma can be identified and quantified by their unique spectral wavelength and line intensities. In this chapter, the use of information collected from the spectral emission intensities of the laser-induced plasma created during ablation to normalize ICPMS signals will be discussed.

#### **Background**

Spectral atomic emission intensity from laser-induced plasmas has been shown to exhibit excellent correlation with atomic emission intensity in LA-ICP-AES<sup>48</sup>. Laser ablation sampling with an ICP for chemical analysis has a strong non-linear dependence on ablation parameters such as laser irradiance, energy, beam diameter, and crater depths. Laser-induced plasma emission also has been shown to exhibit a similar non-linear dependence on these ablation parameters. Russo and co-workers<sup>48</sup> have demonstrated that a direct correlation exists between inductively coupled plasma and laser induced plasma atomic spectral emission intensities. In this study, the use of the spectral emission intensities of analyte as a means of normalization of the analyte's corresponding ICPMS

signal was employed. A major advantage of using this method of normalization is that it makes use of information that is part of the laser ablation process itself. Thus, it entails no significant alteration of the LA-ICPMS set-up, but only the addition of an emission detector. Only optical access to the plasma is required so that the collection of information from the laser-induced plasma will not result into possibilities of sample contamination. The method can be used on-line to monitor time-resolved changes in ablation behavior. The method of normalization is perfect for heterogeneous material where matrix-matched standards are hardly ever available. Normalization to the emission intensities will reduce, if not eliminate, the need for matrix-matched standards since differences in ablation behavior can be compensated for. Unlike the use of an internal standard for normalization, there is no required knowledge of an element's composition in the sample. The chosen internal standard also requires that its behavior is similar to that of the analyte. The selection of the internal standard is particularly hard to find for heterogeneous samples especially for nuclear wastes. The method of normalization is also ideal for the analysis of nuclear wastes given that fiber optics and the lenses can be used to collect the spectra emission intensities and feed them into the spectrometer. The use of fiber optics allows access to the ablation cell and to the laser-induced plasma without the necessary exposure to radiation. Most importantly, since the radiation is spectrally resolved, normalization can be performed on a per-element basis. This will allow correcting for non-linear variations of each element. Thus, laser-induced elemental fractionation can also be monitored using this method.

### **Experimental Methods**

The set-up for the experiments performed in this chapter is illustrated schematically in Figure 7-1. The lens (Ocean Optics Inc., Florida USA) used to collect the spectral

emission was held in fixed at a location above the ablation cell so that even upon rastering during the ablation, the plasma was still collected at the same angle and distance. A fiber optic was used to transport the emission from the ablation spot and into the spectrometer (SD 2000 Ocean Optics, Inc.). The spectrometer had two input channels, master and slave. The master channel was used with spectral window from 230 nm to 300 nm. The slave channel was used from 180 nm to 870 nm. The emission intensities from the laser-induced plasma were monitored in synchronization with the ICPMS. The spectrometer was triggered with the flashlamp output of the Nd:YAG laser so that an average emission intensity was taken for every laser pulse during the ablation.

The same laser ablation and ICPMS systems used in the previous chapters were used for these experiments.

### **Results**

The initial stage of this study involved the demonstration of the correlation between the analyte emission intensity measured from the laser-induced plasma and the ICPMS signal of the same analyte. The demonstration of a correlation required a synchronization of the time duration and the data acquisition of both signals.

A copper metal was ablated with the Nd:YAG laser. The spectral emission intensity was then monitored while the particles or material resulting from the ablation was monitored in time with the ICPMS. Figure 7-2a shows the ICPMS signal and the

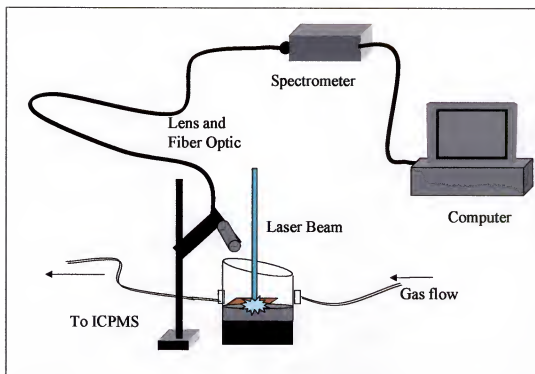


Figure 7-1. Schematic diagram of experimental set-up for simultaneous measurement of emission from the laser-induced plasma.

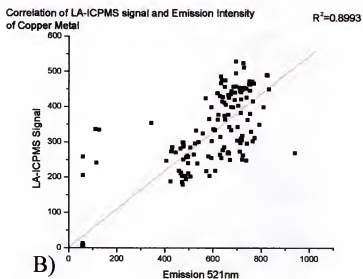
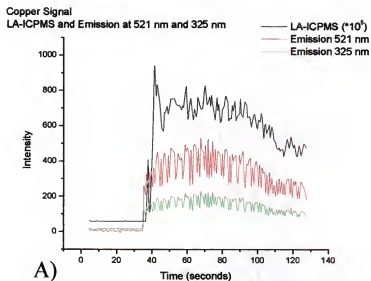


Figure 7-2. Synchronized ICPMS and emission intensity measured from the ablation of copper metal. A) Time-resolved ICPMS and emission intensities. B) Correlation of ICPMS and emission signal.

corresponding emission intensities of copper monitored at 325 nm. The two signals showed variations in mass ablated with time. The initial stage of ablation especially produced a greater mass than the rest of the ablation duration. The two signals, ICPMS and emission intensities, show a clear correlation to each other. Figure 7-2b shows the LA-ICPMS signal plotted against the Cu emission intensity. The resulting  $R^2$  value was 0.8993, demonstrating further the correlation between the two signals.

Figure 7-3 shows the raw ICPMS and emission signals plotted individually and the normalized LA-ICPMS signal. The low frequency variation in the normalized signal was reduced. High frequency fluctuations were present, but these may possibly be introduced by discrepancies in time synchronization.

The next stage was to show that the emission intensities measured from the laser-induced plasma reflected actual changes in mass ablated for particular elements. To demonstrate the dependence of the emission intensity on the mass ablated, a penny (1983 one cent coin) was ablated. The 1983-penny is made of a copper coated-zinc metal strip, which is an alloy of 97.5% zinc and 2.5% copper.

The penny was ablated without rastering the laser beam across the sample. This way, the laser pulses drilled through the copper coating of the penny and into the zinc-copper strip. Figure 7-4 shows the emission spectra collected from the ablation of the top layer of the penny (copper coating) and the spectra from the inner layer (zinc metal strip). The lines at 320.8 nm and 521.8 were monitored for copper and 636 nm for Zn were monitored simultaneously with two channels of the spectrometer. Although, there were other stronger emission lines seen, these three lines for copper and zinc were chosen specifically so that there were no possibilities of peak overlap from each analyte. The



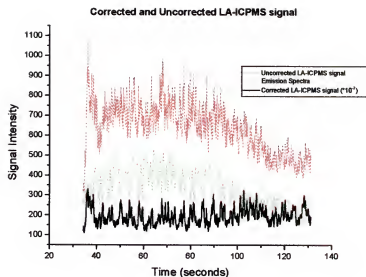


Figure 7-3. Raw LA-ICPMS signal and emission intensity plotted with the normalized LA-ICPMS signal.

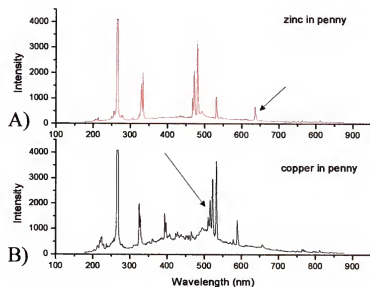


Figure 7-4. Emission spectra collected from ablation of A) zinc metal portion of penny, B) copper coating or top layer of penny.

emission intensities for copper and zinc are plotted in Figure 7-5A, showing that the copper layer was present for about 4 seconds (20 laser shots) until the zinc strip was reached. The ratio of Cu to Zn then became lower. After the first 4 seconds of ablation, the concentration of copper dropped abruptly and the concentration of zinc increased. Since the ICPMS used had a quadrupole for mass analyzer, the two elements could not be monitored at the same time. The quadrupole, however, was made to scan and peak hop between copper and zinc back and forth with dwell times of 32 ms. The quadrupole was then set to scan at specific times coinciding with data acquisition of the emission signals. Figure 7-5B shows the corresponding ICPMS intensities for copper and zinc at specific instances during the ablation. Figure 7-6A shows the actual Cu/Zn ratio measured from the ICPMS signals and Figure 7-6B show the corresponding emission intensities. As the laser drilled a hole into the penny, the ratio of Cu/Zn measured by the ICPMS decreased with time. This clearly agrees with the emission intensities measured for Cu and Zn.

Another experiment was carried out using the penny. The laser beam was first rastered across the penny. The laser was stopped at about 98 seconds, and immediately turned on but this time, firing at a fixed spot. The laser was then turned off. Figure 7-7 shows the corresponding ICPMS signal intensities (A) and emission intensities (B) for Cu and Zn. The ratio of the ICPMS signals for copper and zinc were taken and plotted against the copper and zinc emission intensities, shown in Figure 7-8. While the laser was being rastered, the ratio of Cu/Zn was above one, increasing with time. When the laser was turned on for the second time without rastering, a hole, the laser beam was drilling through the same spot. The corresponding emission signals show that copper was

decreasing while zinc was increasing. Thus, clearly, a correlation between the two signals with regards to differences in mass ablated exists.

The next stage of the investigation was to demonstrate that the technique could account for small variations in mass ablated due to non-linear dependence of ablation on laser pulse-to-pulse fluctuations and due to sample heterogeneity. The waste simulant formula G was then ablated and the emission signals from the laser-induced plasma and the ICPMS signals for Zr were monitored with time. Figure 7-9 shows the two signals plotted with time. The two signals showed a substantial correlation. The next step was to monitor Zr and Nd emission while monitoring the Zr and Nd ICPMS signals shown in Figure 7-10. The ratio of the ICPMS signals for Zr and Nd were plotted with the ratio of the emission intensities for Zr and Nd. Figure 7-11 shows the two ratios plotted together in time. Again, a direct correlation exists between the two ratios obtained from the two signals although the magnitude of the chosen emission lines do not correspond in terms of magnitude to that of the ICPMS. The waste simulant, being a complex sample, had too many emission lines that were overlapping each other. For the purposes of this investigation, the lines that were chosen were weak lines chosen for the reason that there were no spectral overlaps. Given the availability of a high resolution spectrometer or ccd camera, the appropriate emission lines could be chosen for the desired analytes so yielding the correct stoichiometric proportions.

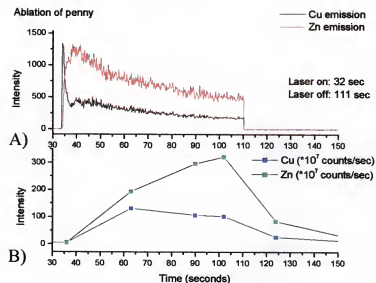


Figure 7-5. Simultaneous LA-ICMPS signals and emission intensities for Cu and Zn. A) Emission intensities of Cu and Zn plotted over time. B) ICPMS signals of Cu and Zn plotted over time.

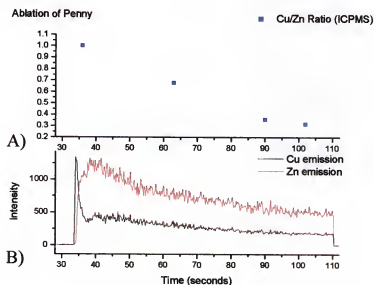


Figure 7-6. Simultaneous LA-ICMPS signals and emission intensities for Cu and Zn. A) Cu/Zn ratio values from LA-ICPMS signals. B) Emission intensities for Cu and Zn over time.

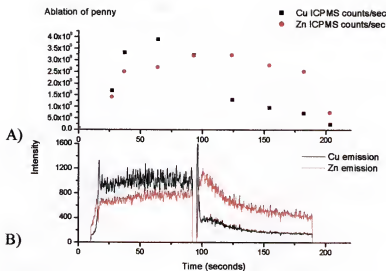


Figure 7-7. Resulting LA-ICPMS and emission signals for Cu and Zn for ablation of a penny. A) ICPMS signals for Cu and Zn. B) Emission intensities of Cu and Zn.

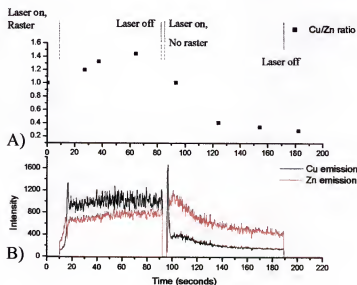


Figure 7-8. Resulting LA-ICPMS and emission signals for Cu and Zn for ablation of a penny. A) Cu/Zn ratio from ICPMS signal. B) Emission intensities for Cu and Zn.

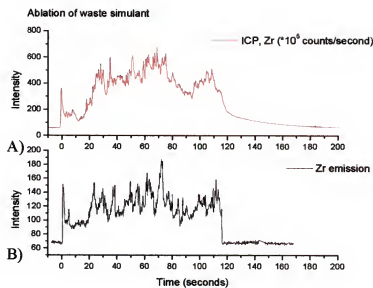


Figure 7-9. Synchronized LA-ICPMS and emission intensities for Zr as a result of waste simulant ablation. A) ICPMS signal. B) Emission signal.

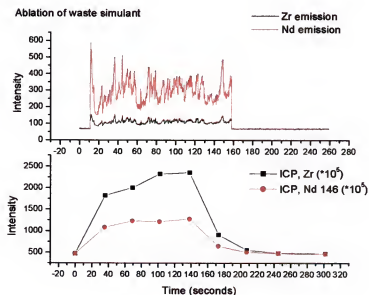


Figure 7-10. Synchronized signals for Zr and Nd for LA-ICPMS and emission intensities. A) Emission intensities from laser-induced plasma. B) ICPMS signal intensities.

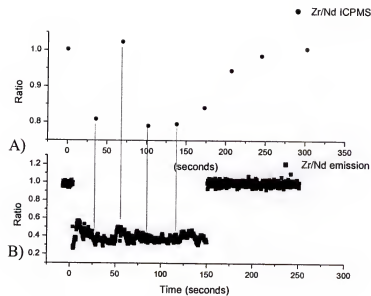


Figure 7-11. Zr/Nd ratios measured for LA-ICPMS and emission intensities for ablation of waste simulant. A) ICPMS ratio. B) Emission intensities ratio.

### Conclusion

A correlation between an analyte's ICPMS signal and spectral emission line intensity collected from the laser-induced plasma created upon ablation has been demonstrated. The emission intensity of an analyte could be monitored in time simultaneously with the collection of the ICPMS signal intensity. Because the emitted radiation of the laser-induced plasma and the mass ablated by the laser (therefore the ICPMS signal intensity, assuming that there were no losses due to transport of particles) were both dependent on ablation parameters such as laser irradiance, and beam diameter, the emission intensity could be used to normalize the ICPMS signal intensity.

The major advantage of this method is that each element of interest could be normalized to its own spectral emission intensity collected from the laser-induced plasma. It was possible to compensate for differences in ablation behavior of each element. Thus, unlike the use of internal standards or scatter-normalization, laser-induced fractionation could be investigated and accounted for by this method. This method of normalization however required the use of a high-resolution spectrometer capable of precise and efficient collection of emission lines.



## CHAPTER 8

### LA-ICPMS ANALYSIS OF WASTE SIMULANTS

The previous chapters have described a methodology of improving the accuracy of analyzing heterogeneous materials by optimizing the ablation parameters so that the particles created are of the smallest and narrowest distribution. Modification of particle size distribution of the ablated material was also performed by the use of an inertial impactor to filter out larger particles from the sample aerosol. To account for differences in mass and particle size distribution of laser-ablated material, a method of normalization was applied to improve the accuracy and precision of LA-ICPMS analysis of waste simulants. Results shown in this chapter will feature results from two different laser ablation-ICPMS systems, one at the University of Florida and other at Pacific Northwest National Laboratory.

#### **Experimental Methods**

The first part of this chapter involved the use of a Finnigan Mat Sola ICPMS (discussed in the previous chapters). The second part of the chapter involved experiments performed at Pacific Northwest National Laboratory (Richland, Wa) using a VG Plasma Quad from Fisons Instruments (Hastings, UK). The ICPMS was coupled to a Nd:YAG Continuum Surelite I Laser (Continuum Lasers, Santa Clara, Ca). The laser was operated to produce 7 ns pulses at 266 nm with pulse energies ranging from 0.400 mJ to 1 mJ and repetition rate of 5 Hz. The laser pulse energy was monitored on-line using a beam splitter and a pulse energy meter (Molelectron, Portland, Or). The sample was mounted on an x-y-z translation stage that could be adjusted to change the focus position of the

sample. The stage could also be moved so that the laser beam was rastered across the desired area of the sample. The ablated material was picked up by a tubing with 0.3175 cm internal diameter and transported to the ICP using argon gas at 1 l/min. The length of the tube from the ablation cell to the ICP was approximately 1.5 m. A particle size analyzer (Particle Measurement Systems, Boulder, Co) was used to monitor the particle size distribution of the laser-ablated material on-line. Since the particle size analyzer essentially destroyed particles, an isokinetic sampler was used to connect the transport tube to the particle size analyzer so that a fraction of the ablated material was delivered to the particle size analyzer while most were transported into the ICP. The particle size analyzer was capable of measuring the number of particles present in eight size classes from 0.1-2  $\mu\text{m}$  in diameter using laser light scattering.

A Leo 982Field Emission Scanning Electron Microscope (FESEM) (Leo Electron Microscopy Inc., NY, USA) was used to image laser-ablated particles collected on filter papers. The FESEM was equipped with an Oxford ISIS energy dispersive x-ray microanalysis system (Oxford Instruments, London, United Kingdom). The microanalysis system, with a SiLi detector, was capable of qualitative and quantitative elemental analyses and elemental mapping.

The waste simulants used in this study were the tank waste simulants described in Chapter 2.

## **Results**

### **Dry vs. Wet Ablation**

For this study, different concentrations of nitric acid were simultaneously nebulized as the waste simulants were being ablated. Prior studies performed using the Finnigan Mat Sola ICPMS revealed that nebulization of water or nitric acid simultaneously with

the ablation of soils resulted in a two-fold reduction in % RSD<sup>49</sup>. Thus, the effect of simultaneous solution-nebulization (wet ablation) of different concentrations of HNO<sub>3</sub> on precision and fractionation was investigated. Dry ablation or ablation without nebulization of any solution was also performed for the waste simulant. The quadrupole was set to monitor one mass so that fluctuations in signal could be monitored. Figure 8-1 shows the ICPMS signal intensities for Zirconium (mass 90) for the ablation of the waste simulant with and without the nebulization of HNO<sub>3</sub>. Figure 8-1a shows that the signal resulting from dry ablation (no solution nebulized with ablation) had greater fluctuations compared to signals resulting from wet ablation (simultaneous nebulization of solutions). Nebulization of water improved signal stability but nebulization of nitric acid solutions improved signal stability more significantly. As the concentration of the nitric acid was increased from 5% to 20%, the fluctuations in signal intensities also decreased. Figure 8-1b shows the average signal intensities (average of 2000 points) and the standard deviations from analyses with and without simultaneous nebulization. The effect of nebulizing different concentrations of nitric acid on fractionation was also studied. Figure 8-2 shows the calculated ratios for <sup>146</sup>Nd/<sup>145</sup>Nd (A), <sup>139</sup>La/<sup>90</sup>Zr (B), <sup>146</sup>Nd/<sup>139</sup>Nd (C), and <sup>143</sup>Nd/<sup>139</sup>La (D). The measured values shown in the graph are values that were obtained from the concentrations resulting from the independent analyses performed by Pacific Northwest National Laboratory. The ratios obtained while simultaneously nebulizing 20% nitric acid are generally the most accurate. The improvement of signal precision and accuracy when simultaneously nebulizing can be explained by the fact that the HNO<sub>3</sub> droplets released by the nebulizer come into contact with

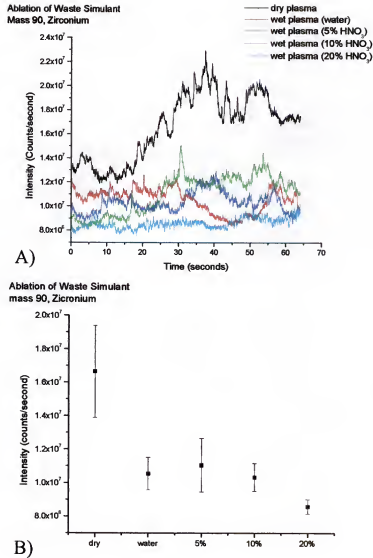


Figure 8-1. LA-ICPMS analysis of waste simulants with and without nebulization of nitric acid. (A) Time-resolved signals (B) Average signal intensities.

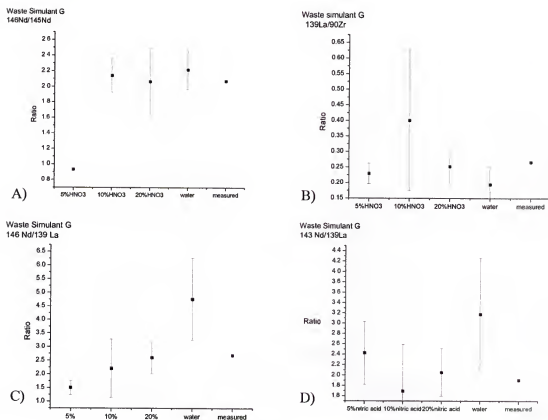


Figure 8-2. Effect of simultaneous nebulization of different nitric acid concentrations on fractionation. (A)  $^{146}\text{Nd}/^{145}\text{Nd}$  (B)  $^{139}\text{La}/^{90}\text{Zr}$  (C)  $^{146}\text{Nd}/^{139}\text{La}$ . (D)  $^{143}\text{Nd}/^{139}\text{La}$ .

the ablated material. Figure 8-3 illustrates the introduction of laser ablated material and sample aerosol from the nebulizer into the plasma torch. The ablated particles and the nitric acid droplets are introduced into the same tubing, 13 cm long, and are exposed to each other for approximately 5.6 s using the 0.635 l/min nebulizer gas for the nitric acid and 0.365 l/min for the transport of ablated material. During this 5.6 second time-duration, the  $\text{HNO}_3$  droplets collide with the ablated material. Upon collision of the waste particles and the nitric acid droplets, the laser ablated waste particles are broken up into smaller particles either due to the desolvating effect of nitric acid, or simply due to impact of collisions. This goes back to the theory that smaller particles are ionized more efficiently in the plasma. Thus, it is possible that by using a higher concentration of nitric acid, the solid particles are dissolved to a greater extent compared to using 5% nitric acid.

#### **LA-ICPMS Analysis of Waste Simulant**

Three different formulations of the waste simulants were measured for La, Nd, Zr, and Y. The simulants had the 400, 1500 and 6250 ppm of Nd, 50,100, and 400 ppm of La, 100, 400 and 1500 ppm of Zr, and 25, 100, and 400 ppm of Y. Thus, the three simulant formulations were used to study the linearity of the ICPMS signals for these concentrations. As the consistencies and physical properties of the waste simulants differed drastically, it was almost impossible to obtain a linear calibration from LA-ICPMS analysis. The mass ablated per sample per measurement would drastically vary. When the light scattered by the ablated particles was monitored and used to normalize the resulting ICPMS signals, the linearity of the calibration curve improved. Figures 8-4 to 8-6 show the uncorrected and scatter-normalized ICPMS signals obtained from the analysis of the waste simulants. The linearity of the calibration curve was improved as

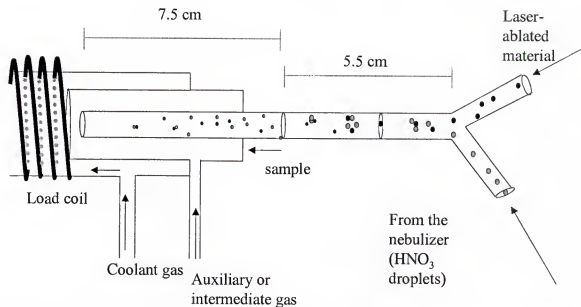


Figure 8-3. Schematic diagram of the introduction of laser-ablated material and nebulized HNO<sub>3</sub> droplets in the ICP torch.

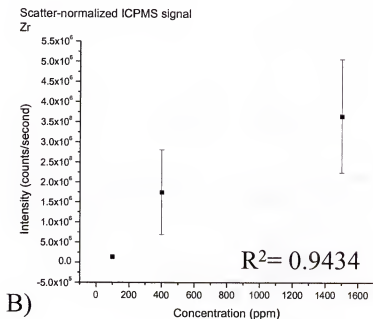
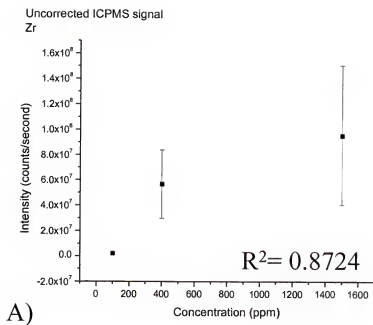
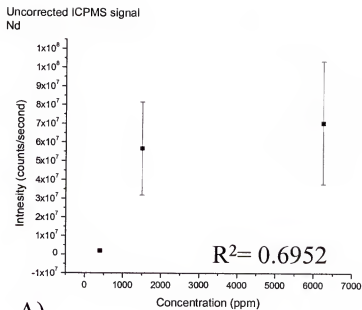
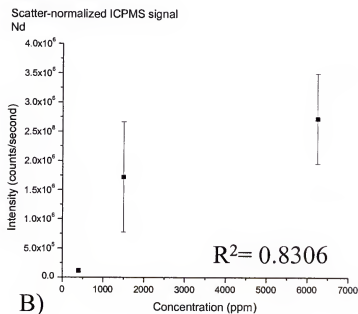


Figure 8-4. LA-ICPMS analysis of waste simulants for Zr. A) Uncorrected ICPMS signal intensities B) Scatter-normalized ICPMS signal intensities.





A)



B)

Figure 8-5. LA-ICPMS analysis of waste simulants for Nd. A) Uncorrected ICPMS signal intensities B) Scatter-normalized ICPMS signal intensities.

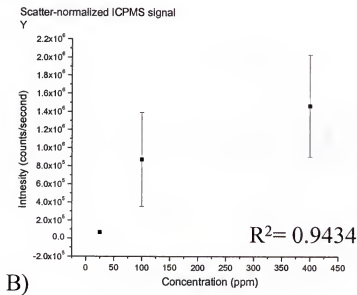
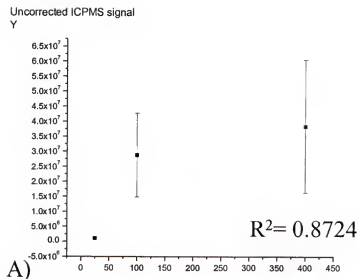


Figure 8-6. LA-ICPMS analysis of waste simulants for Y. A) Uncorrected ICPMS signal intensities B) Scatter-normalized ICPMS signal intensities.

demonstrated by the increase in the  $R^2$  values. However, the improvement in the signal precision was not significant.

An inertial impactor was then placed between the ablation cell so that larger particles were filtered out of the aerosol before passing through the scatter cell and correspondingly before entering into the ICP. Figure 8-7 shows the schematic diagram for this set-up. When the impactor alone was used, the precision for the measurement of each waste simulant for Nd, Y, La and Zr was improved at least 2-fold. However, the linearities of the ICPMS signals for the three different concentrations of the different elements were not improved at all. In fact, when using the impactor, the linearity of the curve became worse.

However, when the impactor was used in combination with the scatter cell, the improvement was more significant than when the impactor or the scatter cell were used separately. Figures 8-8 to 8-10 show the calibration curve resulting from the use of the impactor alone and that from the combination of the impactor and scatter-normalization for Nd, Zr and Y, respectively. Table 8-1 shows the % RSD values obtained from analysis of waste simulants without any correction or normalization, with the use of an inertial impactor alone and with the use of both impactor and scatter normalization. % RSD values obtained without any method of correction ranged from 18%-58%. At this point, it is important to note that ICPMS measurements of the three different simulants produce results with drastically different %RSD values, especially the one with the lowest concentrations. This was attributed to differences in ablation behavior of each simulant.

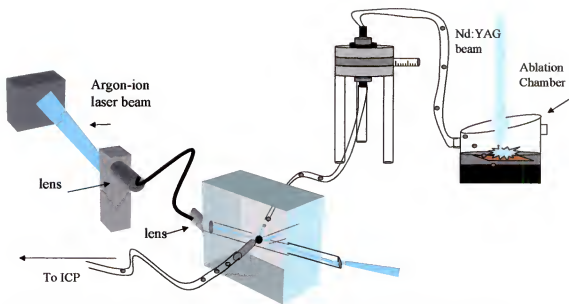


Figure 8-7. Schematic diagram of experiments using both impactor and scatter-normalization.

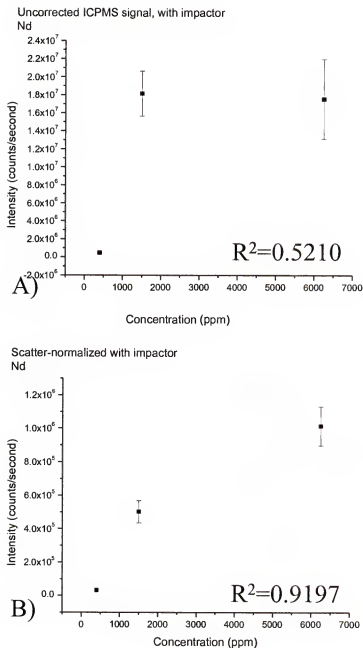


Figure 8-8. LA-ICPMS analysis of waste simulants for Nd. A) With the use of an inertial impactor. B) With the use of an inertial impactor and scatter-normalization.

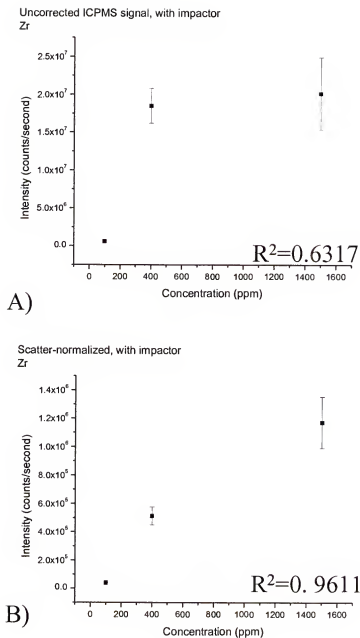


Figure 8-9. LA-ICPMS analysis of waste simulants for Zr. A) With the use of an inertial impactor. B) With the use of an inertial impactor and scatter-normalization.

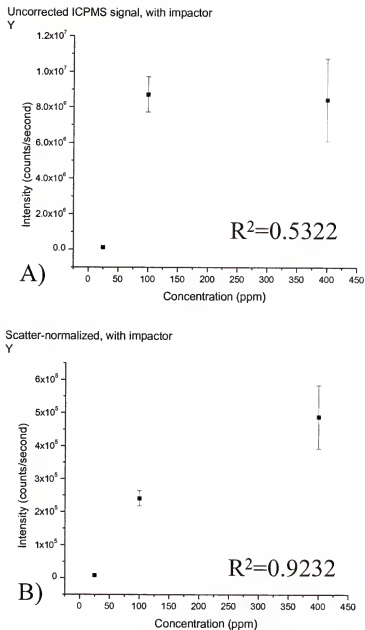


Figure 8-10. LA-ICPMS analysis of waste simulants for Y. A) With the use of an inertial impactor. B) With the use of an inertial impactor and scatter-normalization.

Table 8-1. Results of LA-ICPMS analysis of waste simulants with and without any correction methods.

| % Relative Standard Deviation |                  |               |                    |
|-------------------------------|------------------|---------------|--------------------|
| Concentration (ppm)           | Uncorrected data | Impactor only | Scatter + impactor |
| <sup>146</sup> Nd             |                  |               |                    |
| 400                           | 22               | 13            | 3.0                |
| 1500                          | 44               | 14            | 13                 |
| 6250                          | 47               | 25            | 5.2                |
| <sup>139</sup> La             |                  |               |                    |
| 100                           | 46               | 16            | 12                 |
| 400                           | 55               | 36            | 7.6                |
| 100                           | 18               | 19            | 4.2                |
| <sup>90</sup> Zr              |                  |               |                    |
| 400                           | 47               | 12            | 12                 |
| 1500                          | 58               | 24            | 13                 |
| <sup>89</sup> Y               |                  |               |                    |
| 25                            | 29               | 36            | 27                 |
| 100                           | 49               | 11            | 9.5                |
| 400                           | 58               | 28            | 14                 |



Compared to the results obtained without any correction methods applied, the % RSD values were improved approximately by a factor of two when an inertial impactor was used to filter out larger particles. However, the signal also decreased significantly so that with the use of the impactor, 50 ppm La could no longer be detected. For the rest of the elements, the signal intensity decreased by a factor of 4-5 times. Results obtained when scatter-cell normalization is used in combination with the inertial impactor showed a more significant improvement in %RSD. The improvement in precision for the different standards for different concentrations of Nd, La, Y and Zr ranged from 4-fold to as much as 10-fold, that is with the exception of 25 ppm of La. Furthermore, the calibration curves obtained using both impactor and scatter showed fair correlation.

#### **Studies Performed with the PNNL System**

Figure 8-11 shows the schematic diagram of the experimental set-up used for this set of experiments. The particle size distribution of a fraction of the ablated material was monitored during the ICPMS analysis performed.

#### **Effect of varying laser irradiance**

The effect of increasing the laser energy and consequently increasing the laser irradiance on the particle size distribution of the ablated material and the ICPMS signal intensity and stability was investigated.

All things being equal, ablation of the waste simulant with 1 mJ ( $5.7 \text{ GW/cm}^2$ ) yielded slightly wider size distributions than that yielded by ablation with 0.600 mJ ( $3.4 \text{ GW/cm}^2$ ), shown in Figure 8-12A. The %RSD obtained from the analysis of the material created with 0.600 mJ laser pulses was significantly better than that

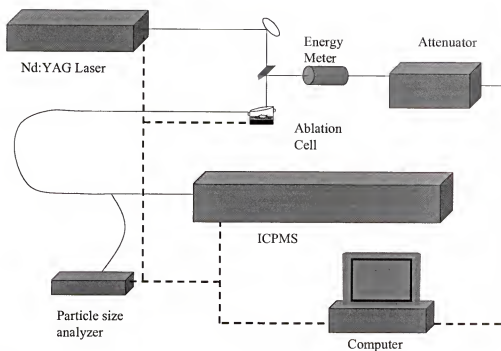


Figure 8-11. Schematic Diagram of the Laser Ablation ICPMS system at Pacific Northwest National Laboratory.

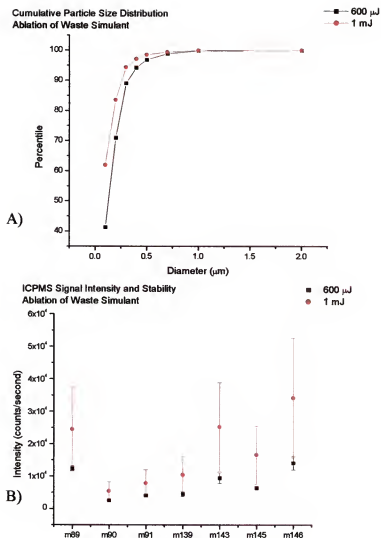


Figure 8-12. LA-ICPMS analysis of waste simulants using 0.600 mJ and 1 mJ laser energies. A) Cumulative particle size distribution of ablated material. B) ICPMS signal intensities.

obtained using 1 mJ laser pulses (shown in Figure 8-12B). The %RSD values for ablation with 0.600 mJ ranged from 7-17% while that obtained from using 1 mJ ranged from 52-54%. Unfortunately, using 0.600 mJ resulted in less material ablated. The signal intensity obtained for ablation with 0.600 mJ was approximately half of that obtained with 1 mJ. For analysis of waste simulants with lower concentrations of analytes, detection or sensitivity may be compromised by the use of lower laser energies. For instance, in the case of the system used in University of Florida, ablation using less than 1 mJ did not produce enough ablated material for detection of most analytes. Table 8-2 shows the results from LA-ICPMS analyses using 1 mJ and 0.600 mJ. The effect of the laser energy on fractionation (isotopic and elemental) was also studied. Table 8-3 shows the calculated ratios. The difference in laser irradiance does not affect the isotopic fractionation significantly. The elemental fractionation is more affected. This is as expected since different elements behave differently upon laser ablation. The particles produced from ablation of waste simulants with 1 mJ and 0.600 mJ were collected on nucleopore filters using a pump, and imaged with a field emission scanning electron microscope (982 Leo, company). Figures 8-13 and 8-14 show the particles created from ablation with 0.600 mJ and 1 mJ laser energies respectively. The presence of particles as large as 20  $\mu\text{m}$  in diameter was noted with the material created from 1 mJ laser pulse energy. The biggest particles formed in the material created with 0.600 mJ laser energy had a diameters less than 5  $\mu\text{m}$ . This piece of information is important since the particle size analyzer used in these experiments is incapable of giving distributions above 2  $\mu\text{m}$ .

Table 8-2. Results of LA-ICPMS analysis of waste simulants using 0.600 mJ and 1 mJ laser energies for ablation

| % Relative Standard Deviation |        |      |
|-------------------------------|--------|------|
| Element mass                  | 600 uJ | 1 mJ |
| 89                            | 6.8    | 52   |
| 90                            | 9.4    | 53   |
| 91                            | 6.7    | 52   |
| 139                           | 16     | 54   |
| 143                           | 17     | 54   |
| 145                           | 9.2    | 54   |
| 146                           | 15     | 54   |

Table 8-3. Elemental and isotopic ratios obtained from the analysis of waste simulants.

|         | 600 uJ |       | 1mJ  |       |          |
|---------|--------|-------|------|-------|----------|
|         | AVE    | % RSD | AVE  | % RSD | Expected |
| 146/145 | 2.20   | 11.48 | 2.07 | 2.04  | 2.07     |
| 146/143 | 1.49   | 7.84  | 1.35 | 3.89  | 1.41     |
| 143/139 | 2.10   | 6.74  | 2.65 | 19.59 | 1.91     |

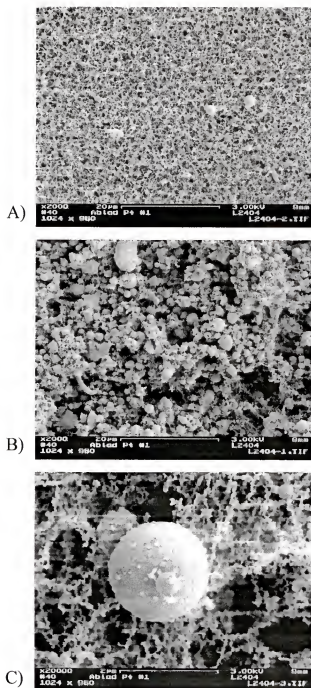


Figure 8-13. Scanning electron microscope images of particles resulting from ablation of waste simulants using 0.600 mJ laser energy. A) A few 2 μm-diameter particles B) A cluster of particles of different sizes C) A particle 2 μm in diameter with smaller particles on it.

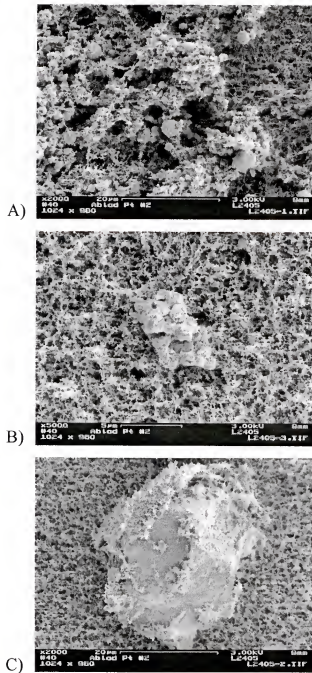


Figure 8-14. Scanning electron microscope images of particles resulting from ablation of waste simulants using 1 mJ laser energy. A) A cluster of particles of different sized B) A solid chunk of material C) A close up of a 20 µm-diameter particle.

**Raster vs. no raster**

Another method of sample preparation used at PNNL was the use of small Teflon cups with diameters about 0.6 cm and depth of about 1.2 cm. The method of sampling used was to fire the laser at a fixed position. Experiments were performed to determine the effect rastering the beam across the sample. As illustrated in Figure 8-15, rastering the laser beam across the sample surface resulted in better signal precision than when the laser was fired at a fixed position. Table 8-4 shows that when the laser was not rastered, the %RSD value was increased by a factor of two. This may be explained by the fact that when the laser is fired in one spot of the cup, a wider particle size distribution and a variance in the distribution resulted per shot since the laser focus was changed as the laser drills a hole into the sample surface.

**Impactor studies**

The use of the impactor was employed in the analysis of waste simulant G on a slide using 1 mJ laser energy. Figure 8-16 shows the results for the analyses using cut-off diameters 2, 1 and 0.5  $\mu\text{m}$ . The particle size analyzer used was only capable of detecting particles of diameters 2  $\mu\text{m}$  and below so these diameters were chosen. The particle size distribution of the ablated material also proved to be smaller than that achieved with the LA-ICPMS system used at the University of Florida. Table 8-5 shows that the use of the impactor evidently improved the % RSD values when cut-off diameters 2 and 1  $\mu\text{m}$  were used. When a 0.5 cut-off diameter was used, the % RSD values did not improve. This resulted because too much mass was removed by filtering out particles greater than 0.5  $\mu\text{m}$  in diameter. Figure 8-16 illustrates use of the impactor improved the precision for the analysis of almost all the analytes in the waste simulants.



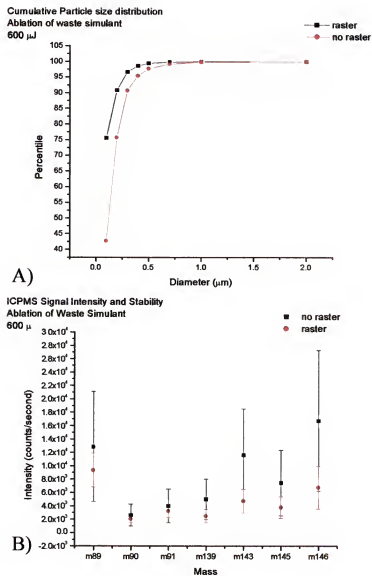


Figure 8-15. LA-ICPMS analysis of waste simulants prepared in Teflon Cups with and without rastering the laser beam. A) Particle size distribution. B) LA-ICPMS average signal intensities.

Table 8-4. % RSD values for sample preparation in cup with and without raster.

| % Relative Standard Deviation |           |        |
|-------------------------------|-----------|--------|
|                               | no raster | raster |
| Element                       | % RSD     | % RSD  |
| 89                            | 64        | 27     |
| 90                            | 62        | 29     |
| 91                            | 64        | 31     |
| 139                           | 60        | 40     |
| 143                           | 59        | 37     |
| 145                           | 66        | 43     |
| 146                           | 63        | 47     |

Table 8-5. % RSD values with and without the use an inertial impactor.

| % Relative Standard Deviation |      |           |           |             |  |
|-------------------------------|------|-----------|-----------|-------------|--|
| element                       | 1 mJ | 2 $\mu$ m | 1 $\mu$ m | 0.5 $\mu$ m |  |
|                               | RSD  | RSD       | RSD       | RSD         |  |
| 89                            | 52   | 24        | 16        | 56          |  |
| 90                            | 53   | 27        | 14        | 57          |  |
| 91                            | 52   | 28        | 15        | 56          |  |
| 139                           | 54   | 26        | 17        | 57          |  |
| 143                           | 54   | 28        | 16        | 57          |  |
| 145                           | 54   | 31        | 16        | 56          |  |
| 146                           | 54   | 29        | 16        | 56          |  |

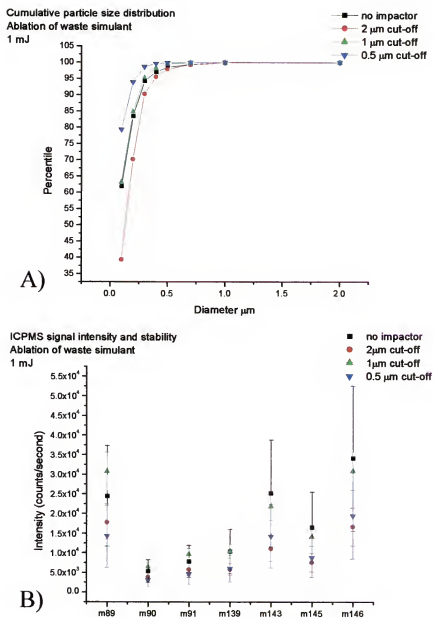


Figure 8-16. LA-ICPMS analysis of waste simulants using an inertial impactor  
A) Particle size distribution. B) Average ICPMS signal intensities.

When 1  $\mu\text{m}$  cut-off diameter was used with the impactor, % RSD values for most elements improved from approximately 50 % to less than 20%. This set of experiments showed that the use of the impactor at 1  $\mu\text{m}$  filter allowed a more precise analysis of most elements in the waste simulant.

### **Scanning electron images**

A Scanning Electron Microscope (SEM) equipped with an x-ray dispersive system was used to investigate differences in elemental concentrations between particles collected from ablation of waste simulant. Figure 8-17 shows a group of particles with diameters less than 0.5  $\mu\text{m}$  collected from the ablation of waste on a slide at 1 mJ. The x-ray dispersive system was used to approximate the concentration of several elements on the different particles. Figure 8-18 shows the images illustrating the effect of composition of different elements in the group of particles. The degree of brightness of each color on the particles signifies higher concentration of the particular element represented. For instance, Figure 8-19a shows the composition of calcium in the along the group of particles shown. The brighter pink spots indicated that some particles have a greater concentration of calcium than the rest of the particles. The different images imply the presence of elemental fractionation, with some particles having greater concentrations of some elements than the rest. Figure 8-20 shows a particle about 2  $\mu\text{m}$  in diameter. Similarly the composition of elements within the particle was mapped. Although, the particle was almost melted by the process, the difference in concentrations of the elements in the particle differed from the rest of the ablated material was evident. Figure 21 maps out the concentration of Ca, Fe, Na, Nd, and Zr.

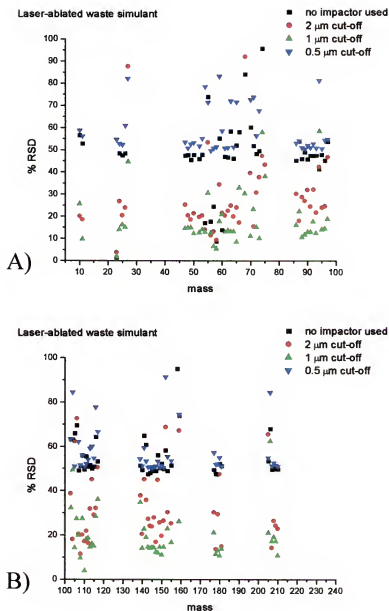


Figure 8-17. % RSD values resulting from LA-ICPMS analysis of waste simulants for most elements present in the simulant. A) Elements from mass 5-100. B) Elements from mass 100- 240.

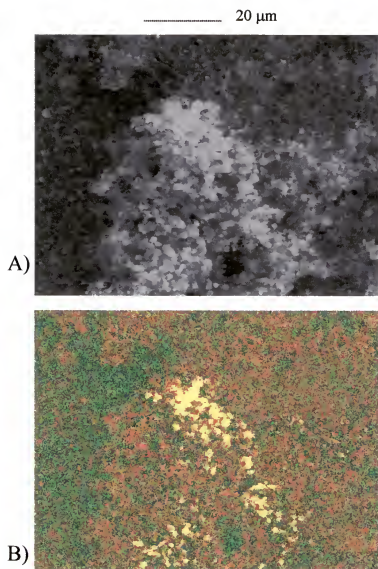


Figure 8-18. Images of a group of particles collected from the ablation of the waste simulants. A) Scanning electron image. B) Elemental Mapping of particles' composition.

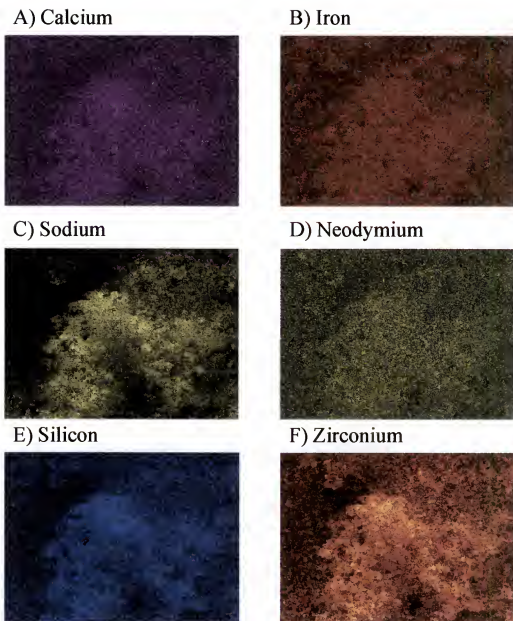


Figure 8-19. Elemental mapping of particles collected from the ablation of waste simulants. A) Calcium. B) Iron. C) Sodium. D) Neodymium. E) Silicon. F) Zirconium.

\_\_\_\_\_ 2  $\mu\text{m}$

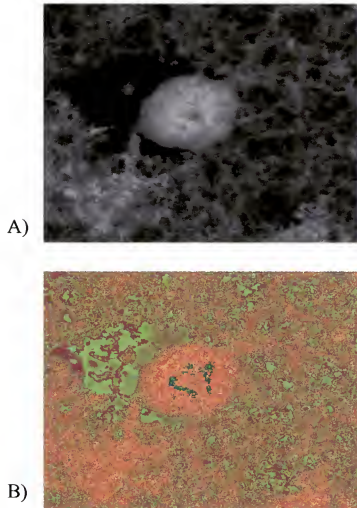


Figure 8-20. Close-up image of a particle collected from ablation of waste simulant.  
A) SEM image. B) Elemental mapping of composition.



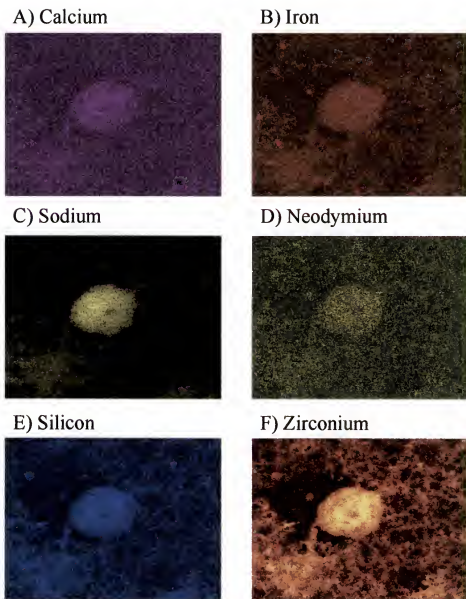


Figure 8-21. Elemental mapping of a particle collected from the ablation of waste simulants. A) Calcium. B) Iron. C) Sodium. D) Neodymium. E) Silicon. F) Zirconium.

### **Conclusion**

This chapter demonstrated that the methods of modifying the particle size distribution and methods to normalize the LA-ICPMS signal could be effectively applied to the analysis of waste simulants. Characterization of waste simulants were made with a precision lower than 10% for most elements as long as ablation parameters were optimized and with the implementation of the correction methods described in the preceding chapters was applied.

## CHAPTER 9 CONCLUSION AND FUTURE WORK

### **Conclusion**

The limiting source of noise in Laser ablation ICPMS originates from the ablation process itself. Variations in the particle size distribution, in the mean particle diameter, and in the mass of the sample aerosol are caused by non-linear variations in the ablation process consequently caused by a combination of factors such as pulse-to-pulse laser energy fluctuations and sample heterogeneity. The particle size distribution of a given sample can be improved by finding the optimum ablation parameters, laser wavelength, irradiance and beam diameter, that yield the smallest mean particle diameters and the narrowest distribution. For most samples, including nuclear wastes, a softer ablation using less than 1 mJ laser pulse energy of a laser with wavelength in the UV range produces smaller particles.

In cases where soft ablation does not yield enough mass ablated to produce ICPMS signal intensities well above the instrument's limits of detection, a method of improving the particle size distribution of the ablated mass has been developed. An inertial impactor can be used to effectively filter out larger particles ( $\sim 3 \mu\text{m}$  in diameter) from the ablated material. Results from this study have shown that larger particles are not effectively ionized in the ICPMS and do not contribute significantly to signal intensity. Therefore, removal of the larger particles does not compromise the analytical signal and improves the precision by at least a factor of two.

To compensate for the differences in mass ablated during an analysis, methods of normalization must be employed.

The use of light scattered by a sample aerosol (in this case, the laser-ablated material) to normalize the resulting ICPMS signal was investigated. It has been shown that the light scattered by single particles of one element is a function of both particle diameter and particle number density. For cases where the number of particles in the scattering region per residence time is more than one, and a size distribution exists (as in the case in laser ablation), the dependence of the light scattered on particle diameter and number density may be more complex. However, the method of normalization may still be effective in correcting for the number of particles ( and consequently the mass ablated) if the mean particle diameter remains constant. In cases, where the size distribution varies, a mean average diameter and mean average scattering coefficient must be considered. For experimental purposes, the angle of collection must be with forward scatter mode. The effectiveness of the method for ablation of waste simulants was also investigated. A correlation between the scattered signal of the ablated material and the ICPMS signal was demonstrated. Normalization of the ICPMS signal intensities resulting from analysis of the simulants resulted in a significant reduction in %RSD values. This method of normalization also corrected for matrix effects in ablation of in-house standards. The linearity of ICPMS signals with analyte concentration was improved with the use of the scatter normalization. A disadvantage to this method is that the normalization does not account for laser-induced fractionation.

The use of the emission intensities collected from the laser-induced plasma created upon ablation as a means of ICPMS signal normalization was investigated. An apparent

correlation was demonstrated to exist between an analyte's emission intensity and its corresponding ICPMS signal, both of which are affected by variations in the ablation process. The results have also demonstrated that two or more elements can be monitored over time with the ICPMS and a spectrometer to monitor ablation differences over time. This results in an effective normalization method accounting for differences in mass ablated on a per element basis. This method of normalization is ideal for applications requiring knowledge on elemental ratios.

For the analysis of heterogeneous nuclear wastes, a combination of optimizing the laser and ICPMS operating parameters, modifying the particle size distribution of the sample aerosol with the inertial impactor, and normalizing the ICPMS signal with the light scattered by the resulting sample aerosol was employed. The results confirmed that the use of these methods increased the precision by a factor of 20 times for some elements, and at least 2 times for most elements. The use of these methods also compensated for differences in mass ablated for different matrices and thus allowed the use of in-house standards for the quantitative analysis of the heterogeneous materials such as nuclear wastes. The compensation for matrix-effects caused by the ablation process allowed for more accurate quantitative analyses. Variations in the ablation behavior of each element were compensated for, thus allowing more accurate analyses, especially in cases where elemental ratios were required.

### **Future Work**

Future work on Laser ablation ICPMS will rely heavily on improving sample introduction into the ICPMS. More work has to be performed to find the optimum way of introducing the laser-ablated material into the ICPMS so that it is transported and ionized efficiently.

The experiments performed in this dissertation, however, leave many questions and tasks in mind. Rigorous fundamental studies must be performed to determine the maximum particle diameter which can be efficiently ionized by the ICP. When the optimum particle diameter is known, steps must be taken towards finding ablation parameters yielding optimum particle size for specific applications. Since the existence of particle size distributions introduces noise in the ICPMS analysis, ways of producing mono-disperse particles by laser ablation must be found. The use of particle separating devices such as the DMA or Differential Mobility Analyzer must be investigated.

The scattering device employed for this research can also be used to study transport mechanisms from the ablation cell to the ICP. Two scattering cells may be created, one located right near the ablation cell, and the other right before the ICP. The differences between the light scattered by the sample aerosol as it passes through each scattering cell may reveal information as to the extent of particle transport losses. Placing the scatter cell right before the plasma will also improve the normalization method. As previously mentioned, collecting the scattered signal at a forward angle improves the effectiveness of the method.

The normalization method involving the spectral emission intensity collected from the laser-induced plasma may be significantly improved with the use of a high-resolution spectrometer. Finally, the methods of improving the precision and accuracy of laser ablation- ICPMS analysis of heterogeneous materials must be applied and tested on other samples, such as geological and archeological materials, for a more definitive evaluation of their effectiveness.

## LIST OF REFERENCES

1. S. Durrant, *J. Anal. At. Spectrom.*, **14**, 1385 (1999)
2. A. Montaser, D.W. Golightly, ed., *Inductively Coupled Plasmas in Analytical Atomic Spectrometry*, 2<sup>nd</sup> Edition, (New York, VCH Publishers, Inc., 1992)
3. M.L. Alexander, M.R. Smith, J.S. Hartman, A. Mendoza, and D.W. Koppenaal, *Applied Surface Science*, **127-129**, 255 (1998)
4. S.E. Hobbs, J.W. Olesik, *Anal. Chem.*, **64**, 274 (1992)
5. T.H. Maiman, *Phys. Rev. Lett.*, **4**, 564 (1960)
6. T.H. Maiman, *Nature*, **187**, 493 (1960)
7. J.D. Winefordner, I.B. Gorunshkin, D. Papps, O.I. Matveev, and B.W. Smith, *J. Anal. Atomic Spec.*, **15**, 1161 (2000)
8. E. H. Piepmeier. *Analytical Applications of Lasers*, series Chemical Analysis, editors P.J. Elving, J.D. Winefordner, I.M. Kolthoff, vol. 87, (New York, John Wiley and sons, 1986)
9. F. Brech, *Appl. Spectrosc.*, **16**, 59 (1962)
10. J.D. Ingle, S.R. Crouch, *Spectrochemical Analysis*, (New Jersey: Prentice-Hall, Inc., 1988)
11. R.E. Russo, X.L. Mao, H.C. Liu, J.H. Yoo, S.S. Mao, *Appl. Phys. A*, **69**, S887 (1999)
12. R.E. Russo, X. Mao, S.S. Mao, *Anal. Chem.*, **74**, 71A (2002)
13. R.H. Wendt and V.A. Fassel, Induction-Coupled Plasma Spectrometric Excitation Source, *Anal. Chem.*, **37**, 920 (1965)
14. S. Greenfield, I. Ll. Jones, C.T. Berry, *Analyst*, **89**, 713 (1964)
15. R.S. Houk, V.A.F., G.D. Flesch, H.J. Svec, A.L. Gray and C.D. Taylor, *Anal. Chem.*, **52**, 2283, (1980)
16. R.H. Scott, V.A. Fassel, R.N. Kniseley, D.E. Nixon, *Anal. Chem.*, **6**, 76-80, (1974)

17. A.L. Gray, A.R. Date, *Applications of Inductively Coupled Plasma Mass Spectrometry*, (New York: Chapman and Hall, 1989)
18. N. Furuta, *Spectrochim. Acta*, **41B**, 1115 (1986)
19. P.W.J.M. Boumans, *Theory of Spectrochemical Excitation*, (New York: London/Plenum Press, 1986)
20. N. Furuta, *Spectrochim. Acta*, **40B**, 1013 (1985)
21. R.A. Browner and A.W. Boorn, *Anal. Chem.*, **56**, 786 (1984)
22. M. Thompson, J.E. Goulter, and F. Sieper, *Analyst*, **106**, 32 (1981)
23. A.L. Gray, *Analyst*, **110**, 551 (1985)
24. S.E. Jackson, H.P. Longerich, G.R. Dunning, B. Fryer, *J. Can. Mineral.*, **30**, 1049 (1992)
25. R.A. Stern, *Mineralogical Assoc. of Canada, Short Course Series*, **27**, 241 (1998)
26. P. Arrowsmith, S.K. Hughes, *Appl. Spectrosc.* **42**, 1231 (1988)
27. K. Knight, S. Chenery, S.W. Zochowski, M. Thompson, C.D. Flint, *J. Anal. Atom. Spectrom.* **11**, 53 (1996)
28. J.W. Olesik, J.C. Fister, *Spectrochim. Acta* **46B**, 851 (1991)
29. E.F. Cromwell and P. Arrowsmith, *Appl. Spectrosc.* **49**, 1652 (1995)
30. D.P. Baldwin, D.S. Zamzow, and A.P. D'Silva, *Anal. Chem.*, **66**, 1911 (1994)
31. H-M. Pang, D.R. Wiederin, R.S. Houk and E.S. Yeung, *Anal. Chem.* **63**, 390, (1991)
32. A.L. Gray, J.G. Williams, A.T. Ince, and M. Liezers, *J. Anal. Atom. Spectrochim.*, **9**, 1179
33. A.T. Ince, A.L. Gray, *J. Anal. Atom. Spectrochim.*, **8**, 899 (1993)
34. C. Geertsens, A. Buand, F. Chartier, J.L. Lacour, P. Mauchien, S. Sjostron
35. J.M. Mermet, J.M. (1994). *Journal of Atomic and Applied Spectroscopy*, **9**, 17, (1994)
36. M. Montelica-Heino, P. le Constumer, O.F.X. Donard, *J. Anal. Atom. Spectrochim.*, **16**, 542 (2001)
37. D. J. Figg, J.B. Cross, C. Brink, *Appl. Surf. Sci.* **129**, 287 (1998)




38. S.H. Jeong, O.V. Boirov, J.H. Yoo, X.L. Mao, R.E. Russo, *Anal. Chemistry*, **71**, 5123 (1999)
39. D. Pollman, C. Pilger, R. Hergenroder, F. Leis, *Spectrochimica Acta*, **49B**, 683 (1994)
40. M. Guilliong, D. Gunther, *J. Anal. At. Spectrom.* **17**, 831 (2002)
41. M. Guilliong, H. Kuhn, D. Gunther, *Spectrochim. Acta B*, *in press*
42. J. Thompson, PhD Thesis, University of Florida, Gainesville, FL, USA, 2001
43. T. Nomizu, H. Nakashima, Y. Hotta, T. Tanaka, and H. Kawaguchi, *Analytical Sciences*, **8**, 527 (1992)
44. S.A. Baker, B.W. Smith, and J.D. Winefordner, *Appl. Spectrosc.*, **52**, 154 (1998)
45. A.R. Jones, *Progress in Energy and Combustion Science*, **25**, 1 (1999)
46. J. H. Seinfeld, *Atmospheric Chemistry and Physics of Air Pollution* (New York: John Wiley and Sons, 1986)
47. M. Kerker, *The scattering of light*, (New York, Academic Press, 1969)
48. D.W. Hahn, J.E. Carranza, G.R. Arsenault, H.A. Johnsen, K.R. Hencken, *Review of Scientific Instruments*, **72**, 3706 (2001)
49. A. Fernandez, X.L. Mao, W-T. Chan, R.E.Russo. *Anal. Chem.*, **67**, 2444 (1995) normalization
50. S. Baker, PhD Thesis, University of Florida, Gainesville, FL, USA, 1998


## BIOGRAPHICAL SKETCH

Janina R. Gutierrez was born on March 16, 1976 in Quezon City, Philippines. She received a degree in Bachelor of Science in Chemistry in March 1998. She worked under a joint project of the United Nations, World Bank and Philippine Department of Environment and Natural Resources from March to December 1998 as a Project Evaluation and Monitoring Officer for the Montreal Protocol Desk. She then went to the University of Florida in August 1999 to pursue a Doctorate of Philosophy in Chemistry. She expects to receive her degree in August 2003.


I certify that I have read this study and that in my opinion it conforms to acceptable standards of scholarly presentation and is fully adequate, in scope and quality, as a dissertation for the degree of Doctor of Philosophy.

  
James D. Winefordner, Chair  
Graduate Research Professor of Chemistry


I certify that I have read this study and that in my opinion it conforms to acceptable standards of scholarly presentation and is fully adequate, in scope and quality, as a dissertation for the degree of Doctor of Philosophy.

  
Willard W. Harrison  
Professor of Chemistry


I certify that I have read this study and that in my opinion it conforms to acceptable standards of scholarly presentation and is fully adequate, in scope and quality, as a dissertation for the degree of Doctor of Philosophy.

  
David H. Powell  
Scientist of Chemistry

I certify that I have read this study and that in my opinion it conforms to acceptable standards of scholarly presentation and is fully adequate, in scope and quality, as a dissertation for the degree of Doctor of Philosophy.

  
John R. Eyler  
Professor of Chemistry

I certify that I have read this study and that in my opinion it conforms to acceptable standards of scholarly presentation and is fully adequate, in scope and quality, as a dissertation for the degree of Doctor of Philosophy.

  
Paul A. Mueller  
Professor of Geological Sciences

This dissertation was submitted to the Graduate Faculty of the Department of Chemistry in the College of Liberal Arts and Sciences and to the Graduate School and was accepted as partial fulfillment of the requirements for the degree of Doctor of Philosophy.

August 2003

\_\_\_\_\_  
Dean, Graduate School